Computer Sciences Department

Face, Expression, and Iris Recognition Using Learning-Based Approaches

Guodong Guo

Technical Report #1575

August 2006

UNIVERSITY OF WISCONSIN MADISON

FACE, EXPRESSION, AND IRIS RECOGNITION USING LEARNING-BASED APPROACHES

by

Guodong Guo

A dissertation submitted in partial fulfillment of
the requirements for the degree of

Doctor of Philosophy

(Computer Sciences)

at the

UNIVERSITY OF WISCONSIN–MADISON

2006

FACE, EXPRESSION, AND IRIS RECOGNITION USING LEARNING-BASED APPROACHES

Guodong Guo

Under the supervision of Professor Charles R. Dyer

At the University of Wisconsin-Madison

This thesis investigates the problem of facial image analysis. Human faces contain a lot of information that is useful for many applications. For instance, the face and iris are important biometric features for security applications. Facial activity analysis such as face expression recognition is helpful for perceptual user interfaces. Developing new methods to improve recognition performance is a major concern in this thesis.

In approaching the recognition problem of facial image analysis, the key idea is to use learning-based methods whenever possible. For face recognition, we propose a face cyclograph representation to encode continuous views of faces, motivated by psychophysical studies on human object recognition. For face expression recognition, we apply a machine learning technique to solve the feature selection and classifier training problems simultaneously, even in the small sample case.

Iris recognition has high recognition accuracy among biometric features, however, there are still some issues to address to make more practical use of the iris. One major problem is how to capture iris images automatically without user interaction, i.e., not asking users to adjust their eye positions. Towards this goal, a two-camera system consisting of a face camera and an iris camera is designed and implemented based on facial landmark detection. Another problem is iris localization. A new type of feature based on texture difference is incorporated into an objective function in addition to image gradient. By minimizing the objective function, the iris localization performance can be improved significantly. Finally, a method is proposed for iris encoding using a set of specially designed filters. These filters can take advantage of efficient integral image computation methods so that the filtering process is fast no matter how big the filters are.

ABSTRACT

This thesis investigates the problem of facial image analysis. Human faces contain a lot of information that is useful for many applications. For instance, the face and iris are important biometric features for security applications. Facial activity analysis such as face expression recognition is helpful for perceptual user interfaces. Developing new methods to improve recognition performance is a major concern in this thesis.

In approaching the recognition problem of facial image analysis, the key idea is to use learning-based methods whenever possible. For face recognition, we propose a face cyclograph representation to encode continuous views of faces, motivated by psychophysical studies on human object recognition. For face expression recognition, we apply a machine learning technique to solve the feature selection and classifier training problems simultaneously, even in the small sample case.

Iris recognition has high recognition accuracy among biometric features, however, there are still some issues to address to make more practical use of the iris. One major problem is how to capture iris images automatically without user interaction, i.e., not asking users to adjust their eye positions. Towards this goal, a two-camera system consisting of a face camera and an iris camera is designed and implemented based on facial landmark detection. Another problem is iris localization. A new type of feature based on texture difference is incorporated into an objective function in addition to image gradient. By minimizing the objective function, the iris localization performance can be improved significantly. Finally, a method is proposed for iris encoding using a set of specially designed filters. These filters can take advantage of efficient integral image computation methods so that the filtering process is fast no matter how big the filters are.

ACKNOWLEDGMENTS

This thesis is greatly dedicated to my advisor, Professor Chuck Dyer. His enthusiasm, guidance, and encouragement have been invaluable to this work. He taught me how to do research and how to best communicate ideas. I am very fortunate to have had an opportunity to work with him at UW-Madison. I would also like to thank him for continuous financial support for my work.

Dr. Mike Jones at MERL has been another source of inspiration and advice during last two years. He led me to the iris recognition work. He also gave me the research flexibility and constructive criticism. I am also grateful for his support for my summer internships. I have also benefited from discussions of research ideas with Paul Beardsley, Shai Avidan, Fatih Porikli, and Jay Thornton at MERL. I would also thank Zhengyou Zhang at Microsoft Research for his advice and encouragement during my summer internship with him.

I am also grateful to several former members of the vision group, including Russel Manning, Steve Seitz, and Liang-Yin Yu for useful discussions. Thanks to Nicola Ferrier for lending her pan-tilt unit for our experiments, and many students for allowing me to capture their face images for my research.

Special thanks are due to Professors Jude Shavlik, Yu Hen Hu, Jerry Zhu, and Stephen Wright for taking time to review this work as members of my thesis committee.

Most of all, I am deeply grateful to Limei Yang. Her love and affection, her spirit of optimism, and her belief in me were the only sources of strength during the difficult life as a graduate student. My kids, Xinwei and Ziwei, make me happy and proud even confronting hard stages of life. Finally, I would like to dedicate this thesis to my parents, Guanfa and Meifang. They encouraged me to learn and study from middle school to university. Without their love and support none of this work would have been possible.

TABLE OF CONTENTS

Page

Appendix

Page

LIST OF TABLES

LIST OF FIGURES

Figure Page

Appendix
Figure Page

Appendix
Figure Page

Appendix
Figure Page

Chapter 1

Introduction

Computer vision is the study and application of methods that allow computers to understand image content. The images can be single images or sequences of images. One major goal of computer vision research is to automatically recognize real objects or scenes. In particular, humans can recognize each other by looking at faces. As shown in Figure 1.1(a), we can recognize Tom Cruise quickly from his face image without any problem, even with changes in expression, pose, lighting, and hair style. A second ability of people when looking at faces is the ability to recognize facial expressions such as smiling in Figure 1.1(b). This thesis is concerned with developing improved methods for these two problems.

1.1 Recognition Problems

Recognizing faces and facial expressions are important abilities for many practical applications. Face expression recognition is useful for human-computer interaction, perceptual user interfaces, and interactive computer games [101] [92]. The face expression recognition problem is challenging because different individuals display the same expression differently. Selecting the most relevant features and ignoring unimportant features is a key step in solving this problem. But previous papers have not adequately addressed this issue.

Face recognition is an important biometric feature. Computational face recognition has been studied for over 30 years [18] [135], but the performance is still not high in comparison with face

(a) (b) (c)

Figure 1.1 (a) A face image, (b) a smiling face image, and (3) an iris image.

recognition by people. Observations from biological vision systems are helpful for designing computational methods. Recent psychophysical studies show that humans seem to represent objects as a series of connected views instead of separate single views [110] [111] [12]. But it is not clear how to develop a computational method that encodes and uses a series of continuous views.

Another important biometric feature is the iris of the eye, as shown in Figure 1.1 (c). Humans do not use iris features to recognize each other, but it turns out that iris features have been used to obtain high recognition accuracy for security applications [26]. Although iris recognition has high accuracy, there are still some issues remaining for practical use of this biometric. For example, the human iris is about 1cm in diameter, which is difficult to capture. Traditional systems capture iris images by requiring user cooperation and interaction. Users adjust their eye positions based on feedback from the camera system [125]. Is it possible to design an iris acquisition system without user interaction[1]?

Another challenging problem in building iris recognition systems is iris localization. Iris features cannot be used for recognition unless the iris region is localized precisely. Classical methods

[1] "User cooperation is still required" means that the user should look at the camera system. But users do not need to adjust their eye positions.

for iris localization are Daugman's integro-differential operator (IDO) [26] and Wildes' Hough transform [125]. When evaluated on a public iris database, both methods achieve only about 85 - 88% localization rates, which means that about 12 - 15 % of images cannot be used for recognition. Why don't classical methods work very well for iris localization? By analyzing these methods carefully, we found that all previous methods use only image gradient information for detecting iris boundaries. In order to improve iris localization performance, more information is needed. But what kind of information can be added? And how to incorporate that information?

This dissertation focuses on the above problems: face recognition, face expression recognition, and iris recognition. All these problems exploit information from face images as shown in Figure 1.2. Usually the whole face is used for face recognition, sparse local features are used for face expression recognition, and only the eye regions are used for iris recognition. The research emphasis is to develop improved methods that exhibit high recognition performance.

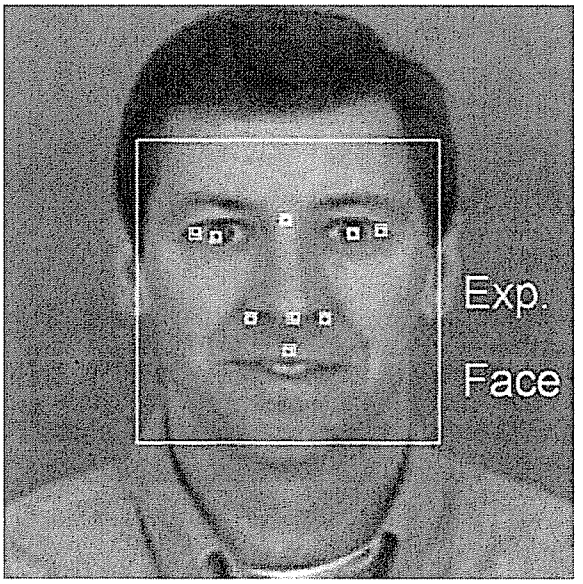

Figure 1.2 Facial image processing: face, face expression, and iris recognition.

1.2 Learning-based Approaches

How can the facial recognition problems listed in previous section be solved more successfully? In other words, what kinds of novel methods can be used to improve recognition performance? We use learning-based approaches. Because of the large variability within each object class, model-based approaches are difficult to define. On the contrary, learning-based approaches circumvent the difficulty in modeling and solve these problems in an efficient and robust way.

Learning-based approaches to computer vision problems, or simply *learning for vision*, is a promising research direction. There are two classes of methods in machine leaning: generative and discriminative learning methods. Generative methods use models that "generate" the observed data. The model is often a probability distribution. On the other hand, discriminative methods learn a function to discriminate among different classes of data. Which method is best depends on the task. The difference between generative and discriminative methods can be seen based on a statistical viewpoint. As shown in Figure 1.3, generative methods usually learn the conditional probability density function $p(x|C_i)$, where x is the data and C_i represents the class. When the prior, $p(C_i)$, is known for each class, a Bayesian decision can be made for classification or recognition. On the other hand, discriminative methods learn the posterior probability density function, $p(C_i|x)$, or a decision boundary directly.

For the specific problem of face expression recognition, where usually we have a small number of training examples, discriminative methods usually give better results than generative learning methods. The new methods that we use are discriminative learning methods, such as support vector machines [121] and a linear programming technique [9]. These methods are evaluated and compared with some existing generative methods experimentally. These results for face expression recognition may also be useful for other computer vision problems.

For face recognition, the learning comes from studying object recognition by people. Observations of the characteristics of biological vision systems are important for designing computer vision algorithms. Recent psychophysical studies show that people seem to represent objects as

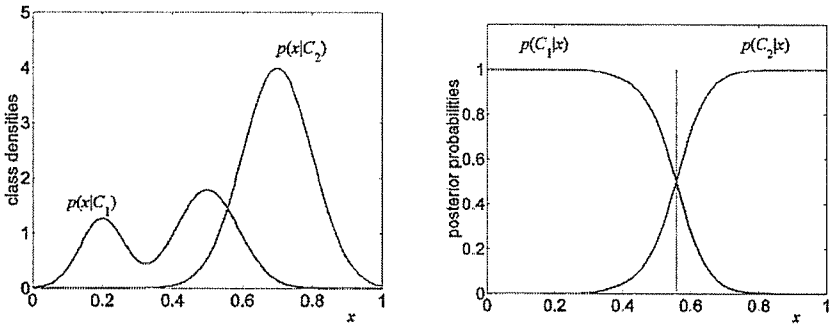

Figure 1.3 A statistical view of the generative and discriminative methods.

a series of connected views. Our research develops a computational method to encode and use a series of connected views for recognition.

For iris recognition, we focus on three sub-problems: iris acquisition, iris localization, and iris encoding. For automatic iris capture without user interaction, we design a two-camera system based on face anthropometry. The key observation is that anthropometric measures have small variations (within a few centimeters) over all races, genders, and ages. An AdaBoost-based detector [122] is developed for face and facial landmark detection. Then, the eye region detected in one camera is used to control another camera so that a high resolution iris image can be captured.

To localize iris boundaries, a new type of high-level knowledge is used and a new energy function is formulated. By minimizing this function, iris localization performance is improved significantly.

After irises are localized and normalized, the next issue is how to encode the iris pattern. A new set of filters is designed for this purpose. The new method has higher recognition accuracy and is faster than state-of-the-art methods.

To summarize the approaches to recognition problems studied in this dissertation, a categorization of learning for vision is shown in Figure 1.4.

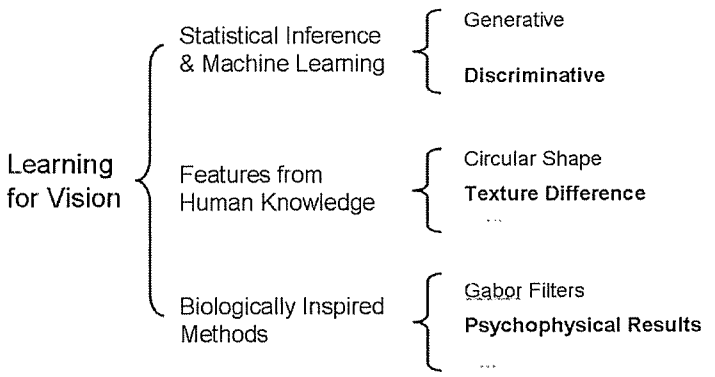

Figure 1.4 A categorization of learning for vision approaches.

1.3 Thesis Contributions

This thesis focuses mainly on learning-based approaches to the facial image analysis problems of face recognition, face expression recognition, and iris recognition. The major contributions include:

- For face recognition, we use a representation called face cyclographs in order to encode continuous views of faces [47]. Our research then develops a computational method that is inspired by psychophysical evidence for object representation and recognition. When a human head rotates in front of a stationary video camera, a spatiotemporal face volume can be constructed based on a fast face detector. A slicing technique is then used to analyze the face volume and a composite image is generated which we call a face cyclograph. To match two face cyclographs, a dynamic programming technique is used to align and match face cyclographs. We also introduce a technique for normalizing face cyclographs.

- For face expression recognition, we apply a recent linear programming method that can select a small number of features simultaneously with classifier training [44] [46]. The method was originally proposed by Bradley and Mangasarian [9]. We show that this method works well for recognizing face expressions using a very small number of features (usually less than 20). This kind of result has never been reported in previous face expression recognition

work. We also address the problem of learning in the small sample case [46] and show that this technique has the power to learn a classifier in the small sample case, which was not dealt with in the original paper [9].

- In iris recognition, first we present a two-camera system for capturing eye images automatically [52] instead of depending on user interaction to align his or her eye's position at the center of the image. Second, we propose a new objective function for iris localization [51]. The new method incorporates the texture difference between the iris and sclera or between the iris and pupil, in addition to the intensity gradient. This new method improves iris localization performance significantly over traditional methods. Third, we propose a new method for iris encoding [50] [49] based on a new set of filters, called difference-of-sum filters. The new method has higher accuracy and is faster than previous methods.

1.4 Thesis Outline

Chapter 2 presents the problem of moving face representation and recognition. To simplify the problem, we consider only single-axis rotations. Given a face video sequence with head rotation, a spatiotemporal face volume is constructed first. Then a slicing technique is presented to obtain a face cyclograph. Some properties of the face cyclograph representation are presented. After that, two methods are developed for recognition based on the face cyclograph representation. Finally, recognition experiments are performed on a video database with more than 100 videos.

Chapter 3 considers the problem of face expression recognition. We first introduce the linear programming formulation which was first developed in [9]. Then we give a simple analysis that shows why it can avoid the curse of dimensionality problem. The method is evaluated experimentally and compared with other methods.

Chapter 4 investigates the problem of iris recognition. First, we present a method for automatic iris acquisition using a two-camera system. One is a low-resolution "face camera" with a wide field of view, and another is an "iris camera" with narrow field of view. Second, we describe a new method for iris localization given an eye image. A new objective function is developed. We also

discuss the problem of model selection, i.e., circles vs. ellipses for representing the shape of the iris, and present a new method for the mask computation that can remove eyelid occlusion from the extracted iris images. Iris localization experiments are performed and compared with existing methods. Third, we consider iris encoding. We present a new method using a new set of filters, called difference-of-sum filters. Experiments on iris encoding are performed and compared with previous methods.

Chapter 5 extends the idea of iris capture using two cameras. The images taken by a high-resolution digital camera can be used to enhance the low-resolution video images. Our first attempt is to deal with a planar scene. As a result, we may acquire a high-resolution video sequence.

Finally Chapter 6 concludes by summarizing contributions and indicating future research directions.

Chapter 2

Face Cyclographs for Recognition

A new representation of faces, called face cyclographs, that incorporates all views of a rotating face into a single image, is introduced in this chapter. The main motivation for this representation comes from recent psychophysical studies that show that humans use continuous image sequences in object recognition. Face cyclographs are created by slicing spatiotemporal face volumes that are constructed automatically based on real-time face detection. This representation is a compact, multiperspective, spatiotemporal description. To use face cyclographs for face recognition, a dynamic programming based algorithm is developed. The motion trajectory image of the eye slice is used to analyze the approximate single-axis motion and normalize the face cyclographs. Using normalized face cyclographs can speed up the matching process.

2.1 Motivation

Over the last several years there have been numerous advances in capturing multiperspective images, i.e., combining (parts of) images taken from multiple viewpoints into a single representation that simultaneously encodes appearance from many views. Multiperspective images [130, 104] have been shown to be useful for a growing variety of tasks, notably scene visualization (e.g., panoramic mosaics [93] [107]) and stereo reconstruction [103]. Since one fundamental goal of computer vision is object recognition [82], a question may be asked: are multiperspective images of benefit for object recognition?

Under normal conditions, 3D objects are always seen from multiple viewpoints, either from a continuously moving observer who walks around an object or by turning the object so as to see

it from multiple sides. This suggests that a multiperspective representation of objects might be useful.

Recently, psychophysical results have shown that the human brain represents objects as a series of connected views [111] [123] [12]. In psychophysical experiments by Stone [111], participants learned sequences which showed 3D shapes rotating in one particular direction. If participants had to recognize the same object rotating in the opposite direction, it took them significantly longer to recognize and the recognition rate decreased. This result cannot be reconciled with traditional view-based representations [115] whose recognition performance does not depend on the order in which images are presented. Instead, it is argued in [111] that temporal characteristics of the learned sequences, such as the order of images, are closely intertwined with object representation. These results and others from physiological studies [85] support the hypothesis that humans represent objects as a series of connected views [12].

The findings from human recognition may give practical guidance for developing better computational object recognition systems. Bülthoff et al. [12] presented a method for face recognition based on psychophysical results [111] [123] in which they showed experimentally that the representation of connected views gives much better recognition performance than traditional view-based methods. The main idea of their approach is to process an input sequence frame-by-frame by tracking local image patches to achieve segmentation of the sequence into a series of time-connected "key frames" or views. However, a drawback of the "key frames" representation is that it heuristically chooses several single view images instead of integrating them together to form a composite visual representation.

Can we integrate all continuous views of an object into a *single* image representation? We propose to incorporate all views of an object using the cyclograph of the object [27], a type of multiperspective image [104]. A cyclograph is generated when the object rotates in front of a static camera or the camera rotates around the object.

Cyclographs have a long history in photography. The first patent related to making cyclographs was issued in 1911 [27]. Historically, different names were used, such as peripheral photographs,

rollout photographs, and circumferential photographs. A typical usage of the technique is in archeology, such as the rollout display of Maya vases, as one example is shown in Figure 2.1.[1]. The basic idea of a peripheral photograph is to include in one photograph the front, sides, and back of an object so that one could see all the detail contained on the surface of the object at once [27]. The technique can also be used for other cylindrical (or approximately cylindrical) objects such as pistons, cylinders, earth core samples, potteryware, etc. [27]. For example, a peripheral photography of a human head is shown in Figure 2.2.[2] See [27] for details on how to change a regular camera into a "strip" camera in order to capture peripheral photographs of objects.

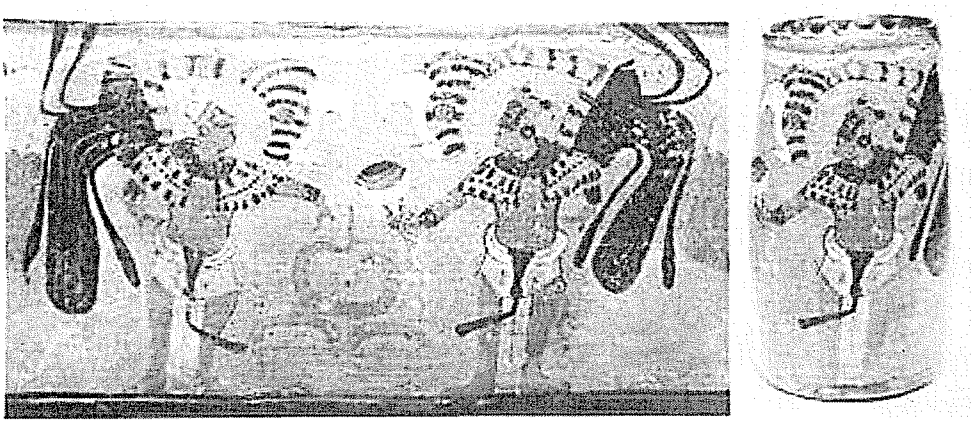

Figure 2.1 Left: A rollout photograph of a Maya vase; Right: One snapshot of the Maya vase.

Cyclographs have been used in computer vision and computer graphics, including image-based rendering [98] and stereo reconstruction [103] but, to our knowledge, there is no previous work using cyclographs for object recognition.

The rest of this chapter is organized as follows. Section 2.2 gives a short review of face recognition approaches. Section 2.3 presents the analysis of the *spatiotemporal volume* of continuous views of objects, and the generation of face cyclographs. Section 2.4 describes properties of face cyclographs especially for face recognition. Section 2.5 presents two methods for face recognition

[1]The Maya vase images are obtained from http://www.wide-format-printers.org/Mayan_Maya_vase_rollout_book/Mayan_vase_rollout_book.html

[2]The head image is obtained from http://www.rit.edu/~andpph/travel-exhibit.html

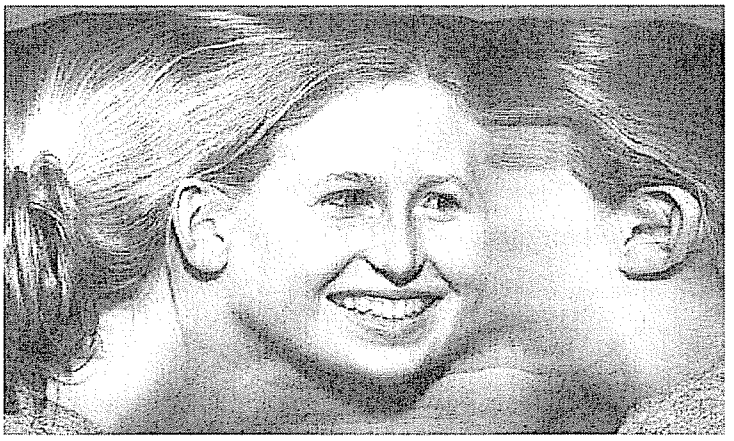

Figure 2.2 A peripheral photograph of a human head.

using face cyclographs. Experimental results are given in Section 2.6. Some issues are discussed in Section 2.7.

2.2 Related Work

Face recognition is an important biometric feature and has been studied for over 30 years. Some survey papers [18] [135] cover most research topics on face recognition. According to the type of input data, face recognition includes still image based and video based. Still image based face recognition can be viewed as a pattern recognition problem. Then we have two issues: feature extraction and classification. For feature extraction, lots of work focuses on linear dimensionality reduction such as principal component analysis (PCA) [119] and Fisher linear discriminant analysis (FLD) [4], and nonlinear dimensionality reduction such as the kernel PCA method [102]. For classification, the support vector machine (SVM) method [121] has shown to have high recognition accuracy [53] [56], and been used more and more in face recognition.

On the other hand, human faces share a similar geometrical structure. The elastic bunch graph matching (EBGM) method proposed by Wiskott et al. [128] takes advantage of the facial geometry and faces are represented as graphs, with nodes positioned at fiducial points, and edges labeled with 2D distance vectors. Each node contains a set of 40 complex Gabor wavelet coefficients at different

scales and orientations. Recognition is based on labeled graphs. This kind of method has been used in some commercial face recognition products.

Another representative method for still image based face recognition is the Bayesian method proposed by Moghaddam et al. [86]. The basic idea is to model the face recognition problem as a two-class classification problem, i.e., intra-person and inter-person. Bayesian rules are used to measure similarities. A drawback of this method is that each image has to be stored in order to compute the image difference between a new test face and the training faces.

For video-based face recognition, there are some recent approaches. In [67] Gabor features were extracted on a regular 2D grid and tracked using Monte Carlo sequential importance sampling. The authors reported performance enhancement over a frame to frame matching scheme. In another work [136], a framework was proposed to track and recognize faces simultaneously by adding an identification variable to the state vector in the sequential importance sampling method.

In [66] a probabilistic appearance manifold was used to represent each face. Example faces in a video were clustered by a k-means algorithm with each cluster called a pose manifold represented by a plane computed by principal component analysis (PCA). The connectivity between the pose manifolds encoded the transition probability between images in each pose manifold.

In [70] hidden Markov models (HMM) were used. During the training stage, an HMM was created to learn both the satistics and temporal dynamics of each individual. During the recognition stage, the temporal characteristics of the face sequence were analyzed over time by the HMM corresponding to each subject. The likelihood scores provided by the HMMs were compared, and the highest score determined the identity of a face in the video sequence.

In [1] the autoregressive and moving average (ARMA) model was used to model a moving face as a linear dynamic system and to perform recognition. Recognition was performed using the concept of subspace angles to compute distances between probe and gallery video sequences.

Hadid and Pietikinen [54] recently analyzed several video-based face recognition approaches and used the methods in [70] and [1] for experimental evaluation. Their conclusion was that these methods "do not systematically improve face recognition results" [54]. Previous video-based face recognition systems do not extract and use head motion information explicitly, although video data

has been used as the input either for training or testing. In conclusion, it is still not clear how to use motion information to help face recognition.

2.3 Viewing Rotating Objects

Our goal is to develop a computational method that encodes all continuous views of faces for face recognition. In some psychophysical experiments, the connected views of an object were captured by object rotation in one particular direction [111] [12]. Following this approach, we consider the class of single-axis rotations and associated appearances as the basis for capturing the continuous views of faces. The most natural rotations in depth for faces are when an erect person rotates his or her head, resulting in an approximately single-axis rotation about a vertical axis. Many other objects have single-axis rotations as the most "natural" way of looking at them. When we see a novel object we usually do not see random views of the object but in most cases we walk around it or turn the object in our hand [12].

2.3.1 Spatiotemporal Volume

Suppose that a 3D object rotates about an axis in front of a camera, as shown in Figure 2.3, where different circles represent different depths of the object, and a sequence of images are captured. Stacking together the sequence of images, a 3-dimensional volume, *x-y-t*, can be built, which is called a *spatiotemporal volume*. All continuous views are contained within this 3D volume data.

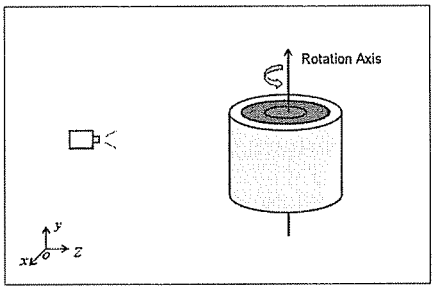

Figure 2.3 A camera captures a sequence of images when an object rotates about an axis. Circles with different radii denote different depths of the object.

In psychophysical studies, this 3D volume data is called a *spatiotemporal signature* and there is evidence showing that such signatures are used by humans in object recognition [110], but no computational representation was presented. We analyze the spatiotemporal volume and generate a computational representation of rotating objects.

2.3.2 3D Volume Analysis

The *spatiotemporal volume*, *x-y-t*, is a stack of *x-y* images accumulated over time *t*. Each *x-y* image contains only appearance but no motion information. On the contrary, the *x-t* or *y-t* images contain both spatial and temporal information. They are called *spatiotemporal images*. The *x-t* and *y-t* images can be obtained by slicing the *x-y-t* volume, as shown in Figure 2.4.

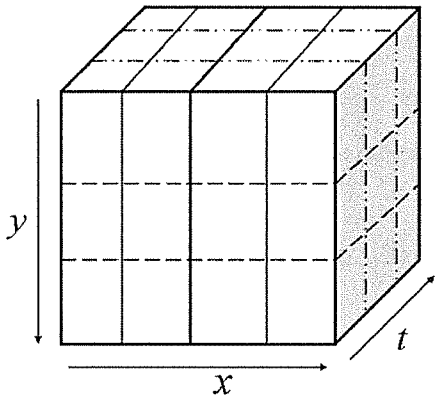

Figure 2.4 A 3-dimensional volume is sliced to get different image content. The *x-t* and *y-t* slices are *spatiotemporal images*.

Given a 3D volume, all the *x-t* (or *y-t*) slices preserve all the original information without any loss. The *x-y* slices are captured by the camera, while the *x-t* or *y-t* slices are cut from the volume independently. The union of all *x-t* (or *y-t*) slices is exactly the original volume. On the other hand, different slices, *i.e.*, *x-y*, *x-t*, or *y-t*, encode different information from the 3D volume.

Although both *x-t* and *y-t* slices are *spatiotemporal images*, they contain different information. When the object rotates about an axis that is parallel to the image's *y* axis, each *x-t* slice contains information on object points along a horizontal line on the object surface, defining the motion

trajectories of these points. One example is shown in Figure 2.11(a). On the contrary, each *y-t* slice contains the column-wise appearance of the object surface because of the object rotation about an axis that is parallel to the image's y axis. Thus *y-t* slices encode the appearance of the object as it rotates 360°. Partial examples are shown in Figure 2.9.

When a convex (or nearly convex) object rotates 360° about an axis, the *spatiotemporal volume* is constructed by stacking the whole sequence of images captured by a static camera. The slice that intersects the rotation axis usually contains the most visible appearance of the object in comparison with other parallel slices. Furthermore, this slice also has least distortion.

As shown in Figure 2.5 with a top-down view, when an object rotates 360°, each point on the object surface intersects the middle slice, S_4, once and only once. All other slices will miss seeing some parts of the object. In this sense S_4 contains the most appearance of the object. This can also be observed from the *y-t* slices in the face volume shown in Figure 2.9 in which the middle image corresponding to S_4. Further, slice S_4 usually minimizes foreshortening distortion because it captures every visible fronto-parallel surface point at a normal angle while other parallel slices do not.

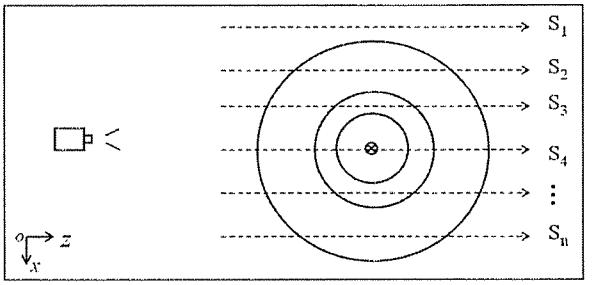

Figure 2.5 Top-down view of a 3D object rotating about an axis. The circles with different radii denote different depths on the object surface.

2.3.3 Spatiotemporal Face Volume

To represent rotating faces for recognition we need to extract a spatiotemporal sub-volume containing the face region, which we call the *spatiotemporal face volume*. A face detector [122] can be used to automatically detect faces in sequences of face images. Figure 2.6 shows the face

detection results in the first frame of a video sequence. The face positions reported by the face detector can then be used to determine a 3D face volume. False alarms from the face detector are removed by using facial skin color information. The eyes, detected with a similar technique as that in the face detector [122], are used for locating the motion trajectory image of the eye-level slice, which will be presented in Section 2.5.3.

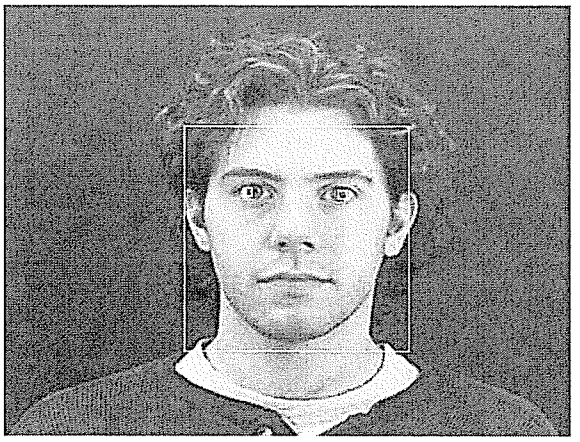

Figure 2.6 Face and eye detection in a frontal face image.

2.3.4 Face Cyclographs

Given a *spatiotemporal face volume* with each coordinate normalized between 0 and 1, we can analyze the 3D face volume via slicing. Based on Section 2.3.2, one may slice the volume in any way without information loss. However, the *y-t* slices encode all of the visible appearance of the object for single-axis rotation about a vertical axis. Furthermore, the unique slice that intersects the rotation axis usually contains the most visible appearance of the object with minimum distortion among all *y-t* slices. As a result, we will use this slice for the rotating face representation.

In our face volume, the slice that intersects the rotation axis is approximately the one with $x = 0.5$. This middle slice extracts the middle column of pixels from each frame and concatenates them to create an image, called the "cyclograph of a face," or simply "face cyclograph." One face cyclograph is created for each face video. The size of a face cyclograph image is determined by

the video length and the size of the segmented faces, i.e., the width of the face cyclograph is the number of frames in the video, and the height is the height of the segmented faces.

A face cyclograph can also be viewed as being captured by a strip camera [98]. As shown in Figure 2.8(b), the face cyclograph captures the face completely from left to right profiles, and all parts of the face surface are captured equally well. On the contrary, when a pin-hole camera is used as shown in Figure 2.8(a), the face surface is captured poorly when the camera's viewing rays approach grazing angle with the face surface, causing parts of the face surface to be captured unequally.

Figure 2.7 Some examples of face cyclographs. Each head rotates from frontal to its right side.

Because in our face videos (see Section 2.6.1 for details) the initial face is always approximately frontal and the last face is approximately a profile view, the created face cyclographs look like a "half face," as shown in Figure 2.7. To create a "whole face cyclograph," the head needs to rotate approximately 180^o. For recognition purpose, there is no need to capture 360^o head rotation since the back of the head has no useful information.

2.4 Properties of Face Cyclographs

Some properties of the face cyclograph representation are now described, especially concerning the face recognition problem.

2.4.1 Multiperspective

A face cyclograph is a multiperspective image of a face. The advantage of using a multiperspective face image is that the faces observed from all viewpoints can be integrated together into a single image representation. The multiperspective face image encodes facial appearance all

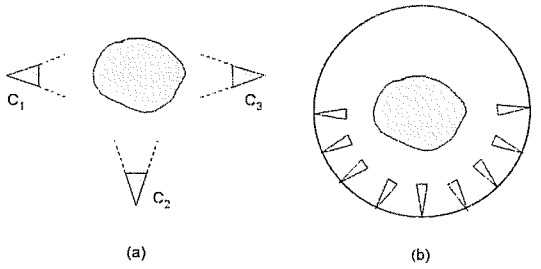

Figure 2.8 A face (nearly-convex object) is captured. (a) The frontal (from C_2) and side views (from C_1 and C_3) are captured separately. (b) The face cyclograph captures all parts of the face surface equally well.

Figure 2.9 The *y-t* slices of the face volume at every twenty-pixel interval in the *x* coordinate.

over the face surface and not just from 1 viewpoint. The face cyclograph can be viewed as being captured by a strip camera [98]. For nearly cylindrical objects (e.g., faces), each strip captures frontoparallel views of the surface along that strip. On the contrary, the "key frames" approach [12] uses a series of single perspective images.

2.4.2 Keeps Temporal Order

If a head rotates continuously in one direction, the face cyclograph successively extracts strips from the spatiotemporal face volume without changing the temporal order in the original face sequence. Temporal order is important for moving face recognition in psychophysical studies [110] [111] [12]. Computationally, temporal order is also important for designing a matching algorithm for face recognition. In Section 2.5 the recognition algorithm, which is based on dynamic programming, depends on this property.

2.4.3 Compact

The face cyclograph representation is compact. From Section 2.3, the *y-t* slices contain all appearance information in a *spatiotemporal face volume*. But only one slice intersects the rotation

axis (see Figure 2.5). The face cyclograph is constructed from this slice. The other slices that do not intersect the rotation axis are not used. Consequently, this representation largely reduces the redundancy in the *spatiotemporal face volume*. In comparison with Bülthoff's key frames approach [12], the face cyclograph uses local strips from moving faces without overlap, instead of using partially overlapped key frames and overlapped local patches from each key frame. Therefore the face cyclograph is a concise representation.

2.5 Recognition using Face Cyclographs

For face recognition, one face cyclograph is computed for each face video sequence containing one rotating face. Given a testing face sequence, the face cyclograph is computed first and then matched to all face cyclographs in the database. The recognition problem is illustrated in Figure 2.10. Two algorithms have been developed for matching face cyclographs. The first uses dynamic programming (DP) [96] for alignment and matching of face cyclographs. The monotonicity condition has to be satisfied to use DP and face cyclographs satisfy this by keeping the temporal order of the original face sequences. The second method analyzes the face motion trajectory image and then normalizes face cyclographs to the same size before matching.

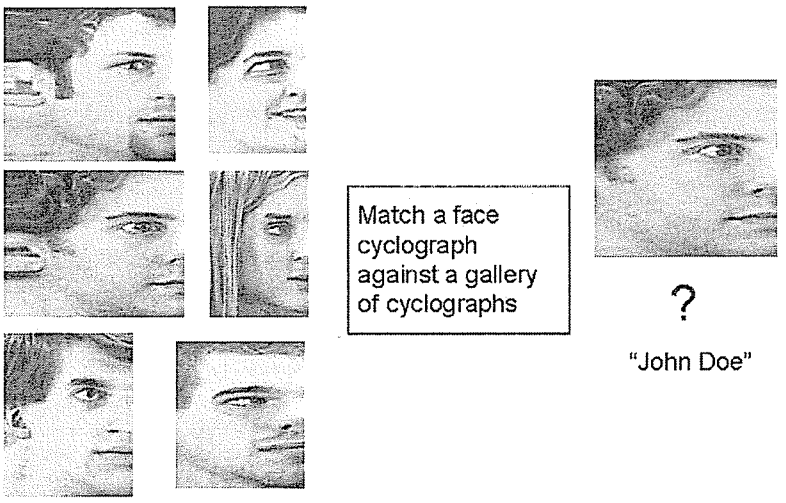

Figure 2.10 The recognition problem is defined as matching a face cyclograph against a gallery of cyclographs.

2.5.1 Matching Two Strips

The local match measure for comparing two strips is described in this subsection. Each strip is a vertical column in a face cyclograph image. Matching two strips in two face cyclographs is a 1D image matching problem. We define the similarity between two strips, i and j, in two cyclographs, 1 and 2, respectively, using the 1-norm:

$$S_{i,j}^{1,2} = \| \rho_1(strip_i^1, \Theta) - \rho_2(strip_j^2, \Theta) \|_1 \qquad [2.1]$$

where ρ_1 and ρ_2 are transforms for strips with respect to a parameter set Θ. Θ characterizes the method used for feature extraction. Currently, we simply use the pixel color information as the similarity measure; one could alternatively use a 1D wavelet transform to extract features and then match strips.

2.5.2 Matching Face Cyclographs using Dynamic Programming

Given a match measure between two strips, the next step is to match two face cyclographs. The number of strips within each cyclograph will vary in general because it is determined by the number of frames in the input video sequence, which itself is influenced by the speed and uniformity of the head rotation. The algorithm has to take these variabilities into consideration in matching face cyclographs.

We develop a method for matching face cyclographs based on the dynamic programming technique [96], which can effectively align variable-width face cyclographs and match them simultaneously. The DP technique can be used for matching face cyclographs because they keep the temporal order in head motion. The sub-problem of matching two strips was presented in Section 2.5.1.

The DP optimization is to find the minimum cost $C^{1,2}$ of matching two cyclographs, 1 and 2, where cyclograph 1 is the test face and cyclograph 2 is from the gallery of known faces. It is a composition of the following sub-problems,

$$C_{i,j}^{1,2} = \min\{C_{i-1,j-1}^{1,2}, C_{i-1,j}^{1,2}, C_{i,j-1}^{1,2}\} + S_{i,j}^{1,2} \qquad [2.2]$$

where $C_{i,j}^{1,2}$ is the minimum cost of matching strip pairs i and j in cyclographs 1 and 2, respectively. Note that indexes i and $i-1$ are always in face cyclograph 1, while j and $j-1$ are always in cyclograph 2. The accumulated costs are filled in a 2D table and an optimal path is traced back in the cost table. The final cost corresponds to the optimal path to match two face cyclographs. The smaller this cost, the more similar are two face cyclograph images.

The computational complexity of dynamic programming is $O(MN)$ to match two face cyclographs of widths M and N.

2.5.3 Normalized Face Cyclographs

Face cyclographs can also be normalized to the same size before matching. Using normalized face cyclographs can make the recognition process much faster, and allow feature extraction on 2D images rather than 1D strips. To normalize face cyclographs, we developed a method based on motion trajectory image analysis.

Motion-trajectory images are slices perpendicular to the rotation axis in the spatiotemporal volume. They are similar to epipolar plane images (EPI) [7]. The EPI was used for scene structure estimation with a camera moving along a straight line. Here we use the motion trajectory images for face motion analysis. For a face rotating about a vertical axis, the horizontal slices contain face motion trajectory information. Experimentally we found that the slice of the eyes gives richer information than other slices for motion analysis. One example of the eye slice is shown in Figure 2.11(a).

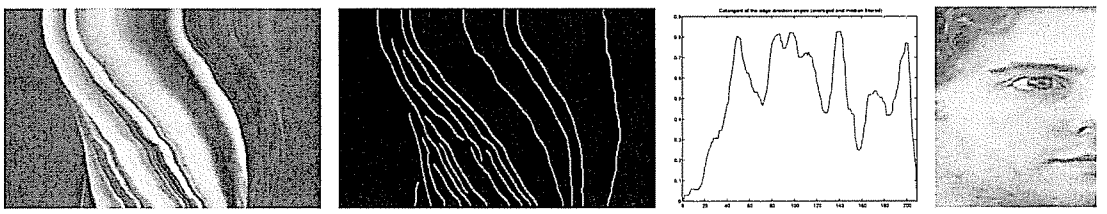

(a) (b) (c) (d)

Figure 2.11 (a) Motion trajectory image sliced along the right eye center. (b) Detected edges. (c) Cotangent of the edge direction angles averaged and median filtered. (d) The new face cyclograph after non-motion part removal.

Given the eye slice motion-trajectory image, we can detect and remove non-motion image frames from the original sequence of face images, and then align the remaining frames. The whole algorithm consists of the following 5 steps:

(1) Edge detection. Edges in the motion trajectory image are detected using the Canny edge detector [14].

(2) Average edge direction. The average of edge directions over each row in the edge image is estimated using

$$\overline{Dir_i} = \frac{1}{n_i} \sum_{j=1}^{n_i} \| \cot \theta_{ij} \| \qquad [2.3]$$

where n_i is the number of edges in row i of the motion trajectory image, θ_{ij} is the edge direction angle of the j^{th} edge in row i, and $\overline{Dir_i}$ is the average of edge direction in row i. This average improves the robustness for edge direction estimation.

(3) Median filtering [43] of average edge directions computed in previous step.

(4) Non-motion detection. Each row in the motion trajectory image corresponds to one frame in the original video sequence. $\overline{Dir_i}$ characterizes the amount of motion in frame i. If the average edge direction in row i is almost vertical, then there is no motion in frame i and the value of $\overline{Dir_i}$ will be very small. So, the criterion for non-motion detection is that if $\overline{Dir_i}$ is smaller than a threshold (experimentally chosen to be 0.4), frame i contains no motion. The detected frames with no motion are removed.

(5) Image warping. The remaining frames in the image sequence contain some head rotation between consecutive frames. The corresponding strips sliced from those frames are concatenated to construct the face cyclograph. In this way, all face cyclographs contain only moving parts. Finally, the face cyclograph is normalized to a fixed size by image warping [129].

2.6 Experiments

2.6.1 A Dynamic Face Database

A face video database with horizontal head rotation was captured. Each subject was asked to rotate his or her head from an approximately frontal view to an approximately profile view (i.e.,

approximately a 90^o head rotation). A single, stationary, uncalibrated camera was used to capture videos of the subjects. 28 individuals, each with 3 to 6 videos, were captured for a total of 102 videos in the database. The number of frames per video varies, ranging from 98 to 290, resulting in a total of 21,018 image frames. Each image is size 720×480. An image in one of our face videos is shown in Figure 2.6.

Each video in our face video database was matched against all other face videos, providing an exhaustive comparison of every pair of face videos. Precision and recall measures were computed to evaluate the algorithm's performance. Let TP stand for true positives, FP for false positives, and FN for false negatives. $Precision$ is defined as $\frac{TP}{TP+FP}$, and $recall$ is defined as $\frac{TP}{TP+FN}$. Precision measures how accurate the algorithm is in predicting the positives, and recall measures how many of the total positives the algorithm can identify. Both precision and recall were computed with respect to the top n matches, characterizing how many faces have to be examined to get a desired level of performance.

2.6.2 Face Recognition Results

Face cyclographs were created for all 102 face videos in our database. No faces were missed by this completely automatic process. The similarity measure between two face cyclographs was the 1-norm, i.e., $\alpha = 1$ in Eq. (2.1). Given a query face cyclograph, the costs of matching it with all remaining 101 face cyclographs were computed and sorted in ascending order. Then the precision and recall were computed with respect to the top n matches, with $n = 1, 2, \cdots, 101$. Finally, the precision and recall were averaged over all 102 queries and are shown in Figure 2.12.

Using the normalized face cyclograph method, the performance was lower than using DP. The reason may be that linear warping introduces artifacts. A non-linear warping method is under consideration.

The face cyclograph algorithms were also compared with a volume-based face recognition method, where the whole face volume was used for matching using the dynamic programming optimization method. As seen in Figure 2.12, the performance of the face cyclographs methods is very close to the volume-based method in terms of precision and recall. However, using the whole

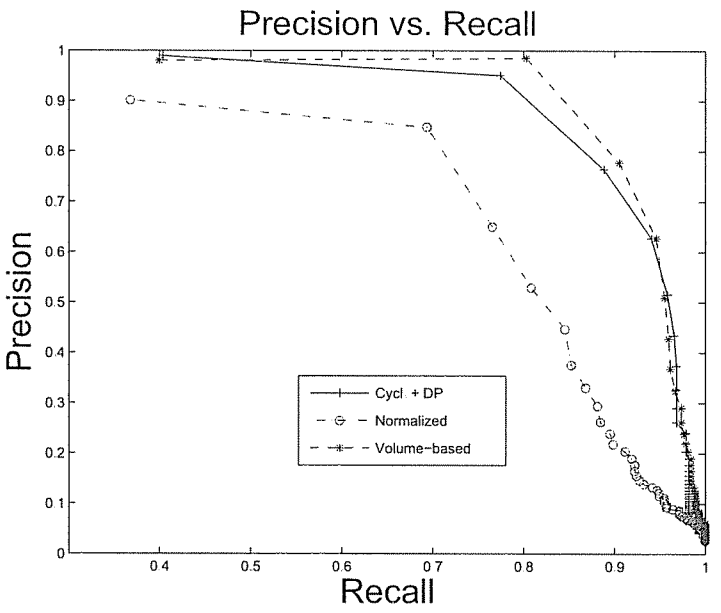

Figure 2.12 Average precision versus recall. The comparison is between face cyclographs (multiperspective), face volume-based method, and normalized face cyclographs.

volume has two disadvantages: (1) it requires a large amount of storage, and (2) it is very slow for volume-based matching. In our experiment, the program took more than 24 hours in order to obtain the precision and recall curve (as shown in Figure 2.12) using the whole volume data as input, while it took just a couple of minutes using the face cyclograph representation.

2.7 Discussion

In this chapter face cyclographs were used for face recognition, integrating the continuous views of a rotating face into a single image. We believe that this multiperspective representation is also useful for other object representation and recognition tasks. The basic idea is to capture object appearance from a continuous range of viewpoints and then generate a single multiperspective image to represent the object, instead of using multiple single-perspective images, which is the traditional view-based representation.

Assuming a simplified 3D head model, e.g., a cylinder [16] or ellipsoid [71], a 2D face image taken from a single viewpoint can be unwrapped when it is registered with the head model that

contains reference face texture maps. Our face cyclograph representation does not require any assumptions about the object shape, nor registration of different object views. Hence it is not difficult to extend the cyclograph representation for other object recognition tasks. Furthermore, the creation of a face cyclograph is simple and fast so it is useful for real-time recognition. Finally, unwrapped faces [16] [71] are not necessarily multiperspective [104], as face cyclographs are.

The focus of our approach is a face representation that encodes all views of a rotating face with a face cyclograph, and its use for face recognition. Our work is different from recent methods on video-based face recognition where the head motions used were arbitrary (see [54] and references there).

2.8 Summary

Motivated by recent psychophysical studies, this chapter presented a new face representation, called face cyclographs, for face recognition. Temporal characteristics are encoded as part of the representation, resulting in better face recognition performance than using traditional view-based representations. This new representation is compact, robust, and simple to compute from a *spatiotemporal face volume*, which itself is automatically constructed from a video sequence. Face recognition is performed using dynamic programming to match face cyclographs or using normalized face cyclographs based on motion trajectory analysis and image warping. We expect this multiperspective representation to improve results for other object recognition tasks as well.

Chapter 3

Face Expression Recognition

In this chapter a linear programming technique is introduced that jointly performs feature selection and classifier training so that a subset of features is optimally selected together with the classifier. Because traditional classification methods in computer vision have used a two-step approach: feature selection followed by classifier training, feature selection has often been ad hoc, using heuristics or requiring a time-consuming forward and backward search process. Moreover, it is difficult to determine which features to use and how many features to use when these two steps are separated. The linear programming technique used in this chapter, which we call feature selection via linear programming (FSLP), can determine the number of features and which features to use in the resulting classification function based on recent results in optimization. We analyze why FSLP can avoid the *curse of dimensionality* problem based on margin analysis. As one demonstration of the performance of this FSLP technique for computer vision tasks, we apply it to the problem of face expression recognition. Recognition accuracy is compared with results using Support Vector Machines, the AdaBoost algorithm, and a Bayes classifier.

3.1 Motivation

The goal of feature selection in computer vision and pattern recognition problems is to preprocess data to obtain a small set of the most important properties while retaining the optimal salient characteristics of the data. The benefits of feature selection are not only to reduce recognition time by reducing the amount of data that needs to be analyzed, but also, in many cases, to produce better classification accuracy due to finite sample size effects [59].

Most feature selection methods involve evaluating different feature subsets using some criterion such as probability of error [59]. One difficulty with this approach when applied to real problems with large feature dimensionality, is the high computational complexity involved in searching the exponential space of feature subsets. Several heuristic techniques have been developed to circumvent this problem, for example using the branch and bound algorithm [29] with the assumption that the feature evaluation criterion is monotonic. Greedy algorithms such as sequential forward and backward search [29] are also commonly used. These algorithms are obviously limited by the monotonicity assumption.

Sequential floating search [95] can provide better results but at the cost of higher search complexity. Jain and Zongker [59] evaluated different search algorithms for feature subset selection and found that the sequential forward floating selection (SFFS) algorithm proposed by Pudil *et al.* [95] performed best. However, SFFS is very time consuming when the number of features is large. For example, Vailaya [120] used the SFFS method to select 67 features from 600 for a two-class problem and reported that SFFS required 12 days of computation time.

Another issue associated with feature selection methods is the *curse of dimensionality*, i.e., the problem of feature selection when the number of features is large but the number of samples is small [59]. This situation is common in many computer vision tasks such as object recognition because there are often less than tens of training samples (images) for each object, but there are hundreds of candidate features extracted from each image.

Yet another difficult problem is determining how many features to select for a given data set. Traditional feature selection methods do not address this problem and require the user to choose the number of features. Consequently, this parameter is usually set without a sound basis.

Recently, a new approach to feature selection was proposed in the machine learning community called *Feature Selection via Concave Minimization* (FSV) [9]. The basic idea is to jointly combine feature selection with the classifier training process using a linear programming technique. The results of this method are (1) the number of features to use, (2) which features to use, and (3) the classification function. Thus this method gives a complete and optimal solution.

In order to evaluate how useful this method may be for problems in computer vision and pattern recognition, we investigate its performance using the face expression recognition problem as a testbed. 612 features were extracted from each face image in a database and we will evaluate if a small subset of these features can be automatically selected without losing discrimination accuracy. Success with this task will encourage future use in other object recognition problems as well as other applications including perceptual user interfaces, human behavior understanding, and interactive computer games.

This chapter is organized as follows. First, related work is reviewed in Section 3.2. The feature selection via linear programming (FSLP) formulation is presented in next section. We analyze why this formulation can avoid the *curse of dimensionality* problem in Section 3.4. Then we describe the face expression recognition problem and the feature extraction method used in Section 3.5. The FSLP method is experimentally evaluated in Section 3.6 and results are compared with Support Vector Machines, AdaBoost, and a Bayes classifier.

3.2 Related Work

There are two versions of the face expression recognition problem depending on whether an image sequence is the input and the dynamic characteristics of expressions are analyzed, or a single image is the input and expressions are distinguished based on static differences.

Previous work on dynamic expression recognition includes the following. Suma *et al.* [112] analyzed dynamic facial expressions by tracking the motion of twenty markers. Mase [83] computed first- and second-order statistics of optical flow in evenly divided small blocks. Yacoob and Davis [132] used the inter-frame motion of edges extracted in the areas of the mouth, nose, eyes, and eyebrows. Bartlett *et al.* [3] combined optical flow and principal components obtained from image differences. Essa and Pentland [34] built a dynamic parametric model by tracking facial motion over time. Donato *et al.* [30] compared several methods for feature extraction, and found that Gabor wavelet coefficients and independent component analysis (ICA) gave the best representation. Tian *et al.* [116] tracked upper and/or lower face action units over sequences to construct their parametric models.

There has also been considerable work on face expression recognition from single images. Padgett and Cottrell [91] used seven pixel blocks from feature regions to represent expressions. Cottrell and Metcalfe [19] used principal component analysis and feed-forward neural networks. Rahardja *et al.* [99] used a pyramid structure with neural networks. Lanitis *et al.* [65] used parameterized deformable templates to represent face expressions. Lyons *et al.* [74] [75] and Zhang *et al.* [134] [133] demonstrated the advantages of using Gabor wavelet coefficients to code face expressions. See [92] [36] for reviews of different approaches for face expression recognition.

Facial expressions are usually performed during a short time period, e.g., lasting for about 0.25 to 5 seconds [36]. Thus, intuitively, face expression analysis requires image sequences as input. However, we can also tell the expression from single pictures of faces such as those in magazines and newspapers. As shown in Figure 3.1, one can easily recognize the face expression from the picture in a magazine. So, either image sequences or single images are appropriate input data for facial expression analysis.

Figure 3.1 A smiling face on a magazine cover.

Almost all previous work does not address the feature selection problem for face expression recognition, partly because of the small number of training examples. Some previous work noticed

that different features may have different discriminative capabilities, however, to our knowledge little work addresses the feature selection problem explicitly for face expression recognition. For instance, it was noticed that the links have different weights in artificial neural networks [134] [133]. In our face expression recognition method, we will address the feature selection problem explicitly.

As for feature extraction, Gabor filters have demonstrated good performance [74] [75] [134] [133], so we use Gabor filters to extract facial features.

Here, we are interested in face expression recognition from single images. Our major focus is on the evaluation of some new methods for face expression recognition. Recently, large margin classifiers such as support vector machines (SVMs) [121] and AdaBoost [41] were studied in the machine learning community, and have been used for solving some vision problems. Here, we are interested to see if they are useful for face expression recognition learning in the small sample case. To our knowledge, this is the first time that large margin classifiers have been evaluated for face expression recognition [44] [46].

3.3 Linear Programming Formulation

In the early 1960s, the linear programming (LP) technique [79] was used to address the pattern separation problem. Later, a robust LP technique was proposed to deal with linear inseparability [5]. Recently, the LP framework has been extended to cope with the feature selection problem [9]. We briefly describe this new LP formulation below.

Given two sets of points $\mathcal{A}$ and $\mathcal{B}$ in R^n, we seek a linear function such that $f(x) > 0$ if $x \in \mathcal{A}$, and $f(x) \leq 0$ if $x \in \mathcal{B}$. This function is given by $f(x) = w'x - \gamma$, and determines a hyperplane $w'x = \gamma$ with normal $w \in R^n$ that separates points $\mathcal{A}$ from $\mathcal{B}$. Let the set of m points, $\mathcal{A}$, be represented by a matrix $A \in R^{m \times n}$ and the set of k points, $\mathcal{B}$, be represented by a matrix $B \in R^{k \times n}$. After normalization, we want to satisfy

$$Aw \geq e\gamma + e, \quad Bw \leq e\gamma - e \qquad [3.1]$$

where e is a vector of all 1s with appropriate dimension. Practically, because of overlap between the two classes, one has to minimize some norm of the average error in (3.1) [5]:

$$\begin{aligned} \min_{w,\gamma} f(w,\gamma) = min_{w,\gamma} \quad & \tfrac{1}{m} \parallel (-Aw + e\gamma + e)_+ \parallel_1 \\ & + \tfrac{1}{k} \parallel (Bw - e\gamma + e)_+ \parallel_1 \end{aligned} \qquad [3.2]$$

where x_+ denotes the vector with components $\max\{0, x_i\}$. There are two main reasons for choosing the 1-norm in Eq. (3.2): (i) it is easy to formulate as a linear program (see (3.3) below) with theoretical properties that make it computationally efficient [5], and (ii) the 1-norm is less sensitive to outliers such as those occurring when the underlying data distributions have pronounced tails [9].

Eq. (3.2) can be modeled as a robust linear programming (RLP) problem [5]:

$$\begin{aligned} \min_{w,\gamma,y,z} \quad & \tfrac{e'y}{m} + \tfrac{e'z}{k} \\ subject\ to \quad & -Aw + e\gamma + e \leq y, \\ & Bw - e\gamma + e \leq z, \\ & y \geq 0, z \geq 0. \end{aligned} \qquad [3.3]$$

which minimizes the average sum of misclassification errors of the points to two bounding planes, $x'w = \gamma + 1$ and $x'w = \gamma - 1$, where "$'$" represents transpose.

Problem (3.3) solves the classification problem without considering the feature selection problem. In [9] a feature selection strategy was integrated into the objective function in order to simultaneously select a subset of the features. Feature selection is defined by suppressing as many components of the normal vector w to the separating plane P as needed to obtain an acceptable discrimination between the sets $\mathcal{A}$ and $\mathcal{B}$. To accomplish this, they introduced an extra term into the objective function of (3.3), reformulating it as

$$\min_{w,\gamma,y,z} \quad (1-\lambda)\left(\tfrac{e'y}{m} + \tfrac{e'z}{k}\right) + \lambda e'|w|_*$$

$$\begin{aligned} subject\ to \quad & -Aw + e\gamma + e \leq y, \\ & Bw - e\gamma + e \leq z, \\ & y \geq 0, z \geq 0. \end{aligned} \tag{3.4}$$

where $|w|_* \in R^n$ has components equal to 1 if the corresponding components of w are nonzero, and has components equal to 0 if the corresponding components of w are 0. So, $e'|w|_*$ is actually a count of the nonzero elements in the vector w. This is the key to integrating feature selection with the classifier training process. As a result, Problem (3.4) balances the error in discrimination between two sets $\mathcal{A}$ and $\mathcal{B}$, $\frac{e'y}{m} + \frac{e'z}{k}$, and the number of nonzero elements of w, $e'|w|_*$. Moreover, if an element of w is 0, the corresponding feature is removed. Thus, only the features corresponding to nonzero components in the normal w are selected after linear programming optimization.

In [9] a method called *Feature Selection via Concave Minimization* (FSV) was developed to deal with the last term in the objective function of (3.4). They first introduced a variable v to eliminate the absolute value in the last term by replacing $e'|w|_*$ with $e'v_*$ and adding a constraint $-v \leq w \leq v$, which models the vector $|w|$. Because the step function $e'v_*$ is discontinuous, they used a concave exponential to approximate it, $v_* \approx t(v, \alpha) = e - \varepsilon^{-\alpha v}$, in order to get a smooth solution. This required introduction of an additional parameter, α. Alternatively, instead of computing the concave exponential approximation, a simple term $e's$ with only one parameter, μ, can be used. This produces the final formulation, which we call *Feature Selection via Linear Programming* (FSLP) [131]:

$$\begin{aligned} \min_{w,\gamma,y,z} \quad & \left(\frac{e'y}{m} + \frac{e'z}{k}\right) + \mu e's \\ subject\ to \quad & -Aw + e\gamma - y \leq -e, \\ & Bw - e\gamma - z \leq -e, \\ & -s \leq w \leq s, \\ & y, z \geq 0. \end{aligned} \tag{3.5}$$

The FSLP formulation in (3.5) is slightly different from the FSV method [9] in that FSLP is simpler to optimize and is easier to analyze in relation to the margin, which we do in Section 3.4. It should be noted that the normal of the separating hyperplane w in (3.5) has a small number of non-zero components (about 18) and a large number of 0 components (594) in our experiments. The features corresponding to the 0 components in the normal vector can be discarded, and only those with non-zero components are used. As a result, no user-specified parameter is required to tell the system how many features to use.

3.4 Avoiding the Curse of Dimensionality

In [9] the authors did not address the issue of the *curse of dimensionality*. Instead, they focused on developing the FSV method to get a smooth solution, which is not explicitly connected with the margin analysis we do here. Also, their experiments used data sets in which the number of examples was much larger than the number of feature dimensions. Here we will show that the FSLP method is actually related to margin maximization, which makes it possible to avoid the *curse of dimensionality* problem [59].

Consider the last term, $e's$, in the objective function of (3.5), where s is the absolute value of the normal w due to the constraint $-s \leq w \leq s$. To minimize the objective function in (3.5) requires minimizing the term $e's$ too. Since

$$e's = \sum_i s_i = \sum_i |w_i| = \| w \|_1 \qquad [3.6]$$

this means minimizing $\| w \|_1$, which is the 1-norm of the normal w. Because minimizing $\| w \|_1$ is equivalent to maximizing $\frac{1}{\|w\|_1}$, the objective function in (3.5) maximizes $\frac{1}{\|w\|_1}$.

Recall from Eq. (3.1) there are two bounding hyperplanes, $P1 : w'x - \gamma = 1$ and $P2 : w'x - \gamma = -1$. The discriminating hyperplane P is midway between these two hyperplanes, i.e., $w'x - \gamma = 0$. The distance of any point x to the hyperplane P is defined as $d(x; P) = \frac{|w'x-\gamma|}{\|w\|_2}$. From Eq. (3.1) $|w'x - \gamma| \geq 1$, so any point, x, that is outside the two bounding hyperplanes, $P1$ and $P2$, satisfies $d(x; P) \geq \frac{1}{\|w\|_2}$.

The minimum distance between the two bounding hyperplanes is $\frac{2}{\|w\|_2}$, which is defined as the margin, similar to that used in SVMs [121]. We know that the p-norm is non-increasing monotonic for $p \in [1, \infty]$, so $\| w \|_1 \geq \| w \|_2, \forall w \in R^n$, which is equivalent to

$$\frac{1}{\| w \|_1} \leq \frac{1}{\| w \|_2}. \qquad [3.7]$$

Also, the p-norm $\| w \|_p$ is convex on R^n, $\forall p \in [1, \infty]$ [100]. So, by maximizing $\frac{1}{\|w\|_1}$, we approximately maximize $\frac{2}{\|w\|_2}$. As a result, the last term, $e's$, in the objective function of (3.5) has the effect of maximizing the margin.

Maximizing the margin can often circumvent the *curse of dimensionality* problem, as seen in Support Vector Machines, which can classify data in very high-dimensional feature spaces [121] [32]. The FSLP method has a similar advantage because it incorporates a feature selection process based on margin size.

In fact, when $\mu = 0$ the last term in the objective function of (3.5) disappears. In this case classification performance worsens (we do not describe this case in Section 3.6 formally) because the remaining two terms do not have the property of maximizing the margin. So, the last term, $e's$, has two effects: (i) feature selection, and (ii) margin maximization.

Because the *curse of dimensionality* problem occurs in so many computer vision tasks, our analysis that FSLP circumvents this problem is an important new result. Further demonstration of this property is shown empirically in Section 3.6.

3.5 Face Expression Recognition

Face expression recognition is an active research area in computer vision. Here we investigate face expression recognition from static images using Gabor filters for facial feature extraction. Several researchers [74] [75] [134] [133] have demonstrated the advantages of using Gabor wavelet coefficients [24] to code facial expressions.

A two-dimensional Gabor function, $g(x, y)$, and its Fourier transform, $G(u, v)$, can be written as

$$g(x, y) = \frac{1}{2\pi\sigma_x\sigma_y} \exp\left[-\frac{1}{2}\left(\frac{x^2}{\sigma_x^2} + \frac{y^2}{\sigma_y^2}\right) + 2\pi j W x\right] \qquad [3.8]$$

$$G(u,v) = \exp\left\{-\frac{1}{2}\left[\frac{(u-W)^2}{\sigma_u^2} + \frac{v^2}{\sigma_v^2}\right]\right\} \quad [3.9]$$

where W is the frequency of a sinusoidal plane wave along the x-axis, and σ_x and σ_y are the space constants of the Gaussian envelope along the x and y axes, respectively. $\sigma_u = 1/2\pi\sigma_x$ and $\sigma_v = 1/2\pi\sigma_y$. Filtering a signal with this basis provides a localized frequency characterization. Filters with arbitrary orientation can be obtained by a rotation of the x-y coordinate system.

In earlier applications of Gabor filtering [24] for face recognition [64] [128] and face expression classification [74] [75] [134] [133], investigators have only varied the scale and orientation of the filters, but kept the Gaussian envelope parameter σ fixed to π or 2π. This methodology is questionable because the area of the energy distribution of the filters varies with scale, so the Gaussian envelope should vary with the filter size. Consequently, we designed the Gabor filter bank based on the filters used previously for texture segmentation and image retrieval [60] [80].

The Gabor filter bank is designed to cover the entire frequency spectrum [60] [80]. In other words, the Gabor filter set is constructed such that the half-peak magnitude of the filters in the frequency spectrum touch each other. This results in the following formulas to compute the filter parameters σ_u and σ_v:

$$a = \left(\frac{U_h}{U_l}\right)^{\frac{1}{S-1}}, \quad W = a^m U_l, \quad [3.10]$$

$$\sigma_u = \frac{(a-1)W}{(a+1)\sqrt{2\ln 2}} \quad [3.11]$$

$$\sigma_v = \tan\left(\frac{\pi}{2K}\right)\left[W - \frac{(2\ln 2)\sigma_u^2}{W}\right]\left[2\ln 2 - \frac{(2\ln 2)^2\sigma_u^2}{W^2}\right]^{-\frac{1}{2}} \quad [3.12]$$

where U_l and U_h denote the lower and upper center frequencies of interest. $m \in \{0, 1, \ldots, S-1\}$ and $n \in \{0, 1, \ldots, K-1\}$ are the indices of scale and orientation, respectively. K is the number of orientations and S is the number of scales.

In our experiments we used $U_h = \sqrt{2}/4$, $U_l = \sqrt{2}/16$, three scales ($S = 3$) and six orientations ($K = 6$). The half-peak support of the Gabor filter bank is shown in Figure 3.2. The differences in the strength of the responses of different image regions is the key to the multi-channel approach to face image analysis. The amplitudes of each filtered image at selected fiducial points were used as

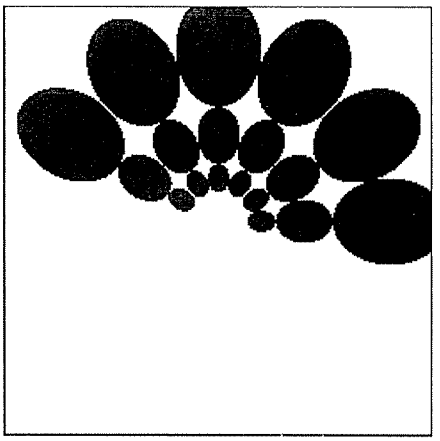

Figure 3.2 The filter set in the spatial-frequency domain. There are a total of 18 Gabor filters shown at half-peak magnitude.

feature vectors. Thus, for each face image, the extracted feature vector was length 612 (34x3x6) when 34 fiducial points were used. Typical positions of the fiducial points are shown in Figure 3.3.

3.6 Experimental Evaluation

3.6.1 Face Expression Database

The face expression database [74] used in our experiments contains 213 images of 10 Japanese women. Each person has two to four images for each of seven expressions: neutral, happy, sad, surprise, anger, disgust, and fear. Each image size is 256 x 256 pixels. A few examples are shown in Figure 3.4. For more information on the database such as image collection, data description, and human ranking, see [74]. This database was also used in [75] [134] [133].

3.6.2 Experimental Results

Our experimental procedure used 10-fold cross-validation because the database contains only 213 images. That is, the database was divided randomly into ten roughly equal-sized parts, from which the data from nine parts were used for training the classifiers and the last part was used for testing. We repeated this procedure ten times so that each part was used once as the test set.

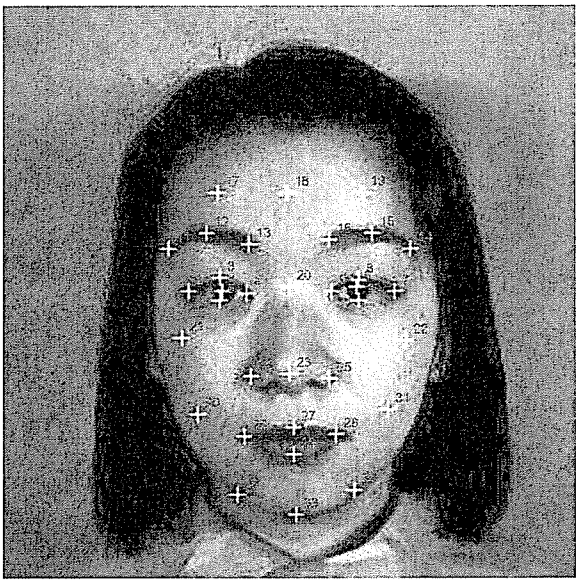

Figure 3.3 34 fiducial points on a face image.

Experimentally we found that the parameter μ in (3.5) is best set to a small value, and we used $\mu = 0.00001$ in all experiments. To solve this 7-expression classification problem we used a simple binary tree tournament scheme with pairwise comparisons.

Experimental results of the FSLP method are shown in Table 3.1. Feature selection was performed for each pair of classes, resulting in a total of 21 pairs for the 7-expression classification problem. The second column in Table 3.1 shows the number of selected features on average over the 21 pairwise classifiers, ranging from 16.0 to 19.1 for the ten runs. The average number of selected features over the ten runs was 17.1. Thus a very sparse set of features was automatically selected out of the 612 features extracted from each face image. This demonstrates that FSLP can significantly reduce the number of feature dimensions, and without any user interaction.

The third column in Table 3.1 shows the total number of features selected by FSLP for all 21 pairwise classifiers in each test set. Because some features are useful in discriminating between one pair, say, "angry" and "happy," but not for separating another pair, say "angry" and "sad," the number of features selected for all pairs is larger than that for each pair. For instance, there were 82 selected features for 21 pairwise classifiers in Set 1. This number is still much smaller than all 612

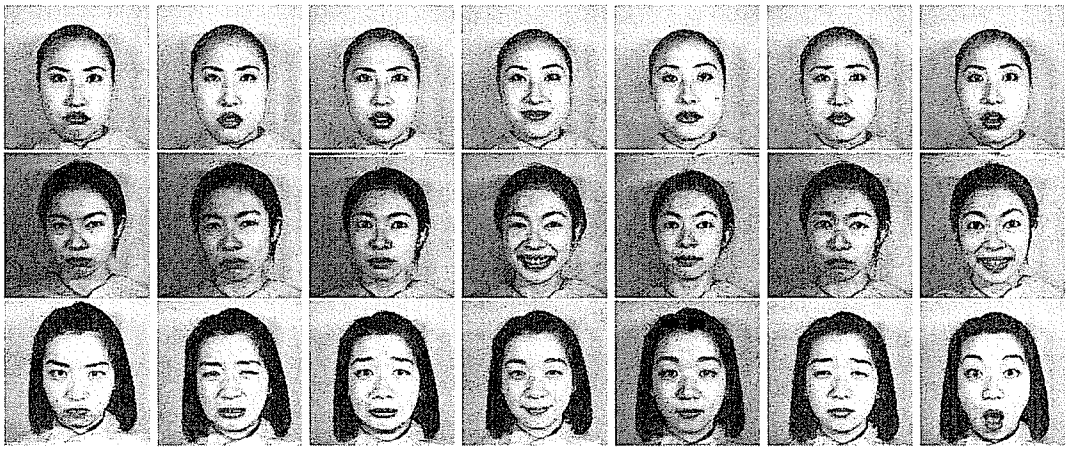

Figure 3.4 Some images in the face expression database. From left to right, the expressions are angry, disgust, fear, happy, neutral, sad, and surprise.

features. On the other hand, the frequency of occurrence of the 82 features over all pairs of classes was very variable, as shown by the histogram in Figure 3.5. The three most selected features are shown on the face in Figure 3.6.

Column 4 in Table 3.1 lists the number of classification errors out of 21 test examples by FSLP on each data set. The average over 10 runs was 1.9.

3.6.3 Comparison with SVMs

In order to verify whether the FSLP method has good performance or not in terms of recognition accuracy, we compared it with some other methods. Support Vector Machines [121] are known to give high recognition accuracy in practice, so we first compared FSLP with SVMs. The constant C in SVMs [121] was set to 100. The classification errors of both linear and non-linear SVMs (using all 612 features) in each run are shown in columns 5 and 6 of Table 3.1. For the non-linear SVM, we used the GRBF kernel and experimentally set the width parameter to its best value. The maximum error of FSLP was 3 over the 10 runs, which was never larger than the errors by linear SVMs and non-linear SVMs. The average number of errors over 10 runs was very similar for FSLP, linear SVM (1.6 errors) and non-linear SVM (1.7 errors). The corresponding recognition accuracies of the three methods were 91.0%, 92.4%, and 91.9%, respectively (see Table 3.2),

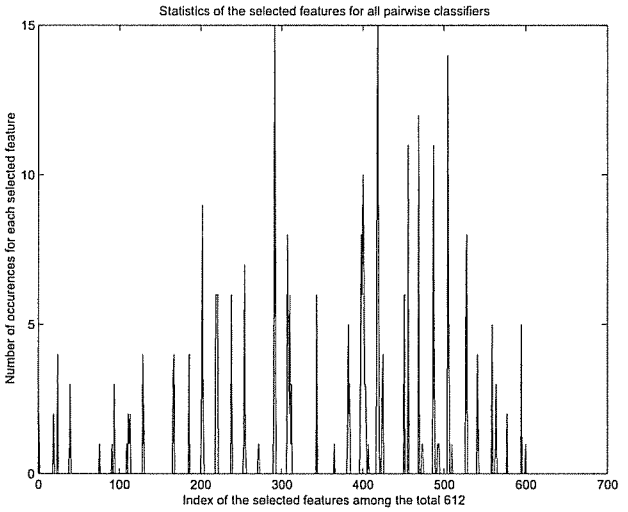

Figure 3.5 Histogram of the frequency of occurrence of the 612 features used in training Set 1 for all 21 pairwise FSLP classifiers.

which are comparable. Notice, however, that the average number of features selected by FSLP was 17.1, much less than that used by the SVMs. Furthermore, the computation time of FSLP was fast in both the training and recognition phases, with run times of several minutes to train all 21 classifiers on a Linux machine with a 1.2 GHz Pentium processor using a Matlab implementation and CPLEX 6.6 for the standard linear programming optimization.

While the recognition accuracy of SVMs is comparable to FSLP, one major weakness of SVMs is their high computational cost, which precludes real-time applications. In addition, SVMs are formulated as a quadratic programming problem and, therefore, it is difficult to use SVMs to do feature selection directly. (Some researchers have proposed approximations to SVM for feature selection [124] [10] by first training the SVM using the whole training set, and then computing approximations to reduce the number of features. This two-step approach cannot guarantee selection of the best feature subset, however.) Finally, SVM approximations [124] [10] cannot determine automatically how many features to use. On the contrary, FSLP addresses all of these issues at once.

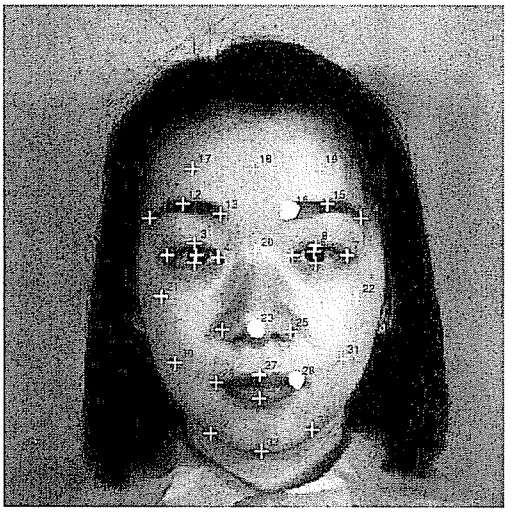

Figure 3.6 The three most used features (as in the histogram of Figure 3.5) are illustrated on the face: the corner of the left eyebrow, the nose tip, and the left mouth corner.

3.6.4 Comparison with AdaBoost and Bayes

Because one of our main goals was an evaluation of FSLP's feature selection process, we also compared the method with some greedy and heuristic methods for feature selection. The AdaBoost method [117] uses a greedy strategy to select features in the learning phase. The Bayes classifier that we used is a Naive Bayes classifier assuming features are independent. The greedy feature selection scheme can also be used by incrementally adding the most discriminating features [69]. Figure 3.7 shows the recognition performance of the AdaBoost and Naive Bayes classifiers as a function of the number of features selected. It is clear that less that 100 features are sufficient for both algorithms. The Naive Bayes classifier reached its best performance of 71.0% with 60 features, and the performance deteriorated slightly if more features were used. The recognition accuracy of the Naive Bayes classifier was 63.3% (shown in Table 3.2) when all 612 features were used. Overfitting the training data is a serious problem for the Naive Bayes method, so feature selection is necessary for it. Nevertheless, a simple greedy method does not give Naive Bayes much better accuracy. For the AdaBoost method, peak performance was 71.9% using 80 features (see Table 3.2) for each pair of classes. As shown in Figure 3.7, using more features slightly lowered recognition accuracy. In summary, both the AdaBoost and Naive Bayes classifiers combined with

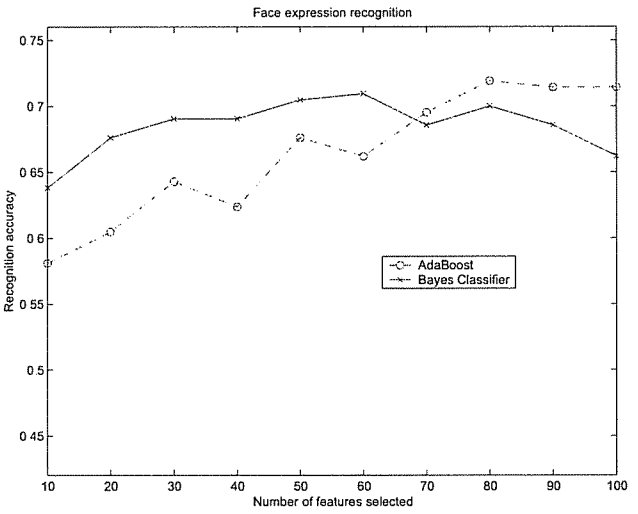

Figure 3.7 Recognition accuracies of a Naive Bayes classifier and Adaboost as a function of the number of features selected.

a greedy feature selection strategy needed to use a larger number of features than FSLP, and their recognition accuracies were much worse than FSLP.

3.6.5 Comparison with Neural Nets and LDA

We also compared the recognition performance of FSLP with other published methods [134] [133] [75] that used the same database. In [134] [133] a Neural Network was used with 90.1% recognition accuracy. When some problematic images in the database were discarded, the accuracy was 92.2%. In [75] a result of 92% using linear discriminant analysis (LDA) was reported, but they only included nine people's face images and, hence, only 193 of the 213 images were used. In conclusion, FSLP gives comparable results to Neural Network and LDA methods, but FSLP optimally selects a small number of features automatically, which is especially important for real-time applications.

3.7 Summary

This chapter introduced a linear programming technique called FSLP for jointly accomplishing optimal feature selection and classifier training, and demonstrated its performance for face

expression recognition. There are four main properties of this method that make it advantageous over existing methods: (1) FSLP can determine how many features to use automatically without any user interaction; (2) FSLP gives high recognition performance, comparable with linear SVMs, non-linear SVMs, Neural Networks, and LDA, and much better than AdaBoost and Naive Bayes classifiers; (3) FSLP avoids the *curse of dimensionality* problem, which often occurs when the amount of training data is small [59]; and (4) FSLP feature selection is fast to compute.

Table 3.1 The performance of FSLP compared to a linear SVM (L-SVM) and a GRBF non-linear SVM (NL-SVM) using 10-fold cross-validation. The average number of selected features (Ave. #) for each pairwise classifier and the total number of selected features (Total #) used for all pairs are shown in addition to the number of errors out of 21 test examples in each run.

Test	Ave. #	Total #	FSLP	L-SVM	NL-SVM
Set 1	16.8	82	3	2	1
Set 2	17.0	84	2	2	2
Set 3	17.1	90	1	1	2
Set 4	16.4	92	3	3	3
Set 5	16.0	83	1	2	2
Set 6	19.1	102	2	2	2
Set 7	16.9	85	2	2	2
Set 8	17.2	91	1	0	0
Set 9	17.5	91	2	1	2
Set 10	17.4	89	2	1	1
Ave.	17.1	88.9	1.9	1.6	1.7

Table 3.2 Comparison of the recognition accuracy and the number of features used by the Naive Bayes classifier without feature selection (Bayes All), Naive Bayes with pairwise-greedy feature selection (Bayes FS), AdaBoost, linear SVM (L-SVM), non-linear SVM (NL-SVM), and FSLP.

	Bayes All	Bayes FS	AdaBoost	L-SVM	NL-SVM	FSLP
Accuracy	63.3%	71.0%	71.9%	92.4%	91.9%	91.0%
# Features	612	60	80	612	612	17.1

Chapter 4

Iris Recognition

A wide variety of systems require reliable person identification or verification. Biometric technology overcomes many of the disadvantages of conventional identification and verification techniques such as keys, ID cards and passwords. Biometrics refers to the automatic recognition of individuals based on their physiological and/or behavioral characteristics [61]. There are many possible features to use as biometric cues, including face, fingerprint, hand geometry, handwriting, iris, retinal vein, and voice. Among all these features, iris recognition has very high accuracy [81]. The complex iris texture carries very distinctive information. Even the irises of identical twins are different [25] [61].

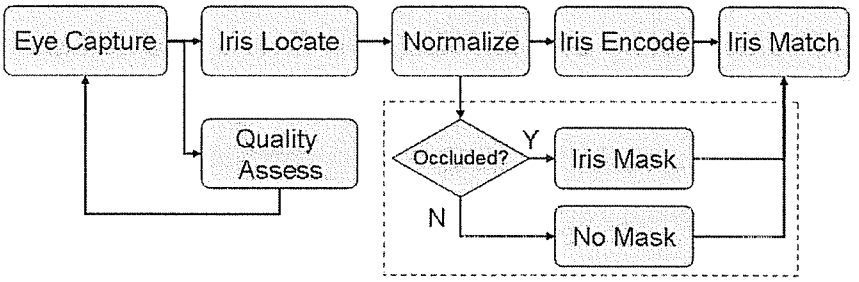

Figure 4.1 The steps in an iris recognition system. See text for details on each part.

An iris recognition system begins with eye image capture, as shown in Figure 4.1. The captured images may undergo quality assessment [26] to check their usability. If the eye image is good enough for recognition, the system first locates the iris in the captured image. This is a very important step for iris recognition. If the iris cannot be localized correctly, the system will fail in

recognizing the person. The correctly localized irises are then normalized into rectangular images called unwrapped images [26] with a predefined size. Iris features are then extracted from the unwrapped images and used for iris matching. Because of possible eyelid occlusions, some recent work also removes eyelids by computing a mask image [25]. Typical approaches detect eyelid boundaries in the eye images. We propose to compute the mask in a different way that works on the unwrapped image as shown in the flow chart within the dashed box in Figure 4.1. This approach has advantages over previous methods and will be presented in detail later.

This chapter[1] is organized as follows. The motivation for our work is introduced in Section 4.1 and previous work is reviewed in Section 4.2. Then we design a new two-camera system to capture iris images automatically in Section 4.3, and present a new method for iris localization in Section 4.4. Finally, we describe a new method for iris encoding in Section 4.5. Experimental evaluations are performed for the three parts separately.

4.1 Motivation

Although the iris can provide high recognition accuracy, it is not easy to capture iris images in practice. Classical iris recognition systems, e.g., Daugman's and Wildes', need the users to adjust their eye positions in order to capture their irises [125]. Furthermore, existing systems require users to be close to the capturing apparatus [26] [126] [76]. Hence, design of an iris capturing system that works without user interaction is of great importance in practice.

A common observation about eye images is that the iris region is brighter than the pupil and darker than the sclera. As a result, almost all previous approaches to iris localization are based on the intensity gradient or edge information. These methods depend heavily on the strong intensity contrast between the pupil and iris and between the iris and sclera. However, these contrasts are not always strong enough for reliable iris localization in practice.

Our new observation is that the iris region has very different texture than the pupil and sclera. We believe that this texture difference is also useful for discrimination between the iris and pupil

[1] This work is in collaboration with Mike Jones at MERL.

and between the iris and sclera, especially when the intensity contrast is not strong enough for iris localization. In fact, the rich texture information in the iris is what is used for iris recognition.

Based on this observation, our goal is to develop a new technique that combines the texture difference between iris and sclera, and between iris and pupil together with the intensity contrast in order to improve iris localization performance.

4.2 Related Work

Since the problem of iris recognition consists of the three parts: iris capture, iris localization, and iris encoding, we now review the related work on these three parts separately.

4.2.1 Previous Work on Iris Capture

Two classical iris capture systems are Daugman's [26] and Wildes' [125]. Both systems require users to adjust their eye positions. Some recent systems use stereo computation, e.g., [88]. However, as reviewed by Brown et al. [11], any real-time stereo implementation makes use of special-purpose hardware such as digital signal processors (DSP) or field programmable gate arrays (FPGA), or uses single-instruction multiple-data (SIMD) coprocessors (e.g. Intel MMX).

Our effort is to develop a new system to capture iris images automatically without user interaction based on recent advances in real-time face detection [122] rather than doing complex stereo reconstruction. Furthermore, it works at a distance of over 1 meter from the user.

4.2.2 Previous Work on Iris Localization

Daugman [26] presented the first approach to computational iris recognition, including iris localization. He proposed an integro-differential operator (IDO) for locating the inner and outer boundaries of an iris via the following optimization,

$$\max_{(r,x_0,y_0)} \left| G_\sigma(r) * \frac{\partial}{\partial r} \oint_{r,x_0,y_0} \frac{I(x,y)}{2\pi r} ds \right| \qquad [4.1]$$

where $I(x,y)$ is an image containing an eye. The IDO searches over the image domain (x,y) for the maximum in the blurred partial derivative with respect to increasing radius r, of the normalized

contour integral of $I(x,y)$ along a circular arc ds of radius r and center coordinates (x_0, y_0). The symbol $*$ denotes convolution and $G_\sigma(r)$ is a smoothing function such as a Gaussian of scale σ.

Daugman's IDO actually behaves as a circular edge detector. The IDO searches for the gradient maxima over the 3D parameter space, so there are no threshold parameters required as in the Canny edge detector [14].

Later, Wildes [125] proposed detecting edges in iris images followed by use of a circular Hough transform [57] to localize iris boundaries. The Hough transform searches for the optimum parameters of

$$\max_{(r,x_0,y_0)} \sum_{j=1}^{n} h(x_j, y_j, x_0, y_0, r) \qquad [4.2]$$

where

$$h(x_j, y_j, x_0, y_0, r) = \begin{cases} 1, & if \;\; g(x_j, y_j, x_0, y_0, r) = 0 \\ 0, & otherwise \end{cases}$$

with $g(x_j, y_j, x_0, y_0, r) = (x_j - x_0)^2 + (y_j - y_0)^2 - r^2$ for edge point $(x_j, y_j), j = 1, \cdots, n$.

One weak point of the edge detection and Hough transform approach is the use of thresholds in edge detection. Different settings of threshold values may result in different edges that in turn affect the Hough transform results significantly [94].

Recently, some other methods have been proposed for iris localization. But most of them are minor variants of Daugman's IDO or Wildes' combination of edge detection and Hough transform, that either constrain the parameter search range or speed up the search process. For example, Ma *et al.* [76] estimated the pupil position using pixel intensity value projections and thresholding, followed by Canny edge detection and a circular Hough transform. Masek [84] implemented an edge detection method slightly different from the Canny operator [14], and then used a circular Hough transform for iris boundary extraction. Cui et al. [22] computed a wavelet transform and then used the Hough transform to locate the iris' inner boundary, while using Daugman's IDO for the outer boundary. Rad *et al.* [97] used gradient vector pairs at various directions to coarsely estimate positions of the circle and then used Daugman's IDO to refine the iris boundaries. Kim *et al.* [62] used mixtures of three Gaussian distributions to coarsely segment eye images into dark, intermediate, and bright regions, and then used a Hough transform for iris localization.

All previous work on iris localization used only image gradient information and the rate of iris extraction is not high in practice. For example, Daugman's and Wildes' methods can only extract about $85 \sim 88\%$ of the iris patterns in the CASIA iris database [17].

4.2.3 Previous Work on Iris Feature Extraction

Daugman was the first to present a complete iris recognition system [26]. In it, the iris is localized by an integro-differential operator and unwrapped into a rectangular image; then a set of 2D Gabor filters were applied to the unwrapped image and the quantized local phase angles were used for iris encoding. The resulting binary feature vector is called the iris code [26]. Two binary iris codes are matched using the Hamming distance. Wildes proposed another iris recognition system [125] where Laplacian of Gaussian filters were applied for iris feature extraction and the irises were matched using normalized cross-correlation. In [6], zero-crossings of the wavelet transform at various scales on a set of 1D iris rings were proposed for iris feature extraction. A 2D wavelet transform was used in [68] and quantized to form an 87-bit code. This method can not deal with the eye rotation problem, which is common in iris capture. Masek implemented an iris recognition system using a 1D log-Gabor filter [84] for binary iris code extraction.

Ma *et al.* [76] used two circular symmetric filters and computed the mean and standard deviation in small blocks for iris feature extraction, with feature dimension 1,536. The authors also compared different methods for iris feature extraction, and concluded that their method outperforms many others but is not as good as Daugman's iris code. Recently, a method based on local variation analysis using a 1D wavelet transform was proposed [77]. The authors reported that their method has comparable recognition accuracy to Daugman's iris code, but only evaluated it using 200 iris images. In addition, their method used 1D processing instead of 2D. In [113], a method was proposed to characterize the local gradient direction for iris feature extraction. They claimed that their method has recognition accuracy comparable to the iris code, but it was much more complicated to compute and the extracted feature vector is 960 bytes, which is about 3 times bigger than the iris code.

In conclusion, Daugman's iris code method [26] is still the state-of-the-art algorithm in terms of recognition accuracy and computational complexity. Next, we develop a new method that is much simpler and faster to compute in 2D and has higher recognition accuracy than Daugman's iris code method.

4.3 Iris Capture

In this section we first introduce face anthropometry, which is the basis of our algorithm design. Second, we describe facial landmark detection on face images. Third, we present an algorithm for learning with detected facial landmarks. Fourth, we describe how to map from the face camera to the iris camera. In our system, the face camera is a video camera, and the iris camera is a high resolution digital still camera. Finally, we evaluate the system experimentally.

4.3.1 Face Anthropometry

Anthropometry is the biological science of human body measurement. Anthropometric data is used for many applications that depend on knowledge of the distribution of measurements across human populations. For example, in forensic anthropology, conjectures about likely measurements, derived from anthropometry, figure in the determination of individuals' appearance from their remains [35]; and in the recovery of missing children, by changing their appearance with age on photographs [35]. It has also been used recently for face model construction in computer graphics applications [28]. Here we use the property of anthropometric measurements to develop an algorithm for automatic iris acquisition.

Anthropometric evaluation begins with the identification of *landmark* points, as shown partially in Figure 4.2. All landmarks are named according to Greek or Latin anatomical terminology and are indicated by abbreviations [35]. For example, *ex* for *exocanthion*, the outer corner of the eye, *n* for *nasion*, the point in the midline of both the nasal root and the nasofrontal suture, and so on. A series of measurements between these landmarks is then taken using carefully specified procedures and measuring instruments. Farkas [35] described a widely used set of measurements for describing the human face. A large amount of anthropometric data is available in [35]. The

system uses a total of 47 landmarks and 132 measurements on the face and head. The measures used by Farkas [35] include distance and angles. The subjects were grouped by gender, race, and age. Means and standard deviations were measured for each group [35], capturing the variation that can occur in the group.

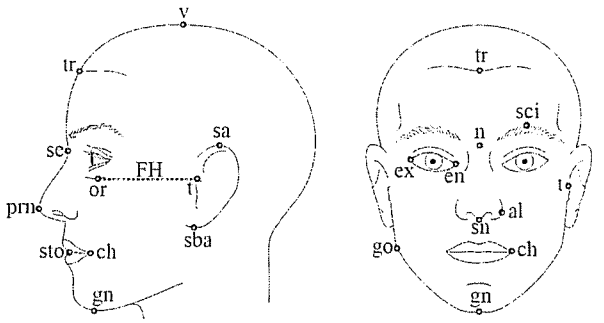

Figure 4.2 Anthropometric landmarks on the head and face.

Some anthropometric measurements obtained from [35] are listed in Table 4.1. In the table four distance measures are listed in terms of race, gender and age. *ex-ex* denotes the distance between the two outer eye corners, *ps-pi* the distance between the upper and lower eyelids, *al-al* the nose width, and *n-prn* the distance between the nasal root and the nose tip. Some useful information can be acquired from Table 4.1. For example, *ps-pi* is about $10mm$ with the standard deviation less than $1.5mm$, so the size of the iris is about $1cm$.

One observation from the anthropometric measures [35] is that the distance variations are small with respect to different race, gender, and age. For instance, the range of variation of *ex-ex* is about $1.2cm$ (from $80mm$ to $91.2mm$, corresponding to ages from 6 to 25 years old) for North American Caucasian males, and is about $1.9cm$ (from $77.8mm$ to $96.8mm$) over all races, genders, and ages. Considering the standard deviations, the maximum variation of *ex-ex* is less than $3cm$. This upper limit also holds for other distance measures on human faces [35]. In sum, the range of variations of distance measures between facial landmarks is quite small (e.g., less than $3cm$) over all races, genders, and ages. This observation is important for our iris capture algorithm.

Table 4.1 Some anthropometric measurements obtained from [35]. Means and standard deviations (SD) are measured for different groups in terms of race, gender, and age. "-" indicates unavailable from [35]. All distance measures are in millimeters.

Meas.	Age	North American Caucasian				Chinese				African-American			
		Male		Female		Male		Female		Male		Female	
		Mean	SD	Mean	SD	Mean	SD	Mean	SD	Mean	SD	Mean	SD
ex-ex	6	80.0	3.6	77.8	3.2	81.4	3.4	79.6	4.5	-	-	-	-
	12	85.6	3.0	83.6	3.4	87.2	3.8	84.6	4.0	-	-	-	-
	18	89.4	3.6	86.8	4.0	91.7	4.0	87.3	5.2	-	-	-	-
	19-25	91.2	3.0	87.8	3.2	-	-	-	-	96.8	4.6	92.9	5.3
ps-pi	6	9.5	1.0	9.4	0.8	8.6	0.9	8.8	0.8	-	-	-	-
	12	9.8	0.9	10.2	1.1	8.4	0.9	8.9	1.1	-	-	-	-
	18	10.4	1.1	11.1	1.2	9.4	0.7	9.5	1.2	-	-	-	-
	19-25	10.8	0.9	10.9	1.2	-	-	-	-	10.0	1.1	10.4	1.2
al-al	6	28.6	1.6	27.8	1.3	33.0	2.0	31.8	2.4	-	-	-	-
	12	31.6	1.9	30.9	2.1	36.2	2.3	36.1	2.3	-	-	-	-
	18	34.7	2.6	31.4	1.9	39.2	2.9	37.2	2.1	-	-	-	-
	19-25	34.9	2.1	31.4	2.0	-	-	-	-	44.1	3.4	40.1	3.2
n-prn	6	34.8	2.0	33.1	2.2	36.9	3.1	36.8	3.1	-	-	-	-
	12	42.8	3.2	42.0	3.1	40.4	2.9	41.7	3.7	-	-	-	-
	18	49.0	4.2	45.4	3.9	46.2	2.8	44.3	3.7	-	-	-	-
	19-25	50.0	3.6	44.7	3.4	-	-	-	-	45.6	3.5	42.6	3.7

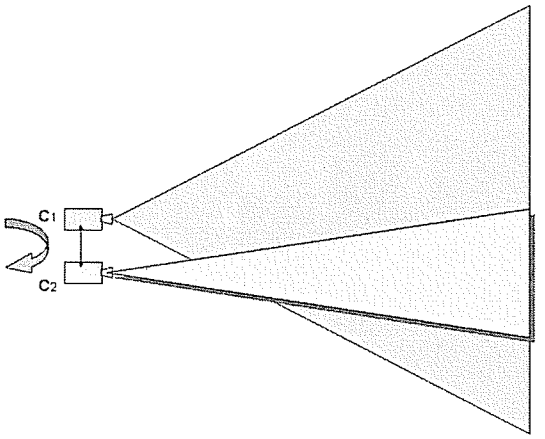

Figure 4.3 The two camera system setup. C_1 is the face camera with WFOV, while C_2 is the high resolution iris camera with NFOV. The two cameras are rigidly fixed together and are moved by a PTU.

4.3.2 System Setup

To demonstrate our anthropometry-based approach to automatic iris capture, we now present a prototype system using two cameras. The design of the two camera system is shown in Figure 4.3, and the 2-camera rig is shown in Figure 4.4. One camera is called the face camera and the other is called the iris camera. The face camera is a wide field of view, low-resolution video camera that captures and tracks the whole face continuously. In each frame the face and 9 facial landmarks are detected. The iris camera is a narrow field of view, high-resolution digital still camera, which is used to capture the iris region. The orientation of the iris camera is adjusted automatically to view the iris. A pan-tilt-unit (PTU) is controlled to rotate the iris camera so that it tracks the iris. The two cameras are close together (hence a very small baseline) with approximately parallel optical axes. This setting guarantees that if a face appears as a frontal view in one camera, it will also be an approximately frontal view in the other camera as well.

The system block diagram is shown in Figure 4.5. The basic operation of the system is to continuously detect a face in each frame of the video sequence captured by the face camera. When a face is found, facial landmark feature points are located and a tightly cropped bounding box around the eyes is computed. This eye region is mapped into the image plane of the iris camera.

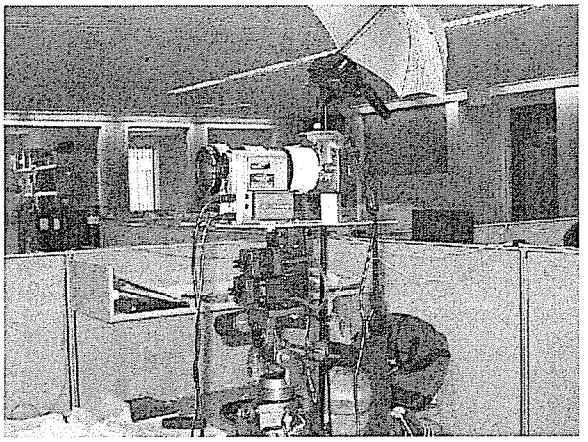

Figure 4.4 The MERL 2-camera rig.

If the eye region is well centered in the iris camera then an image of the eyes is captured. If the eye region is not well centered, then the PTU is used to pan and tilt both cameras until the eye region is approximately centered in the iris camera's image. The detection of faces and features and subsequent panning and tilting of the cameras iterates until the eye region is well centered in the iris camera's image.

4.3.3 Landmarks on Face Images

Unlike the anthropometric face model used in computer graphics [28] where face images are generated from anthropometric measurements [35], our work on automatic iris acquisition has to find landmarks on face images and use them to control iris capture. To detect facial landmarks, the algorithm first finds a face in the input images and then searches for landmarks within the face region.

4.3.3.1 Face Detection

To detect faces in real-time, we use a face detector proposed by Viola and Jones [122], which uses simple rectangle filters for feature extraction and the AdaBoost learning algorithm [42] for

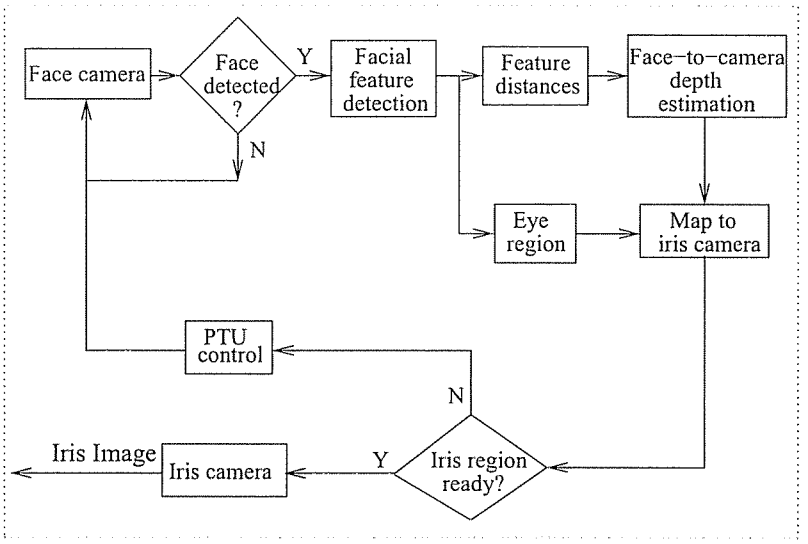

Figure 4.5 The system block diagram. The input is the video images and the output is the captured high resolution iris image. See text for details.

feature selection and classification. A large number of training examples (face and non-face images) are used by the AdaBoost learning algorithm. As a result, this face detector is very fast and robust.

4.3.3.2 Facial Feature Detection

When a face is detected, some facial features or landmarks can be detected within the face box. We use the same rectangle filters and AdaBoost learning algorithm as in face detection [122] but train the classifiers with templates characterizing different facial features, such as eye corners, nose tips, and so on. The training examples for each of the facial feature detectors are simply rectangular regions around each feature where each feature location has been precisely specified by hand. In practice, we found that usually 9 facial feature points can be detected robustly. They are the left and right outside eye corners, left and right eye centers, left and right nose corners, nose tip, center of upper lip, and the bridge of the nose. These features correspond to landmarks *ex*, *p*, *al*, *prn*, *ls*, and *n* in the anthropometric measures used by Farkas [35]. See Figures 4.6 and 4.7 for the nine detected features (each displayed with a white square).

The detected landmarks on face images are used to control iris image acquisition. Details on how to use the facial landmarks will be presented next.

4.3.4 Learning with Detected Facial Landmarks

Anthropometric measures [35] are used to guide iris acquisition: (1) Given face landmarks such as *ex* or *p*, we can compute the location of the iris region to capture. (2) The distances between facial landmarks can be used as a measure of how far the face is from the camera. The smaller the distance between landmarks, the farther the face is from the camera. Because of the small range of variation of anthropometric measures as discussed in Section 4.3.1, we can learn the relation between the distance measures of facial landmarks on face images and the distance of the face from the camera.

4.3.4.1 Eye Region via Facial Feature Points

To capture high resolution iris images, the system first needs to know where the eye region is. Facial features are used to determine the eye region. As shown in Figure 4.6, a simple strategy is to use the two eye corners to determine the eye region. Assuming the distance between two eye corners is d_1, let $W = 1.25 \times d_1$ and $H = 0.5 \times W$, where W and H are the width and height of the eye region, then we have $X_l = X_1 - \frac{5}{32} \times d_1$, $X_r = X_2 + \frac{5}{32} \times d_1$, $Y_l = Y_1 - \frac{5}{16} \times d_1$, and $Y_r = Y_2 + \frac{5}{16} \times d_1$, where (X_1, Y_1) and (X_2, Y_2) are the image coordinates of the left and right eye corners, and (X_l, Y_l) and (X_r, Y_r) are the coordinates of the upper-left and bottom-right corners of the eye region rectangle.

The location of the eye region in the low-resolution video image, I_1, can then be mapped to the high-resolution still camera image, I_2, using the technique presented in Sections 4.3.4.2 to 4.3.5.2.

4.3.4.2 Distance of Face to Camera

After a face is detected in the video frame, the system needs to know the distance of the face to the camera. This is so that the eye region can be mapped into the image plane of the iris camera to decide whether to capture an image or re-orient the camera using the pan-tilt unit.

Figure 4.6 Facial features detected determine the eye region in the video image. The outer box is the face detection result, while the inner rectangle is the computed eye region in the face image. d_1 is the Euclidean distance between two eye corners.

Here we present a technique that uses only the low-resolution face camera to compute the distance using facial features directly. This technique is based on the geometric optics of a pin-hole camera model: the image of an object is bigger if the object is closer to the camera, and vice versa. Using this property, a mapping from facial feature distances to depth values is computed.

Independent Linear Regression Assume we collect a data set of n faces at four different depths from the face camera. For each face we compute N facial feature distance measures. Let $d^i_{j,k}$, $1 \leq j \leq N$, $1 \leq i \leq n$ be the Euclidean distance between the j^{th} pair of feature points for face i at depth index k. D_k is the depth for index k, $1 \leq k \leq 4$. We use linear regression to map each feature distance, $d^i_{j,k}$ to the depth from the face camera :

$$a_j \cdot d^i_{j,k} + b_j = D_k.$$

To compute a_j and b_j for each distance feature j we need to solve a set of linear regressions

$$A_j \cdot X_j = 0 \qquad [4.3]$$

with

$$A_j = \begin{bmatrix} d_{j,1}^1 & 1 & -D_1 \\ \vdots & \vdots & \vdots \\ d_{j,1}^n & 1 & -D_1 \\ d_{j,2}^1 & 1 & -D_2 \\ \vdots & \vdots & \vdots \\ d_{j,2}^n & 1 & -D_2 \\ d_{j,3}^1 & 1 & -D_3 \\ \vdots & \vdots & \vdots \\ d_{j,3}^n & 1 & -D_3 \\ d_{j,4}^1 & 1 & -D_4 \\ \vdots & \vdots & \vdots \\ d_{j,4}^n & 1 & -D_4 \end{bmatrix} \quad [4.4]$$

and

$$X_j = \begin{bmatrix} a_j \\ b_j \\ 1 \end{bmatrix} \quad [4.5]$$

Hence, there is a different linear mapping from feature distance to camera depth for each different pair of features. It is straightforward to solve Eq. (4.3) using singular value decomposition.

Since each feature is processed independently, we call this method independent linear regression (ILR). To get a single depth estimate, all of the depth estimates are averaged. Thus, from a set of feature distances, $\{d_l\}$, the corresponding linear mappings for each feature distance are used to get a set of estimated depths, $\{\Delta_l\}$:

$$a_l \cdot d_l + b_l = \Delta_l, \quad l \in \{1, \cdots, L\} \quad [4.6]$$

$$\bar{\Delta} = \frac{1}{L} \sum_{l=1}^{L} \Delta_l \quad [4.7]$$

where L is the number of feature distance measures for a test face with $L \leq N$. When some features are not detected, $L < N$.

This results in a more robust estimate than using only the distance for a single pair of features. It also has the advantage of easily handling missing feature points. When a feature is not detected, the linear mapping for that distance is simply not used, and the depth estimates from all the other distance measures are averaged to yield a robust depth measure.

Using the ILR method, the procedure for depth estimation in both the learning and testing phases are given below.

Learning Phase

- Divide facial features into groups. In our case, nine facial feature points are detected in each face image. Because the image distance measure is sensitive to close feature points, the nine points are partitioned into 4 groups in order to get a robust estimate. See Figure 4.7 for an illustration.
- Compute the pairwise Euclidean distances from a point in one group to all points in other groups.
- Concatenate distance measures into a feature vector. In our case, 28 distance measures are computed given this 4-group-division of nine facial features. The resulting feature vector is of dimension 28.
- Repeat the above processes for various faces captured by the face camera at various depths to the cameras.
- Compute regression coefficients a_j and b_j using the ILR method.

Testing Phase For a new face, the system first detects the locations of the face and facial features. Then, the pairwise distance measures are computed with the same 4 group division as in the learning stage. The regression coefficients a_j and b_j are used to estimate the depth of the face to the camera using Equations (4.6) and (4.7). In practice, it is possible to use fewer than 28 distance measures (due to missing data), but the ILR algorithm can easily deal with this.

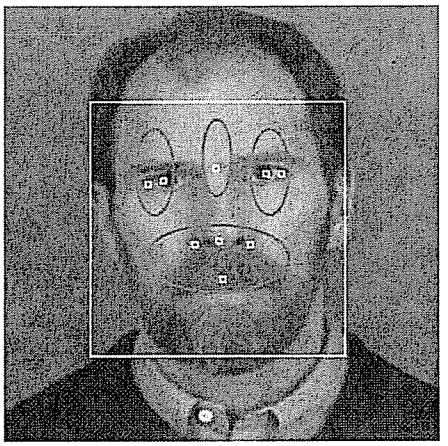

Figure 4.7 Facial features (9 white squares) detected within the face box. They are divided into 4 groups for pairwise feature distance measurement.

4.3.5 Mapping from Face Camera to Iris Camera

Using the ILR method with detected face landmarks, the system gets an estimate of the distance of the face to the cameras. This distance value will be used together with the pre-calibrated homographies (Section 4.3.5.1) and projective invariants (Section 4.3.5.2) to map the eye region in the image of the wide field of view face camera to the narrow field of view iris camera.

4.3.5.1 Camera-Camera Calibration

The goal of camera-camera calibration is to enable the eye positions detected in the video image to be mapped to estimated eye positions in the image plane of the iris camera. One way to achieve this would be to do a full Euclidean stereo calibration of the face camera and iris camera. Given full calibration and an estimate of the depth of the face from the face camera (see Section 4.3.4.2), it is straightforward to find the face position in the iris camera. But the iris camera that we use is autofocus, and a full Euclidean calibration would be difficult and expensive [127]. We adopt a simpler partial calibration that is sufficient for our goal.

First note that if the face is at a known depth d from the cameras, then the calibration is simple. A homography is computed for a fronto-parallel plane at depth d from the cameras. A plane is

an approximate model for the face, so the homography approximately describes the mapping of features on the face between the two cameras.

Now consider the case when the face is within some range of depths. The range is quantized, and a separate homography is computed for a fronto-parallel plane at each depth $d_1, d_2, \cdots, d_n$. At run-time, the distance d to the face is estimated, and the homography associated with the distance d_i that is closest to d could be used to provide the mapping of face features between the cameras. Alternatively, we can interpolate the calibrated homographies to find a mapping for facial features at depth d, as described in Section 4.3.5.2.

For computing the homography, we use a calibration plane with the pattern shown in Figure 4.8. The face camera captures the full pattern, and feature points are found automatically for the eight large squares. The iris camera has a narrower field of view and captures just the central three-by-three grid of small squares, and features points are found automatically for these squares. Knowing these image feature points and the Euclidean coordinates of the full pattern, it is straightforward to compute the homography, H_{VP}, between the video image and the pattern, and homography, H_{SP}, between the still image and the pattern, and hence the camera-camera homography $H_{VS} = H_{SP}^{-1} H_{VP}$ between the video image and the still image [55]. H_{VS} is a 3×3 matrix that describes the mapping of a homogeneous feature point x_v in the video image to a point x_s in the still image by

$$x_s = H_{VS} x_v \qquad [4.8]$$

As described above, the process is repeated for a set of depths of the calibration pattern from the cameras, to give a set of homographies $H_{VS1}, H_{VS2}, \cdots, H_{VSn}$.

4.3.5.2 Cross Ratio Projective Invariant

Assume at run-time the face is at depth d from the cameras. This section describes a simple technique to interpolate between the homographies H_{VSi} at depths d_i to determine a mapping between the face and iris cameras for features at depth d.

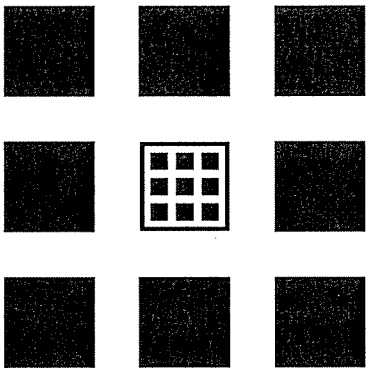

Figure 4.8 Calibration pattern used for computing the homography between two image planes. The wide-FOV face camera captures the entire pattern, while the narrow-FOV iris camera captures the central three-by-three grid of small squares.

The cross ratio of four numbers is invariant under a general homography [109]. For a line AD shown in Figure 4.9, the cross ratio is defined as $cr = \frac{AB}{BD} / \frac{AC}{CD}$, which equals $\frac{A'B'}{B'D'} / \frac{A'C'}{C'D'}$.

How do we use the cross ratio in our two camera system? In Figure 4.9, C_1 and C_2 are two camera centers. Let I_1 be the video camera's image plane, and I_2 be the iris camera's image plane. For any pixel in I_1, there is a viewing line, e.g., C_1A. If the homography from I_1 to I_2 at depth A is known, we can map the 3D point at A to A' in image I_2. Similarly, the 3D points at C and D can be mapped to C' and D', respectively, assuming the homographies at depths C and D are known. Suppose the homography at B is unknown. Using the technique in Section 4.3.4.2, the depth of B can be estimated. Now the cross ratio cr of A, B, C and D in line AD can be computed. Then the cross ratio cr is used for line $A'D'$ based on the invariant property.

Specifically, the coordinates of B', (x_b, y_b), in I_2 are obtained by

$$x_b = \frac{cr \cdot x_c \cdot x_d + (1 - cr) \cdot x_a \cdot x_d - x_a \cdot x_c}{x_d - (1 - cr) \cdot x_c - cr \cdot x_a} \quad [4.9]$$

$$y_b = \frac{cr \cdot y_c \cdot y_d + (1 - cr) \cdot y_a \cdot y_d - y_a \cdot y_c}{y_d - (1 - cr) \cdot y_c - cr \cdot y_a} \quad [4.10]$$

where (x_a, y_a), (x_c, y_c), (x_d, y_d) are the coordinates of A', C', and D' in image plane I_2, and they are computed using the pre-calibrated homographies at known depths A, C, and D. Although we

actually have four precomputed homographies at known depths, we only use three of them with the cross ratio.

In this way, any point in image I_1 can be mapped to I_2 at any depth to the cameras.

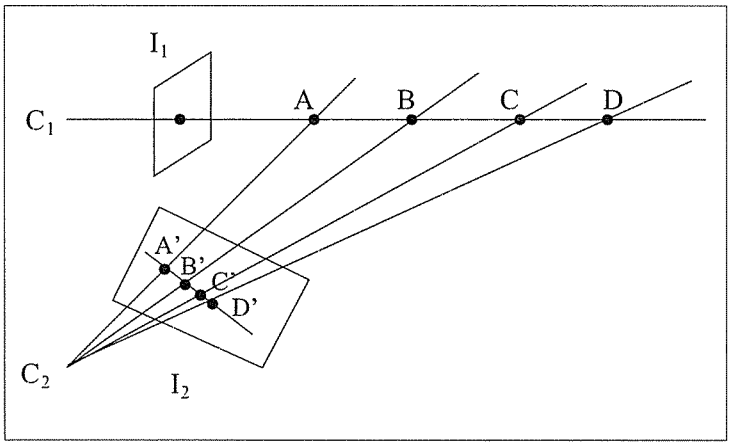

Figure 4.9 Cross ratio computation in the two camera system setup.

4.3.6 Experiments

For the face camera we used a Sony DCR-PC105 video camera with image resolution 640 × 480, focal length 3.7 to 37mm, and a field of view about 60 degrees. For the iris camera, we used a Canon Digital Rebel, which has a resolution of 3072 × 2048 (6 megapixels), a 200mm telephoto lens, EF70, and a field of view about 12 degrees. The minimum shooting distance for the telephoto lens is 1.2 meters, thus the iris images are captured at least 1.2 meters away.

To estimate the linear mapping from facial feature distances to camera depth described in Section 4.3.4.2, 10 people were asked to stand at approximately four different distances: 1.2, 1.5, 1.8, and 2.1 meters from the cameras. Then the face camera captured images of their faces. We captured a total of 40 face images - 4 images per person. Face detection and facial landmark detection was performed on each image. The ILR algorithm was then used to compute the linear mappings for depth.

To evaluate our depth estimation method, we randomly chose 5 of the 10 people as the training set to estimate the linear coefficients of ILR, and used the remaining 5 people for validation. The coefficients are used to estimate the depth of each person in the validation set given their facial feature measurements. The result on the validation set is shown in Figure 4.10(a), where each curve (corresponding to one person) is close to a straight line and the deviation is quite consistent. The main reason for the deviation is that we did not adjust each individual's distance exactly, so the "ground truth" is not exactly as listed. The mean and standard deviation of the depth estimation are shown in Figure 4.10(b). The four means are 1.28, 1.60, 1.87, and 2.04 meters, and the corresponding standard deviations are 0.08, 0.08, 0.04, and 0.01 meters. In fact our system *does not* require very accurate depth values. The linear mapping is adequate and works quite well. After validation, we re-computed the linear coefficients using all 10 individuals and used these for the capture system.

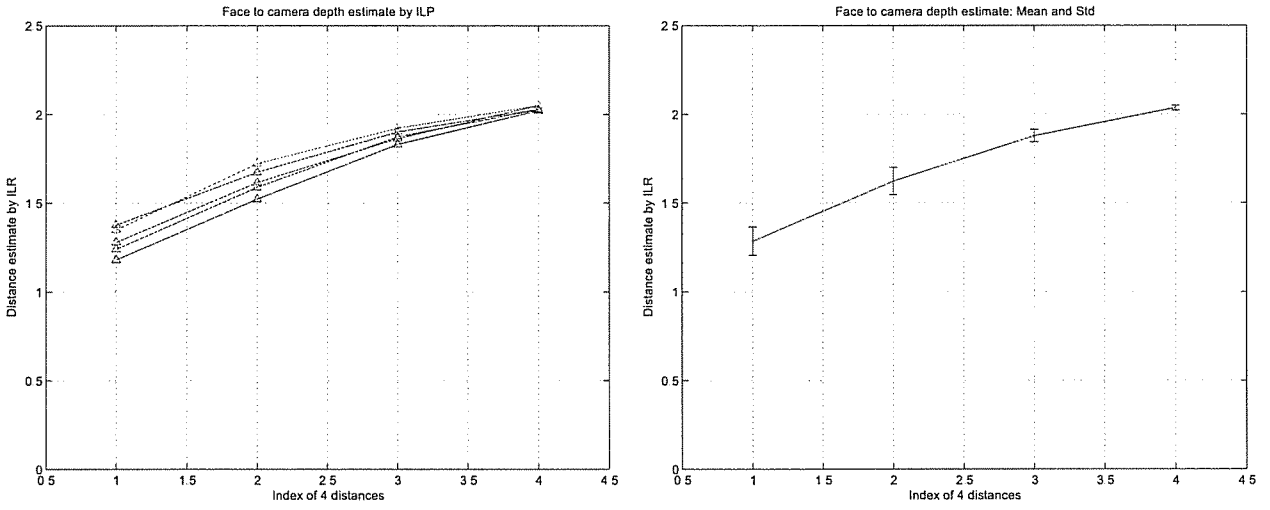

(a) (b)

Figure 4.10 Face to camera depth estimation on the validation set.

To compute the homographies at four different depths from the cameras, we put the calibration pattern at approximately the same four depths: 1.2, 1.5, 1.8, and 2.1 meters. The method described in Section 4.3.5.1 was then used to compute the homographies.

To determine the eye region based on facial features, five images were randomly chosen from the 40 images that were used for depth learning, and the relation of the eye region size and the distance between two eye corners was examined in the five images. We found the approximation shown in Section 4.3.4.1 works well in practice.

Finally, we tested the prototype system for iris capture. A user stands still in front of the cameras at a distance between 1.2 and 2.1 meters, and the system automatically pans and tilts if needed to capture high resolution images of both irises. Currently the system has captured about 20 people (excluding the 10 individuals used for training) without failure. For most of them, the two eyes are centered in the high-resolution images (note that this centering is done automatically by the pan-tilt unit without any user adjustment), while a few images were slightly shifted but this had no influence on extracting the two eyes. An example is shown in Figure 4.11 where the person's left eye is zoomed for visual inspection of the iris texture.

Figure 4.11 An example of the high-resolution eye regions captured by the iris camera (middle) and a digitally zoomed view of the left eye (right). The image captured by the wide-field-of-view face camera is shown in the left.

4.3.7 Summary

In this section we have presented an anthropometry-based approach to automatic iris acquisition without user interaction. The method detects facial landmarks and estimates the distance from the face to the camera. These techniques are fast and robust, involving only 2D images without

stereo reconstruction. To demonstrate the anthropometry-based method for iris capture, a prototype system was built using two cameras (i.e., face and iris cameras). The mapping between the two cameras is computed using projective invariants. Experimental results show that the prototype system works well.

4.4 Iris Localization

In this section we focus on improving iris localization accuracy and mask computation. A new approach to iris localization is presented in Section 4.4.1. We discuss a new issue called model selection and give a solution in Section 4.4.2. The mask image computation is presented in Section 4.4.3. Experimental results are given in Section 4.4.4.

4.4.1 Intensity Gradient and Texture Difference

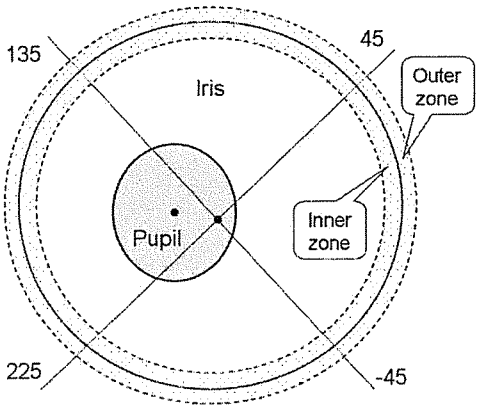

Figure 4.12 The inner and outer zones separated by a circle for iris/sclera boundary detection. The texture difference is measured between the inner and outer zones in addition to the intensity gradient for iris localization. Because of possible eyelid occlusion, the search is restricted to the left and right quadrants, i.e, -45 to 45 and 135 to 225 degrees. This figure also illustrates that the pupil and iris may not be concentric and the pupil/iris boundary is modeled by an ellipse instead of a circle.

Our approach to iris localization is to use features of both the intensity gradient and texture difference. The new formulation for iris localization is

$$(r^*, x_0^*, y_0^*) = \arg\max_{(r,x_0,y_0)} C(I, x_0, y_0, r) + \lambda\, T(Z_i, Z_o, x_0, y_0, r) \qquad [4.11]$$

where $C(I, x_0, y_0, r)$ is the intensity contrast or gradient over image domain $I(x, y)$ along a circle with center at coordinates (x_0, y_0) and radius r, and $T(Z_i, Z_o, x_0, y_0, r)$ measures the texture difference between an inner zone Z_i and an outer zone Z_o that are rings of pixels just inside and outside the circle boundary, respectively, as shown in Figure 4.12. The parameter λ is a constant to weight the contributions from intensity gradient and texture difference. Since the whole region inside or outside the circle is not necessarily homogeneous, e.g., the inner region of the iris/sclera boundary contains two different parts, pupil and iris, and therefore only a narrow zone next to the circular boundary is used to measure the texture property.

What is the specific form for each term in Eq. (4.11)? For the first term, i.e, intensity gradient or contrast, we use Daugman's integro-differential operator because the IDO encodes the image intensity gradient very well along a circular boundary. Thus we have

$$C(I, x_0, y_0, r) = \left| G_\sigma(r) * \frac{\partial}{\partial r} \oint_{r,x_0,y_0} \frac{I(x, y)}{2\pi r} ds \right| \qquad [4.12]$$

For the second term in Eq. (4.11), we use the Kullback-Leibler divergence (see Section 4.4.1.2) to measure the distance between two probability distributions derived from the inner and outer zones, respectively. Now the question is how to extract the texture information from each zone. One could use standard texture features such as those computed by Gabor filters, but filtering approaches usually need a large region of support that may cross the circular boundary. This is a general issue in texture segmentation where the regional property may be characterized well but the boundary between two textures can not be located precisely. In iris localization, accurate boundaries are needed to normalize and match iris images. Inaccurate iris localization deteriorates the iris recognition accuracy quickly no matter how discriminative the iris feature is. Consequently, to efficiently extract the texture properties without negatively influencing iris localization, we use a method called local binary pattern (LBP) with a small neighborhood.

4.4.1.1 Local Binary Pattern

The local binary pattern (LBP) operator is a simple yet powerful method of analyzing textures [78]. It was first proposed by Ojala *et al.* [90] for texture classification. The basic operation of LBP consists of three steps as shown in Figure 4.13: (1) thresholding the pixel values of all neighbors using the intensity value of the center pixel as the threshold, (2) weighting each neighbor with a value associated with a power of 2, and (3) summing the values of all neighbors and assigning this value to the center pixel.

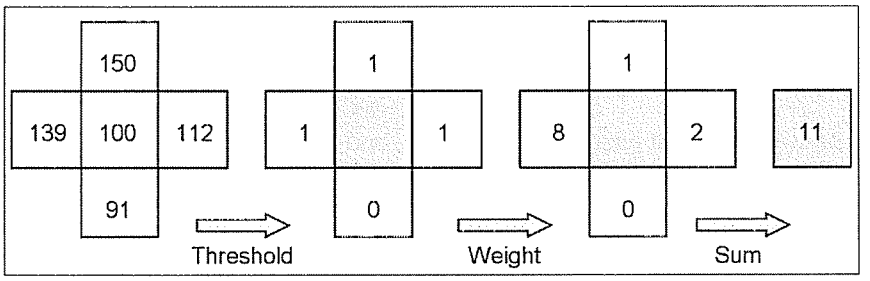

Figure 4.13 The LBP operator using four neighbors. Threshold the four neighbors with respect to the center pixel, weight each neighbor with a different power of 2, and sum the values to get a new value for the center pixel.

The pixels in a region of interest are encoded by new integers with the LBP operator. Then the histogram of these new integers for each zone is computed to represent its probability density function. In our case, a 4-neighborhood is used resulting in a new integer value for each center pixel between 0 and 15, so each histogram has 16 bins. The LBP operator is applied to the whole image once, while the histogram is computed dynamically during the search process.

The probability densities are computed for the inner and outer zones, denoted $p(x; Z_i)$ and $q(x; Z_o)$ respectively, or simply $p(x)$ and $q(x)$, where $x \in \{0, \cdots, 15\}$. The distance between two probability distributions is measured using KL-divergence.

4.4.1.2 KL-Divergence

Given two probability mass functions, $p(x)$ and $q(x)$, the Kullback-Leibler (KL) divergence (or relative entropy) between p and q is defined as

$$D(p||q) = \sum_x p(x) \log \frac{p(x)}{q(x)} \quad [4.13]$$

The KL-divergence $D(p||q)$ is always non-negative and is zero if and only if $p = q$. Even though it is not a true distance between distributions because it is not symmetric and does not satisfy the triangle inequality, it is still often useful to think of the KL-divergence as a "distance" between distributions [20].

As a result, the second term in Eq. (4.11) can be computed by the KL-divergence as

$$T(Z_i, Z_o, x_0, y_0, r) = D\left(p(x; Z_i)||q(x; Z_o)\right) \quad [4.14]$$

where Z_i and Z_o are the inner and outer zones separated by the circle (x_0, y_0, r). The probability densities $p(x; Z_i)$ and $q(x; Z_o)$ are represented by the histograms computed by the LBP operator.

4.4.1.3 Multi-Resolution Search

The optimization in Eq. (4.11) is a search problem. In order to reduce the search space and hence speed up the process, and also to avoid local maxima, we use a multi-resolution, coarse-to-fine technique. The original image is smoothed and down-sampled to a much smaller image and the optimum is found there. Then the search starts again in a finer image with the initial values set by the result obtained in the previous coarser resolution. The process repeats until reaching the finest resolution image. Note that the search in each resolution is restricted to the left and right quadrants because of possible eyelid occlusions [25] as shown in Figure 4.12.

4.4.2 Model Selection

Most approaches to iris localization use two circles to model the inner and outer boundaries of the iris. Using circles is simple to compute but may not fit the iris inner boundary well. Camus and Wildes [13] used an ellipse to model the pupil/iris boundary and a circle to model the iris/sclera

boundary. The ellipse model fits the inner boundary better than the circle whenever the boundary is not a true circle, but the problem is, the search will be in a 4D space instead of 3D. To search in a higher dimensional space will be slower and may be error prone.

What models should be used for iris boundaries? Should the inner/outer boundaries be modeled by circle/circle or ellipse/circle[2]? We call this the model selection problem. And we believe that model selection should be data-driven rather than assigned beforehand.

Our scheme is a two-step approach. First, the circle/circle model is used to approximate the inner/outer iris boundaries. Second, within a region slightly bigger than the inner circle, do the following: (1) detect edges using the Canny edge detector [14], (2) generate chain codes for the detected edge points using 8-connectivity [43], (3) choose the longest contour from all generated chains to eliminate outliers of edge points, (4) fit an ellipse to the chosen contour using a direct ellipse-fitting method [38], (5) compute the eccentricity e of the fitted ellipse, and (6) decide whether to use an ellipse or circle to model the inner iris boundary with the criterion that, if $e > e_T$, choose an ellipse, otherwise, use a circle.

Theoretically, the ellipse model also fits a circular shape. So why choose between an ellipse and a circle? The reason is that the circle model makes it simple to unwrap the iris image into a rectangular image.

The eccentricity $e \equiv \sqrt{1 - \frac{b^2}{a^2}}$ for an ellipse $\frac{(x-x_0)^2}{a^2} + \frac{(y-y_0)^2}{b^2} = 1$. Theoretically, the eccentricity satisfies $0 \leq e < 1$ with $e = 0$ in the case of a circle. Note that the standard ellipse has the major and minor axes consistent with the x and y axes, while the fitted ellipses in iris images may be rotated by an angle. The direct ellipse-fitting method [38] solves a generalized eigenvalue system to estimate the ellipse parameters. It does not involve any iterative computation and thus is very fast.

To show the necessity of ellipse fitting for real iris images, Figure 4.14 shows an example image from the CASIA iris database [17] localized by different methods. The results in the left and middle images were obtained using the Hough transform and the IDO, respectively, assuming

[2]We do not consider an ellipse/ellipse model because a circle usually fits the visible portion of the outer boundary well.

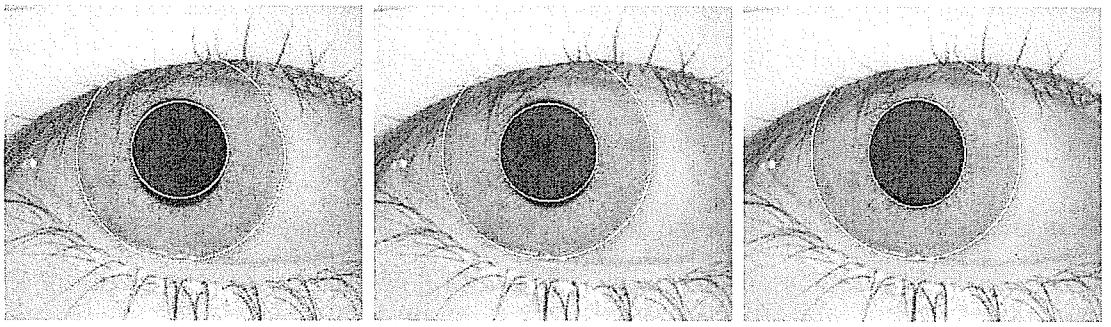

Figure 4.14 Demonstrate that the circle model is not accurate for the iris inner boundary. The iris image (105_1_1) uses a circle model to fit by Hough transform (left) and integro-differential operator (middle). The right image shows the result based on direct ellipse fitting. All circles and ellipse are drawn with one pixel wide white line.

a circle model for the inner boundary. It is obvious that a circle does not fit the pupil/iris boundary well. The result in the right image uses direct ellipse fitting and the boundary is fitted precisely.

4.4.3 Mask Computation

The iris may be partially occluded by the upper or lower eyelids. Because of this problem, Daugman [26] excluded the top and bottom parts of the iris for iris feature extraction and recognition. But this will ignore useful information when very little or no eyelid occlusion exists. As argued by Wildes [125], explicit modeling of the eyelids should allow for better use of available information than simply omitting the top and bottom of the iris. In [25], Daugman used curves with spline fitting to explicitly search for the eyelid boundaries. Cui *et al.* [22] used a parabolic model for the eyelids and fit them separately. The upper eyelid is searched for within the eyelash region, while the lower eyelid is searched for from detected edge points. Masek used straight lines to approximate the eyelids [84], which usually results in a larger mask than necessary.

Almost all previous work explicitly estimates eyelid boundaries in the original eye images. This approach has some problems in practice however: (1) the search range for eyelids is usually large, making the process slow, and (2) the eyelids are always estimated even when they do not occlude the iris. To address these issues, we propose to compute the eyelid occlusion in the unwrapped

rectangular image rather than in the original eye image. The eyelid region looks like a dome in the unwrapped image, as shown in Figure 4.15 (b) and (c), so we call it a dome model.

4.4.3.1 Dome Model

There are three possible cases for the domes in an unwrapped image, as shown in Figure 4.15: (a) no dome, where there is no eyelid occlusion, (b) one dome, where only the upper or lower eyelid occludes, and (c) two domes, where both upper and lower eyelids occlude the iris.

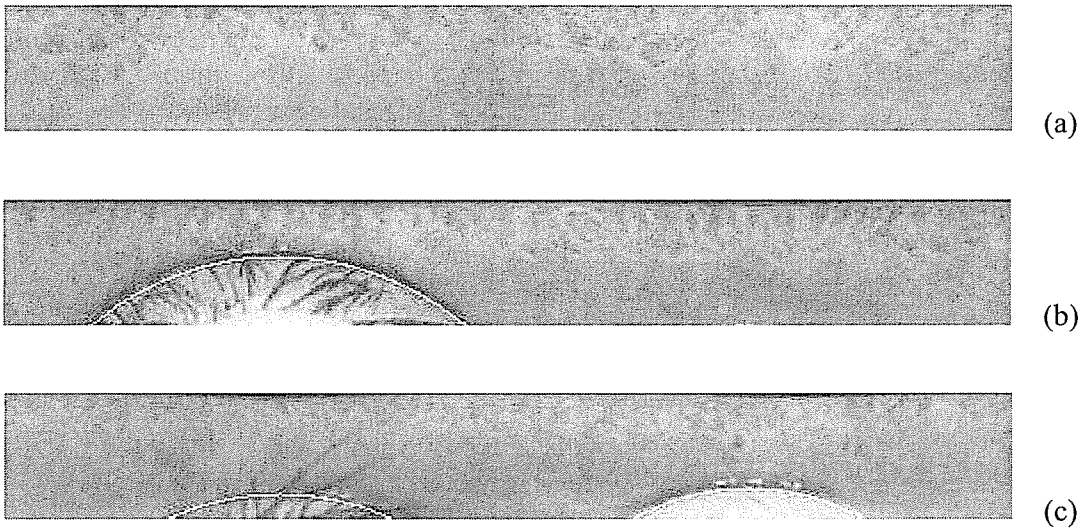

Figure 4.15 The dome model of three possible cases: (a) none , (b) only one dome, and (c) two domes. The dome boundaries are drawn with white curves.

Using the dome model, occlusions from either the upper or lower eyelids can be processed in a unified way. To extract the domes, a circle model is used instead of complex models such as splines [25] and parabolas [22], or a rough model of straight lines [84].

Our approach is a least commitment strategy. The algorithm first determines whether eyelid occlusions exist or not. If no occlusion exists, such as in Figure 4.15 (a), there is no need to detect dome boundaries. When occlusions do exist, the algorithm determines how many domes (1 or 2), and then detects them. The algorithm also has a post-processing stage that reduces false alarms.

To detect possible eyelid occlusions in the unwrapped image, the region of the iris where an eyelid might appear is compared to a region where occlusion cannot occur. These regions are compared by looking at their distributions of raw pixel values. The Chi-squared distance measure is used to compare the histograms of raw pixel values in the two regions,

$$\chi^2(M,N) = \sum_{b=1}^{B} \frac{(M_b - N_b)^2}{M_b + N_b} \qquad [4.15]$$

where M and N are two histograms, each with B bins.

The iris mask computation consists of six steps:

1. Extract three regions in the unwrapped image, denoted as R_l, R_m, and R_r, approximately corresponding to the upper eyelid, part without occlusion (e.g., the region between 135 and 225 degrees in Figure 4.12), and lower eyelid, respectively, in the original eye images.

2. Compute the histogram of pixel values in each region, denoted H_l, H_m, and H_r.

3. Compute $\chi^2(H_m, H_l)$ and $\chi^2(H_m, H_r)$ using Eq. (4.15).

4. Decide whether there are occlusions or not and, if so, how many domes, by testing if $\chi^2(H_m, H_l) > T_o$ and $\chi^2(H_m, H_r) > T_o$, where T_o is a threshold.

5. Search the dome regions if necessary using Eq. (4.11). Note that now the circle center is below the unwrapped image and only the top arc of the circle is fit to the eyelid.

6. Remove false alarms by checking whether the maximum value of a detected dome satisfies $C(I, x_0^*, y_0^*, r^*) + \lambda\, S(Z_i, Z_o, x_0^*, y_0^*, r^*) > T_c$, where T_c is a threshold and (x_0^*, y_0^*, r^*) is the circle for the dome. If not, the extracted dome is a false alarm.

4.4.4 Experiments

To evaluate our proposed method for iris extraction, we used the CASIA iris database [17] that contains 756 iris images in 108 iris classes. For all iris images shown in this section, original image names are also given for reference.

Table 4.2 Comparison of iris detection rates between different methods using the CASIA database.

Hough Transform (Wildes)	Integro-differential Operator (Daugman)	Gradient & Structure (new method)
85.6%	88%	97.6%

4.4.4.1 Experimental Results

First, we evaluate the iris localization rate. In Eq. (4.11), λ was set to 0.1 to balance the intensity gradient and texture difference between the inner and outer zones. Pixel gradient values were normalized to $(0, 1)$. In Eq. (4.12), the central difference approximation is used for gradient estimation with two pixel intervals. To measure the texture information with the LBP operator, a 4-neighborhood was used for each pixel. This small neighborhood helps the boundary localization precision. The inner and outer zones are both 4 pixels wide along the radial direction so that enough information is available for structure estimation but the computational load is low. The KL-divergence is computed only for bins x with $p(x) \cdot q(x) \neq 0$.

Iris localization results are shown in Table 4.2. Our method, which combines intensity gradient and texture difference, located 97.6% irises correctly on the CASIA database, which is much better than Wildes' Hough transform technique (85.6%) and Daugman's integro-differential operator (88%). The correctness of the iris boundaries were determined by manual inspection.

Some examples are shown in Figure 4.16 to show the localization results obtained by the different methods. The upper row in Figure 4.16 shows the results for image 037_2_4. The intensity contrast between the iris and sclera is not strong and the detected edges are weak, so the Hough transform (left image) does not find the true boundary. The IDO method (middle) gets weak gradient information, especially in the left part of the iris, so the detected circle is shifted away from the true boundary. In contrast, our method can deal with the case of weak edges and gives an accurate boundary for the iris (right image, upper row). Similar analysis holds for the example in the lower row in Figure 4.16 (image 039_2_1).

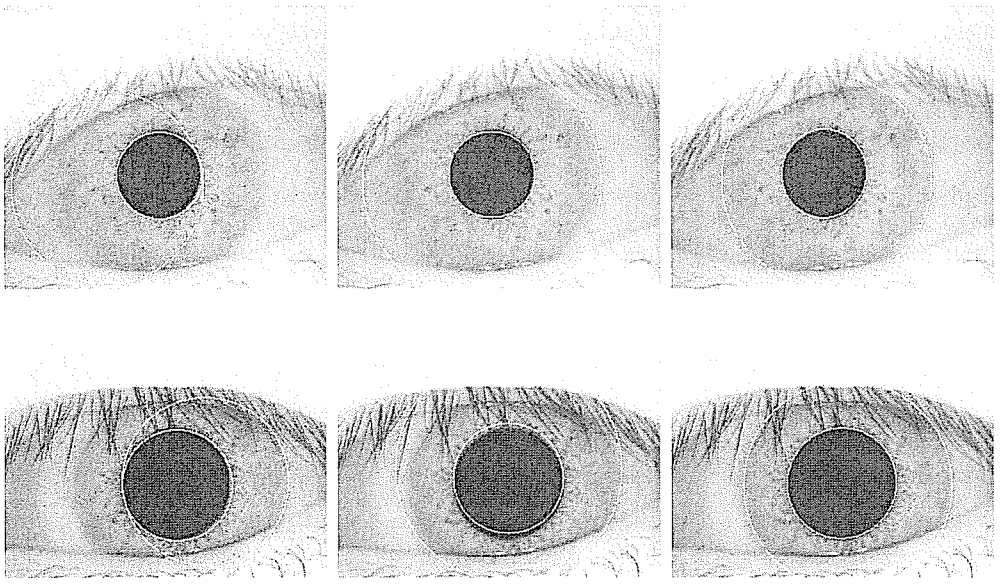

Figure 4.16 Comparison between different techniques for iris boundary extraction. From left to right, the results are based on the Hough transform, integro-differential operator, and the proposed new method. The iris images are 037_2_4 (first row) and 039_2_1 (second row).

Second, we evaluate the model selection method. Because the camera viewing direction is not perpendicular to the eye, perspective makes the projection of the pupil not a circle. In addition, the eyes can move freely to a certain degree. As a result, the ellipse/circle model is better than the circle/circle model for iris localization in some cases. We found that there were 75.7% (572/756) iris images with eccentricity $e > 0.19$, where 0.19 is the threshold value chosen to determine whether to use the ellipse/circle model or not. Our approach is the first to use the circle/circle model to search for iris boundaries, and then use direct ellipse fitting for detecting the inner boundary without turning to a 4D search. As shown in Figure 4.14, for image 105_1_1, both the Hough transform (left) and IDO (middle) methods do not work well when the circle model is used for the inner boundary. On the contrary, ellipse fitting (right) gives a much better result for the pupil/iris boundary.

Third, we evaluate our new mask computation method. As discussed in Section 4.4.3, the mask image is computed in the unwrapped images instead of the original eye images. The unwrapped image is of size 512×64 (see [26] [76] for details on how to unwrap iris images). Our approach

first determines whether there is any eyelid occlusion in the unwrapped image. If not, there is no need to compute a mask. Three regions of size 40 by 20 pixels are obtained, starting from the image bottom. The middle region, R_m, is centered at 256, representing the part of the iris that is never occluded by the eyelids. The left region, R_l, is centered at 128, and the right region, R_r, is at 384. Their histograms, H_l, H_m, and H_r, are computed using 32 bins. Then the χ^2 distance is computed using Eq. (4.15). The threshold value $T_o = 0.26$ was set empirically. The left dome exists if $\chi^2(H_m, H_l) > 0.26$. Similarly, the right dome exists if $\chi^2(H_m, H_r) > 0.26$. Otherwise, there are no domes detected.

In finding domes, a small search range can be used, which is one of the advantages of computing the mask in the unwrapped images. For the left dome, the horizontal search range is 15 pixels to the left and right, centered at $x = 128$. The same range is used for the right dome, but centered at $x = 384$. The vertical search range is $(64 + 15, 512)$, and the search range of radius r is $(128 - 15, 200)$. To remove false alarms, the maximum value for each detected dome is checked to see if it satisfies $C(I, x_0^*, y_0^*, r^*) + \lambda\, S(Z_i, Z_o, x_0^*, y_0^*, r^*) > T_c$ with $T_c = 13.5$ set empirically. If not, the detected dome is a false alarm.

In the CASIA iris database, our method extracted the domes with an accuracy of 93%. We found that almost all domes were detected, but the dome boundaries were not accurate for 7% (53/756) of the images.

4.4.4.2 Comparison of Results

There has been some recent work on iris localization. Masek [84] reported 82.5% iris localization rate on the CASIA database using the Hough transform. A comparison of different methods was presented in [94] where the Hough transform gave 86.49% localization rate on CASIA. Daugman's IDO method had 83% localization rate on CASIA [97]. All these reported results are comparable with our own implementation given in Table 4.2, where the Hough transform has 85.6%, and the IDO has 88% localization rates on the CASIA database. In contrast, our method gives 97.6% iris localization rate, which is much better than previous methods.

In [22], the authors reported some results on the CASIA database in which the IDO method had 98.6% and the Hough transform 99.9% localization rates. It is not clear how Cui et al. achieved such good results since our implementations as well as other published work show poorer results.

Unwrapped images were also used in [97] to compute masks, but they did not give any details on it, nor did they explain why they used unwrapped images, and they did not report any mask extraction accuracy either.

So far, we have not mentioned the problem of eyelash and highlight removal. In [63] Gabor filtering was used for eyelash detection but this method has not been verified with a large iris database such as CASIA. In [84] a simple thresholding method was used for eyelash removal on CASIA but the method is not general for other imaging conditions. Both [63] and [84] used thresholding for highlight removal.

4.4.5 Summary

We presented a novel method for iris localization that utilizes both the intensity gradient and texture difference between the iris and sclera and between the pupil and iris. The iris localization rate using this method is much higher than existing techniques using the Hough transform and the integro-differential operator. We considered the model selection problem and proposed a solution based on direct ellipse fitting. Finally, we presented a novel approach to mask computation in the unwrapped image. The new procedure follows a least commitment strategy that triggers a dome detection process only when necessary.

4.5 Iris Encoding

In this section, a new method for iris feature encoding is presented. A new set of filters is proposed for iris encoding in Section 4.5.1. The advantages of using these filters are discussed in Section 4.5.2. Experimental results are shown in Section 4.5.3 and compared with other methods.

4.5.1 Difference-of-Sum Filters for Iris Encoding

A new set of filters, called difference-of-sum (DoS) filters, is introduced to encode iris features. First, the basics of DoS filters are described. Second, a bank of DoS filters is designed specifically for iris encoding. Third, the filtered results are binarized for robustness and compactness. Fourth, an intermediate representation, called an integral image, is computed that makes DoS filtering extremely fast. Finally, we describe how to apply DoS filters to unwrapped iris images.

4.5.1.1 Basic Shapes of DoS Filters

There are two basic shapes of DoS filters for iris encoding, one is odd symmetric and the other is even symmetric, as shown in Figure 4.17 in the one-dimensional case. Because the filter function $f(x)$ only has values of +1 and -1 in its support, convolving $f(x)$ with any 1D signal computes the difference between the sums of the 1D signal associated with the positive and negative parts of $f(x)$. Consequently, they are called the difference of sum (DoS) filters [50]. The odd symmetric filter, as shown in Figure 4.17(a), is similar to the Haar wavelet. Both the odd and even symmetric filters have zero sum in order to eliminate sensitivity of the filter response to absolute intensity values. This is realized without effort for DoS filters, unlike Gabor filters where the even components have to be biased carefully.

The basic shapes of the DoS filters in 2D are shown as the top pair in Figure 4.18.

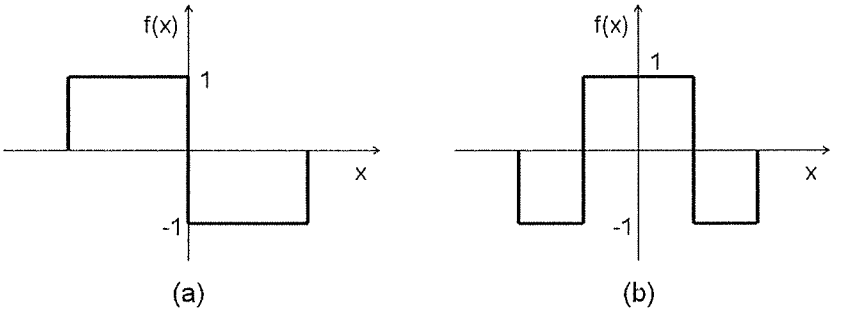

Figure 4.17 Basic shapes of the difference of sum(DoS) filters in 1D, (a) odd symmetric, and (b) even symmetric.

4.5.1.2 A Bank of DoS Filters

For iris feature extraction, a bank of two-dimensional DoS filters was designed and is shown in Figure 4.18. The set of DoS filters have the same height but various widths. We call this special design purely horizontal scaling (PHS). We found that scaling the filters in both the horizontal and vertical directions degrades recognition performance. One possible reason is that the iris patterns may have different dependencies in the radial and angular directions [84]. As shown in Figure 4.18, four pairs of odd and even symmetric DoS filters with various widths are used for iris encoding.

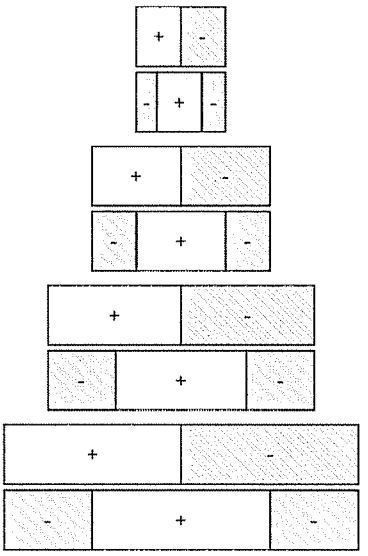

Figure 4.18 A bank of 2D DoS filters with multiple scales in the horizontal direction (purely horizontal scaling). All filters have the same height. This special design is of benefit for iris feature extraction from unwrapped iris images.

The set of DoS filters is designed to extract iris features at multiple scales. The sizes of the filters were adjusted based on experiments.

4.5.1.3 Binarization

The unwrapped iris images are filtered with the set of DoS filters and the output is real valued. A sign function is then used to binarize the filtered values.

The reason for the binarization is to make the encoding robust. This is important because there are quite a few sources of noise in the iris pattern. For example, the irises may be captured at different viewing angles, the incident angles of the light source(s) may change, the iris localization may be not perfect, and so on. A binarized representation with a series of "1" and "0" bits improves the robustness in iris feature encoding. The binarization is similar to digitizing an analog signal. The alteration of an analog waveform is progressive and continuous, hence it is quite sensitive to noise. While a digital signal can be quite robust. In addition to improved robustness, it also creates a very compact signature of the iris pattern.

4.5.1.4 Fast Computation of DoS Filtering

The DoS filtering can be computed rapidly with a pre-computed integral image. Crow [21] first proposed "summed-area tables" for fast texture mapping. Viola and Jones [122] used a similar idea they called the "integral image" for rapid feature extraction in face detection. Here iris feature encoding using DoS filters can also take advantage of the integral image for fast computation.

The integral image at location x, y contains the sum of all the pixels above and to the left of x, y, inclusive:

$$ii(x,y) = \sum_{x' \leq x, y' \leq y} I(x', y'), \qquad [4.16]$$

where $ii(x,y)$ is the integral image and $I(x,y)$ is the original image. Summed row by row, the integral image can be computed quickly in one pass over the original image. Then any rectangular sum in the original image can be computed in four array references in the integral image as shown in Figure 4.19.

DoS filters are different from the rectangle filters used in face detection [122], although both use the integral image computation. The rectangle filters [122] exhaustively search all possible scalings of the base filters for discrimination between faces and non-faces, while DoS filters are designed for the special iris patterns in a predefined manner.

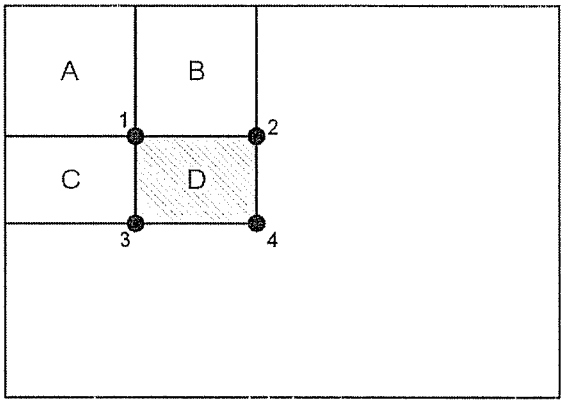

Figure 4.19 A rectangular sum over region D in the original image can be computed by $ii(4) + ii(1) - ii(2) - ii(3)$ in the integral image where each point contains a sum value.

4.5.1.5 DoS Filters Applied to Iris Images

To apply the set of DoS filters, an unwrapped iris image is divided into eight horizontal strips as shown in Figure 4.20. Then the filters are applied within each strip at intervals, with all DoS filters having the same height as each strip.

4.5.2 Advantages of DoS Filters

Before evaluating iris recognition performance using DoS filters we point out some advantages of DoS filters over Gabor filters [26]:

1. *Simple.* The DoS filters are very simple. There is no need to worry about any complicated implementation issues as in Gabor filter design.

2. *Fast.* Iris feature extraction with DoS filters is very fast. It is faster than using Gabor filters because the only required computation in DoS filtering is addition or subtraction without involving multiplication or division. Thus DoS filters can take advantage of the integral image representation which can be computed quickly in advance. Filtering using a DoS filter has constant computation time, no matter how big the filter is. With traditional filters the filtering time is proportional to the filter size – the bigger the filter, the slower the computation.

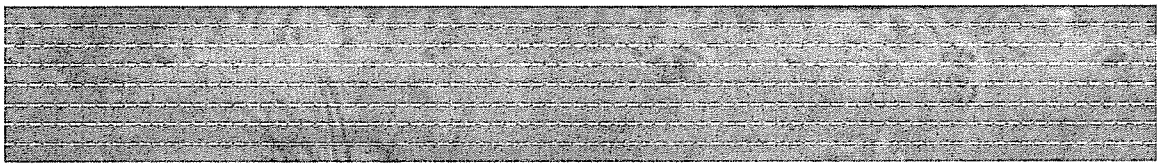

Figure 4.20 An unwrapped iris image is divided into eight horizontal strips before applying the DoS filters.

Table 4.3 Iris image database information

Database	#Eyes	Iris Localized	Localization Rate	Intra Comps.	Inter Comps.
CASIA	756	647	85.6%	1,759	207,222

3. *Few parameters*. In the design of the DoS filter bank, all parameters such as size (width and height) and shape (odd vs. even symmetric) are explicit, without many parameters. On the other hand, Daugman's iris code uses Gabor filters with many parameters, such as the aspect ratio, wavelength, and Gaussian envelope size.

4. *High accuracy*. Iris features extracted from DoS filtering are highly discriminative. As will be shown in Section 4.5.3, DoS features are better than Gabor features, which is the state-of-the-art method in terms of the recognition accuracy.

4.5.3 Experiments

To evaluate our method for iris feature encoding, we used the CASIA iris database [17] that contains 756 iris images in 108 classes. First, the irises are localized using the Hough transform [125]. The localization rate was about 85.6%. Then the detected irises are unwrapped into rectangular images and used for recognition. 1,759 intra-class comparisons and 207,222 inter-class comparisons, as given in Table 4.3, were computed.

Table 4.4 False accept rate (FAR) and false reject rate (FRR) with respect to different separation points for DoS filters and iris code on the CASIA iris database.

	Iris code		DoS filters	
Threshold	FRR	FAR	FRR	FAR
0.20	0.9449	0	0.8937	0
0.25	0.7362	0	0.6111	0
0.30	0.3428	0	0.2393	0
0.35	0.0608	9.65e-006	0.0262	0
0.40	**0**	**0.0039**	**0**	**0.0036**
0.45	0	0.5882	0	0.3344
0.50	0	1	0	0.9848
Decidability	4.7		5.3	

4.5.3.1 Fair Comparison of DoS Filters and the Iris Code

The DoS filters are compared with our own implementation of the iris code [26]. As argued in Section 4.5.2, the aspect ratio, wavelength, and Gaussian envelope size of the Gabor filters are unknown in Daugman's iris code [26] [25]. We tried various settings of these parameters and used the best ones in our implementation [26]. The unwrapped iris image is of size 512×64 and divided into eight rows. The DoS filters and Gabor filters were applied to each row at the same pixel positions for sampling. The input to both methods was exactly the same in order to do a fair comparison. The heights of all the DoS filters were 8 pixels, and the widths were $12 * n$ with $n = 1, 2, 3, 4$ for the 4 pairs of odd and even symmetric filters. For the iris code method using Gabor filters, the filter bandwidth used was 3 octaves. Various wavelengths (8, 16, 24, and 32) and different aspect ratios (2 to 4) were tried and only the best settings were chosen for the four quadrature Gabor filter pairs. The number of sampling points was 256. As a result, the iris code took exactly 256 bytes for each iris image, which is the same length as in [26] [25]. The DoS filters with binarization also resulted in a binary feature vector of 256 bytes. Computationally, DoS

filtering is much faster than Gabor filtering because of its simplicity and the use of the integral image. We do not report the specific computation times here because the code for both DoS filtering and Gabor filtering are not optimized in our implementations. Instead, an analysis of the computation is given in Section 4.5.2. For iris matching, the Hamming distance [26] was computed with 6 shifts (each shift is one byte) to the left and right to compensate for iris rotation.

4.5.3.2 FAR and FRR

The intra- and inter-class Hamming distance distributions for both methods are shown in Figure 4.21. The top corresponds to the iris code method, and the bottom to DoS filters. One can see that both methods for feature encoding deliver separated peaks for the intra- and inter-class distributions. To make a quantitative comparison, the false accept rate (FAR) and false reject rate (FRR) were computed with different separation points. As shown in Table 4.4, DoS filters have smaller error rates than the iris code consistently over the range of threshold values. To show the improvement of the DoS filters over the iris code method visually, the ROC curves are given in Figure 4.22 where the curve for the DoS filters is much lower than that for the iris code. This suggests that DoS filtering gives smaller error rates than the iris code with various separation points. These comparisons indicate that iris features encoded by the DoS filters are more discriminative than the iris code method, and thus give higher recognition accuracy. For both methods, a good choice of the threshold value is 0.4 for intra- and inter-class separation, where both our method and the iris code have 0 FRR. Our method does have a smaller FAR of 0.0036 than the iris code FAR value of 0.0039. The threshold value of 0.4 is the same as that suggested by Masek [84] in his Matlab implementation of the iris code [17].

4.5.3.3 Decidability

For a two-choice decision, Daugman [25] introduced the "decidability" index d to measure how well separated the two distributions are. For two distributions with means μ_1 and μ_2, and standard

deviations σ_1 and σ_2, the decidability index d is defined as

$$d = \frac{|\mu_1 - \mu_2|}{\sqrt{(\sigma_1^2 + \sigma_2^2)/2}} \qquad [4.17]$$

Since recognition errors are usually caused by the overlap between these two distributions, decidability measures how much the overlap is, and is independent of how the threshold is chosen to separate the two distributions. As shown in Table 4.4, the new features using DoS filters has decidability index 5.3 which is higher than the 4.7 using the iris code. This comparison also indicates that DoS filters have better performance for iris encoding than the iris code.

4.5.4 Discussion

In Daugman's iris code, the phase information is quantized after Gabor filtering to obtain a binary bit stream. In DoS filters there is no explicit phase information. The difference between the summations over different iris regions may be positive or negative given the randomness of iris texture. Thus a sign function is used to extract binary features for encoding.

For better iris matching, a mask image may be needed [25] to remove artifacts such as eyelid occlusions. But that is a hard problem in practice. In our approach, the bottom 2 rows (see Figure 4.20) were discarded during iris encoding to remove possible eyelid occlusions to some extent, similar to the approach in [76]. With this simple strategy, the error rates for the iris code and DoS filtering are very small after more than 200,000 comparisons. The FAR can be further reduced for both methods with the mask computation, and the decidability index can be increased too. But this does not affect our comparison of the two methods without computing the masks.

Difference-of-sum (DoS) filters are similar to the rectangle filters used by Viola and Jones for face detection [122]. We chose a different name here to emphasize (1) the computation instead of the filter shape, (2) the special design for iris feature encoding instead of searching all possible filters [122], and (3) more general realization of the filters with arbitrary dimensionality (1D, 2D, or higher for other kinds of data). It may be interesting to investigate 1D DoS filters (see Figure 4.17) with scaling for iris encoding, similar to Masek's approach of 1D log-Gabor filtering [84].

4.5.5 Summary

We presented a new method for iris feature encoding using difference-of-sum (DoS) filters. A special design of the DoS filter bank was proposed to characterize the iris pattern at multiple scales. One of the nice properties of DoS filters is that filtering can take advantage of the integral image representation, and thus all filtering takes a constant time no matter how big the filters are. DoS filters are conceptually simple and computationally fast. Experimental results demonstrated that DoS filters also give higher recognition accuracy than Daugman's iris code method.

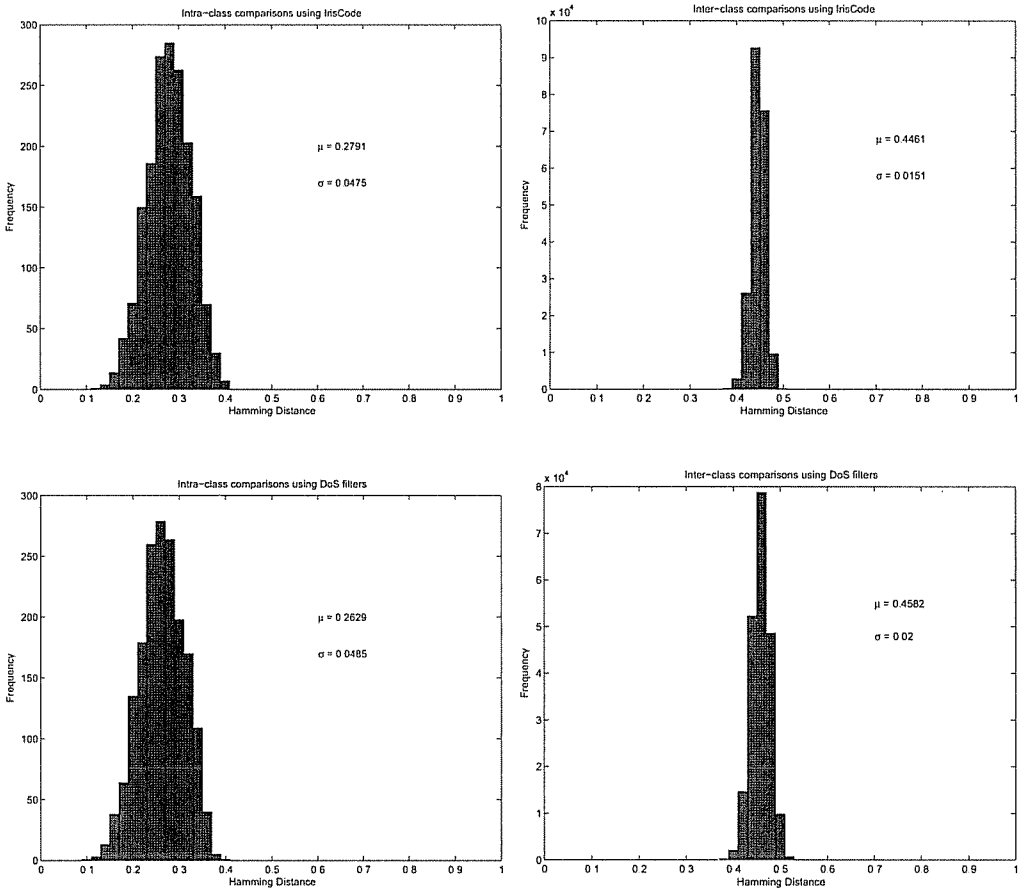

Figure 4.21 Intra- and inter-class Hamming distance distributions. Top: iris code, bottom: DoS filters.

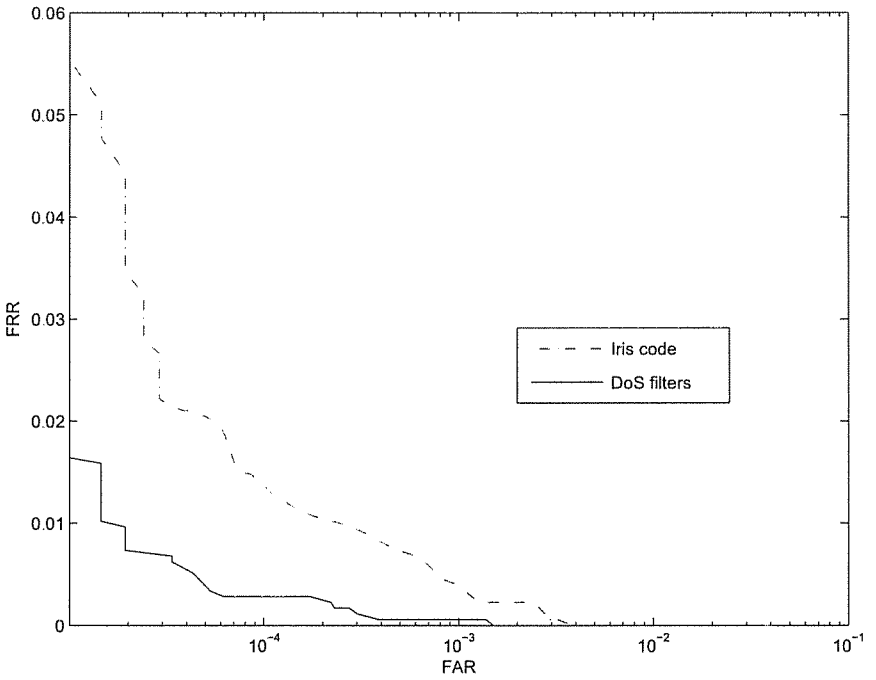

Figure 4.22 ROC curves showing the performance of DoS filters and iris code in terms of the FAR and FRR. The DoS filters give smaller error rates than the iris code method consistently at various separation points.

Chapter 5

Spatial Resolution Enhancement of Video Using Still Images

In this chapter we describe an extension of the two camera system for automatic iris capturing, i.e., combining images from digital still cameras and video cameras, to generate a video sequence with higher resolution than the original video.

The two-camera design for automatic iris acquisition takes advantage of both cameras: the video camera can capture both spatial and temporal information, identifying where the object is at each time, but its spatial resolution is low. On the other hand, the digital still camera has high spatial resolution, but cannot capture extended temporal information. We now consider the question: can the information from the video camera and still camera be combined to capture image data with high resolution in both space and time. Towards this goal, we have developed a method for increasing the spatial resolution from a video camera for a planar scene [45] where a homography can be computed based on detecting and matching of scale-invariant feature points [73].

5.1 Motivation

Visual information includes the dimensions of space, time, spectrum, and brightness [87]. However, a camera cannot capture all this information simultaneously. As a result, there are always trade-offs between the dimensions. For example, color cameras trade-off spatial resolution [87]. Among the multiple dimensions of images we are interested in the space-time interaction.

Digital still cameras capture the world at 5-10 times the spatial resolution of digital video cameras, while video cameras have denser temporal sampling. For example, the Kodak DCS-760

professional digital still camera has a resolution of 3032×2008 (6 megapixels), while the JVC JY-HD10U (high definition) digital video camera records frames of size 1280×720 (0.9 megapixels). For consumer products, 5 megapixel digital cameras (e.g. Canon Powershot G5) are common today, while most digital camcorders have 640×480 resolution (0.4 megapixels).

Why do digital still cameras and camcorders have such different spatial resolutions? One reason is the physical restriction. Charge-coupled devices (CCDs) are the most common image sensors used in digital cameras [23]. CCDs capture light in small photosites on their surface and the charge is read after an exposure. For example, charges on the last row are transferred to a read-out register. From there, the signals are fed to an amplifier and then to an analog-to-digital converter. Once the row has been read, its charges in the read-out register row are deleted, the next row enters the read-out register, and all of the rows above march down one row. The charges on each row are "coupled" to those on the row above so when one moves down, the next moves down to fill its old space. In this way, each row can be read, one row at a time. In digital video cameras, to capture 25 or more frames per second, there are a large quantity of charges to transfer per second. In order to keep the temporal sampling rate, the number of charges used for each frame has to be small enough. This is a space-time tradeoff.

One way to break through this physical restriction is to use multiple cameras such as both digital still cameras and digital camcorders. Then combine the information from both kinds of cameras to enrich each other. In practice, one may not need two or more cameras in order to reach this goal. Nowadays, many digital still cameras can capture short video segments and many digital camcorders can capture digital stills. Because of this property, one can use, for example, a single digital camera to capture high quality digital stills and low-resolution video sequences. However, still cameras can only capture short temporal sequences and video cameras cannot capture very high resolution still images. So, even these "combined cameras" do not adequately solve this space-time tradeoff.

Here we consider the goal of combining the best qualities of each type of camera. Specifically, using high resolution still images to enhance the spatial resolution of a video sequence. The framework of the approach is shown in Figure 5.1. This problem is related to, but different from,

existing super-resolution work that is based on signal reconstruction or example-based learning. In reconstruction-based super-resolution [58] [33] [137] [118] [15], multiple low-resolution images are registered to create a higher resolution image. See a review of approaches to super-resolution image reconstruction in [8]. In learning methods [40] [2], images and their size-reduced images are used as training pairs to learn high frequency information. Other recent work [105] aligns video sequences to increase resolution by assuming the video cameras have the same optical center.

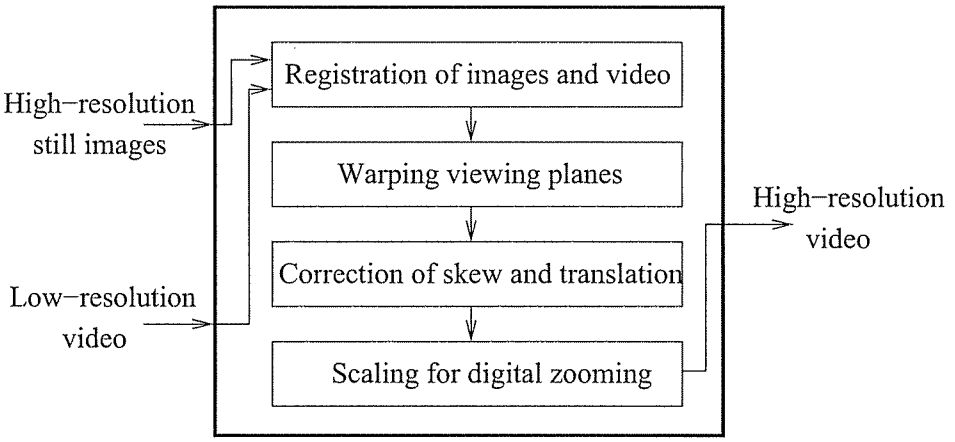

Figure 5.1 The framework of our approach.

We present a recognition-based scheme to align high-resolution images with video sequences in Section 5.2, and robustly estimate the mapping between the images and videos in Section 5.3. Then we describe a factorization technique to rotate and correct the high-resolution images in Sections 5.4 and 5.5. Experimental results are shown in Section 5.6 and further issues are discussed in Section 5.7.

5.2 Image and Video Alignment via Recognition

In order to use high-resolution still images to enhance low-resolution video frames, one has to first establish the relationship between them. That is, align or register the images coming from different sources.

Video registration is a challenging problem [114]. Because of camera motion, the viewpoints of a video sequence may change continuously and be different from the digital still images' viewpoints. Furthermore, the illumination and camera automatic gain may also change. However, the biggest variation in our problem is the difference in spatial resolution.

If two images to be matched have very different spatial resolutions in addition to viewpoint and illumination changes, traditional direct methods using optical flow or local feature (e.g. corner) matching cannot be used because these features are used under the assumption that local image patches between two images do not change significantly in appearance. These features especially lack invariance to scale [72]. For example, corner features are usually computed using the same template size for two images to be matched. When two images have very different scales, the computed values will be different in the two images. In order to align still images with video sequences, we have to find some new matching techniques.

One possible way to deal with image matching with very different scales is to formulate it as a one-to-many matching problem [31]. The high-resolution image is size-reduced by various scales and some local features are extracted at each scale. Another way is to extract scale-invariant features. Lowe [72] proposed a scale-invariant feature transform (SIFT) operator and used it successfully for object recognition. Using the SIFT operator, scale information is automatically encoded at each extracted key point, and there is no need to extract features at various scales of the image. Here, we use SIFT feature matching as the first step for our super-resolution method, and show that the SIFT operator can deal with large resolution differences.

The SIFT operator identifies key locations in scale space by looking for locations that are maxima or minima of a difference-of-Gaussian function. Each point is used to generate a feature vector that describes the local image region sampled relative to its scale-space coordinate frame. The features achieve partial invariance to local variations by blurring image gradient locations. The resulting feature vectors are called SIFT keys. A nearest neighbor criterion is then used to find similar keys in both images. For more details on the SIFT operator, see [72].

5.3 Homography Estimation

After using the SIFT operator for feature extraction and the nearest-neighbor criterion for feature matching, there are usually a large number of incorrect feature correspondences. Robust methods such as RANSAC [37] [55] can be used to remove outlier matches and estimate the homography between the two images.

There are three cases in which a planar homography is appropriate [15] [55]: (1) images of a planar scene viewed under arbitrary camera motion, (2) images of an arbitrary 3D scene viewed by a camera rotating about its optical center and/or zooming, and (3) a freely moving camera viewing a very distant scene. To demonstrate our approach, in this paper we assume the scene is planar and so a planar homography is sufficient to describe the relation between a high-resolution image and a low-resolution image.

5.4 Making Image Planes Parallel

Assume $\mathbf{q} = H\mathbf{p}$, where $\mathbf{p} = (x, y, w)^T$ are the homogeneous coordinates of a point in the low-resolution image, and $\mathbf{q}$ is the corresponding point in the high-resolution image. H is a 3×3 matrix, mapping the low-resolution image to the high-resolution image. For super-resolution purposes, knowing only the mapping H is not enough. The goal is to obtain an image pattern in a high-resolution image with the same viewpoint and illumination as that in the low-resolution image, mimicking a virtual camera with only a spatial scale difference.

To accomplish this, the high-resolution image must first be rotated so that it is parallel to the low-resolution image, as shown in Figure 5.2 where the high-resolution image B is rotated into B' so that B' is parallel to the low-resolution image S. We use QR decomposition to estimate the required rotation.

5.4.1 QR Factorization

The 3×3 homography matrix H can be decomposed into two matrices via QR factorization,

$$H = R_1 U_1 \qquad [5.1]$$

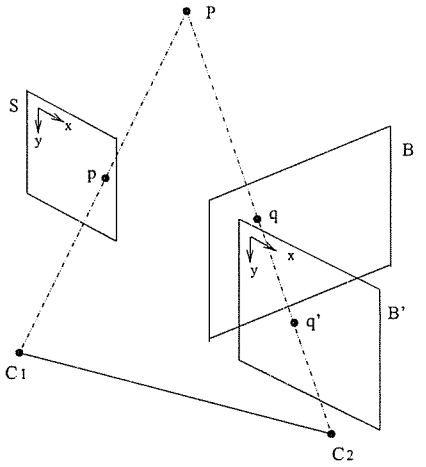

Figure 5.2 Two cameras (with centers $C1$ and $C2$ respectively) are used to capture the low-resolution image S and high-resolution image B which is rotated into B' so that the viewing plane B' is parallel to S. Note that this rotation is different from image rectification in stereo where both images are warped parallel to the baseline C_1C_2.

where R_1 is a rotation matrix and U_1 is an upper triangular matrix. Then, the inverse, H^{-1}, is defined as

$$H^{-1} = (R_1U_1)^{-1} = U_1^{-1}R_1^{-1} = U_2R_2 \qquad [5.2]$$

where $R_2 = R_1^{-1}$ is also a rotation matrix and $U_2 = U_1^{-1}$ is another upper triangular matrix.

From $\mathbf{p} = H^{-1}\mathbf{q}$ and Eq. (5.2), we get

$$\mathbf{p} = U_2R_2\mathbf{q} = U_2\mathbf{q}' \qquad [5.3]$$

where $\mathbf{q}' = R_2\mathbf{q}$ is the corresponding point in the rotated high-resolution image plane that is parallel to the low-resolution image frame. Point $\mathbf{p}$ in the low resolution image is mapped to point $\mathbf{q}'$ by

$$\mathbf{q}' = U_2^{-1}\mathbf{p} \qquad [5.4]$$

and U_2^{-1} has the form

$$U_2^{-1} = \begin{bmatrix} \alpha_x & s & t_x \\ 0 & \alpha_y & t_y \\ 0 & 0 & 1 \end{bmatrix} \quad [5.5]$$

where s is the skew, α_x, α_y are scale factors in the x and y directions respectively, and t_x and t_y are translations. In practice, the skew, s, may or may not be 0. If $s \neq 0$, we need to decompose U_2^{-1} further by

$$U_2^{-1} = \begin{bmatrix} \alpha_x & 0 & t_x \\ 0 & \alpha_y & t_y \\ 0 & 0 & 1 \end{bmatrix} \begin{bmatrix} 1 & \frac{s}{\alpha_x} & 0 \\ 0 & 1 & 0 \\ 0 & 0 & 1 \end{bmatrix} = T_{st} T_k \quad [5.6]$$

where T_k is the skew transform matrix, and T_{st} is the transform of scale and translation. For the purpose of analyzing resolution difference, it is better to further decompose T_{st} as

$$T_{st} = \begin{bmatrix} \alpha_x & 0 & 0 \\ 0 & \alpha_y & 0 \\ 0 & 0 & 1 \end{bmatrix} \begin{bmatrix} 1 & 0 & \frac{t_x}{\alpha_x} \\ 0 & 1 & \frac{t_y}{\alpha_y} \\ 0 & 0 & 1 \end{bmatrix} = T_s T_t \quad [5.7]$$

so we have $U_2^{-1} = T_s T_t T_k$. Letting $T_h = T_t T_k R_2$, one can apply T_h to the high resolution image by

$$\mathbf{q}'' = T_{tk}\mathbf{q}' = T_h \mathbf{q} \quad [5.8]$$

and apply T_s^{-1} to the low resolution image by

$$T_s^{-1}\mathbf{p} = \mathbf{q}'' \quad [5.9]$$

Eq. (5.8) warps the high-resolution image so that it is parallel to the low-resolution frame and has no skew or translation difference. The remaining difference between $\mathbf{q}''$ and $\mathbf{p}$ is just the scale factor, which is encoded in T_s. Eq. (5.9) is used to scale the low-resolution image and find the corresponding position in the rotated, skew-corrected, and translation-corrected high-resolution image for any point $\mathbf{p}$. Note that there is only a scale transformation, T_s^{-1}, between $\mathbf{p}$ and $\mathbf{q}''$. To summarize, all mappings are shown in Figure 5.3.

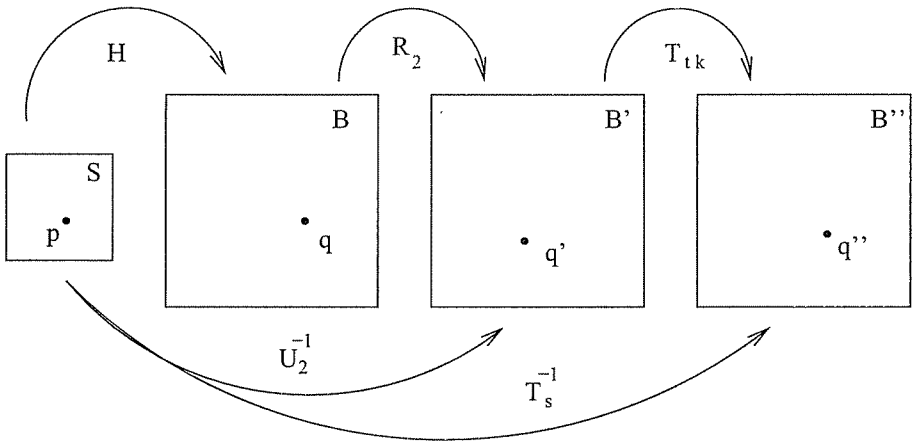

Figure 5.3 The relation between the low-resolution input image S, high-resolution input image B, rotated image B', and skew and translation corrected image B''. p, q, q′, and q″ are corresponding points in each image.

5.4.2 Scale Coherence in Two Directions

The pixels in the images may be square or non-square, as determined by the physical CCDs. The *pixel aspect ratio* (AR) is the ratio of horizontal and vertical sizes of a pixel. This term also refers to an image's display resolution. For instance, an image with a 640×480 resolution has an aspect ratio of 4:3, while a 720×480 resolution has an AR of 3:2. The standard aspect ratio for traditional television sets and computer monitors is 4:3 while the aspect ratio for high-definition, wide-screen digital systems is 16:9. In our super-resolution work, the high-resolution still images may have a different AR than the low-resolution video frames when two different cameras are used. Different ARs may result in different scale factors in the x and y directions, i.e., $\alpha_x \neq \alpha_y$ in Eqs. (5.5), (5.6), and (5.7). While the goal is to enhance the spatial resolution of each video frame, it is not a good idea to change the aspect ratio of the low-resolution frames after enhancement. To avoid this, the two scale factors, α_x and α_y, should be normalized to a common value, analogous to digitally zooming the low-resolution images by a given percentage. Assuming $\alpha_x > \alpha_y$, T_s can

be decomposed as

$$T_s = \begin{bmatrix} \alpha_x & 0 & 0 \\ 0 & \alpha_x & 0 \\ 0 & 0 & 1 \end{bmatrix} \begin{bmatrix} 1 & 0 & 0 \\ 0 & \frac{\alpha_y}{\alpha_x} & 0 \\ 0 & 0 & 1 \end{bmatrix} = T_{ss} T_{sc} \qquad [5.10]$$

Let $T_h' = T_{sc} T_t T_k R_2$ and apply it to the high-resolution image, and only apply T_{ss}^{-1} to the low-resolution images. The scale factor between the low-resolution and high-resolution images is equal to the first element of T_{ss}^{-1}, i.e., $T_{ss}^{-1}(1,1)$, assuming the last element, $T_{ss}^{-1}(3,3)$, equals 1.

In practice, even if the aspect ratios of the two cameras are the same, or only one digital camera is used to capture both the high-resolution still images and low-resolution videos, the estimated scale factors, α_x and α_y, may still be different because of the image and video registration accuracy, and possibly the manufacturing precision. So, the scale factors α_x and α_y should be normalized to a common value in all cases.

5.4.3 Non-Uniqueness

QR decomposition is not unique. Thus when we use the computed R to warp the high-resolution image, it may result in an "invalid" rotation (e.g., the rotated points have negative coordinates). To prove the non-uniqueness of QR decomposition, let $H = RU = (RD)(D^{-1}U) = R'U'$, given that D is orthogonal with determinant 1 and $D \neq I$. Since both R and D are orthonormal, RD is also orthonormal, and $D^{-1}U$ is upper triangular.

In practice, we can check if α_x and α_y (in Eq. (5.6)) are both negative. If so, we can choose

$$D = \begin{bmatrix} -1 & 0 & 0 \\ 0 & -1 & 0 \\ 0 & 0 & 1 \end{bmatrix} \qquad [5.11]$$

and use $H = R'U'$ instead of RU. Note that α_x and α_y cannot have different signs because we cannot capture an image with positive scale in one dimension and negative scale in the other.

5.5 Photometric Correction

Besides the geometrical differences between the low and high resolution images, there may also be differences in the intensities between the images because of global illumination variation and/or camera automatic gain differences. To cope with photometric variation, we use a simple linear method to align the intensities of the warped high resolution image with the low resolution image,

$$E_{new} = \frac{E - B''_{min}}{B''_{max} - B''_{min}}(S_{max} - S_{min}) + S_{min} \qquad [5.12]$$

where B''_{max} and B''_{min} are the maximum and minimum intensities in a region in the warped high-resolution image, S_{max} and S_{min} are the maximum and minimum intensities in the corresponding region in the low-resolution image, E is the given pixel's intensity in B'', and E_{new} is the photometrically-corrected value. Eq. (5.12) is applied for each pixel in each color channel separately.

The whole procedure presented in Sections 5.2 to 5.5 can be applied to each frame of the video sequence using each high-resolution still image.

5.6 Experiments

A Canon PowerShot A70 digital camera was used to capture both the high-resolution still images (of size 2048×1536) using the "auto mode," and the video sequences (each frame of size 320×240) with the "video mode." The scene is a rug containing many details. For display purposes only, the still images were reduced to 1280×960, which has no influence on demonstrating the basic idea.

In Figure 5.4 one image extracted from the video sequence is shown at the top-left, and one high-resolution image is shown in the middle. Using the SIFT operator for feature detection, 5,834 points were extracted from the high-resolution image, and 1,457 points from the low-resolution image. Using nearest neighbor matching, 471 correspondences were found. However, there are many outliers (i.e., mismatches) there. Using RANSAC to estimate the homography, 173 inliers were selected, from which only 30 are displayed in both images (top-right and middle in Figure

5.4) to avoid confusion in this visualization. The condition number of the 3×3 homography matrix H is large, but the estimate is accurate. We also used the normalization approach, but it did not improve the results significantly. QR factorization and related manipulations were performed, Eq. (5.8) was used to warp the high-resolution image parallel to the low-resolution image frame and to correct skew and translation. Eq. (5.9) was used to zoom in the low-resolution image. The scales were estimated using Eq. (5.10) and the scales in the x and y directions are the same without changing the aspect ratio of the low-resolution images. Photometric correction using Eq. (5.12) was then done. For the low-resolution image shown at the top-left in Figure 5.4, its enhanced high-resolution image (of size 1392×1044) is shown at the bottom. The estimated scale difference is 4.35, which is bigger than the image size difference (four times in each direction) between the input high-resolution image (1280×960, middle in Figure 5.4) and the low-resolution image (320×240).

To see the result clearly, it is better to look closely at some selected regions in the images. A 100×100 window was cropped from the low-resolution image (at the top-right in Figure 5.4) and shown in the top of Figure 5.5. The small patch was re-scaled using bilinear interpolation (middle left) and bicubic interpolation (middle right) as shown in Figure 5.5. Clearly, many details were lost and the image patch looks vague. Image interpolation does not add new information although the image size is bigger. The corresponding patch in the warped high resolution image is cropped and shown at the bottom-left in Figure 5.5, which is much clearer. The flowers in the middle and the stripes at bottom-left can be seen clearly. Finally, photometric correction using Eq. (5.12) was performed and the new image is shown at the bottom-right in Figure 5.5. From this experimental result we can see that the low-resolution image can be greatly enriched using the information from the input high-resolution image.

5.7 Discussion

We have demonstrated an approach for using high-resolution digital still images to enhance low-resolution video sequences. There are several questions remaining to be answered: 1) How many high-resolution images are needed? Currently, we use only one high-resolution image to

enhance the whole video sequence. Some regions in the low-resolution images cannot be "enhanced" because the corresponding parts do not exist in the high-resolution image. Hence more high-resolution images may be necessary. 2) How far apart can the viewpoints be when capturing the videos and high-resolution images? If they are too far apart, there will be distortions when warping the images. 3) How should the high-resolution images for a more general, non-planar, scene be warped? In our experiments, we assumed a 3×3 homography, which is not general enough to deal with all possible scenes. 4) How should photometric correction be done for more complex illumination conditions? We believe that all these problems deserve investigation based on the results here.

5.8 Summary

We have proposed enhancing the spatial resolution of video sequences using higher resolution digital still images. A recognition-based method using invariant features was presented to register the high-resolution images with the low-resolution video sequences. A simple, robust method based on QR factorization was used to warp the high-resolution images in order to mimic a digital "zooming" effect. The procedure realizes the basic idea of our still-image-based video enhancement framework. Many extensions of the method are possible in order to build a real system for practical use.

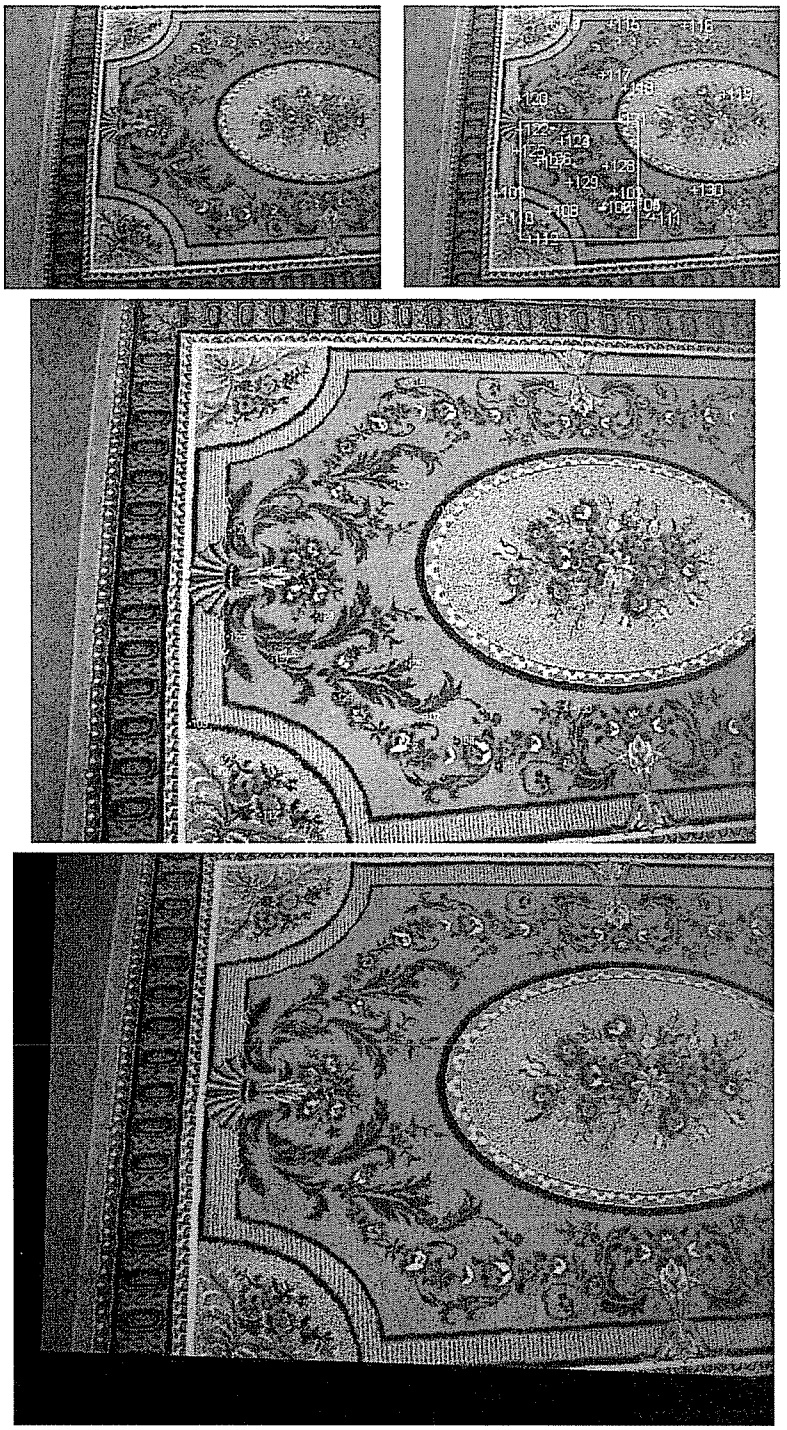

Figure 5.4 Top Left: One frame from a video sequence with frame size 320×240; Top right: a few features detected by the SIFT operator; Middle: A high resolution still image of size 1280×960. Bottom: The resolution-enhanced image of size 1392×1044.

Figure 5.5 Top row: The image block of size 100 × 100 cropped from the square shown in the top right image of Figure 5.4; Middle-left: Cropped square enlarged using bilinear interpolation with the estimated scale 4.35; Middle-right: Enlarged using bicubic interpolation; Bottom-left: Corresponding high resolution block extracted and warped from the bottom image in Figure 5.4; Bottom-right: Photometrically corrected image of the bottom-left image.

Chapter 6

Conclusions

This thesis investigated some problems of facial image analysis, targeting face recognition, face expression recognition, and iris recognition. Learning-based methods are used to attack these computer vision problems.

6.1 Contributions

The major contributions of this dissertation are:

- A face cyclograph representation was developed for encoding continuous views of faces. The face cyclograph is compact and multiperspective. For recognition using the face cyclograph representation, a method was presented based on dynamic programming. Experimental evaluations on a face video database with 102 videos showed that the recognition accuracy was 99.01%. We also developed a method for normalizing face cyclographs with slightly lower recognition accuracy.

- A linear programming technique was used for face expression recognition. The advantage of this method is that a small number of features, e.g., less than 20 versus the original 612 features, can be selected simultaneously with classifier training, even in the small sample case. The recognition accuracy was as high as 91% on a public face expression database.

- A two-camera system was designed and implemented for automatic iris capture. A "face camera" with wide field of view is used to control a narrow field of view "iris camera" for automatic iris acquisition. The system can track users' eye positions, maintaining the eyes

in the center of the iris cameras' image. A prototype system was built and evaluated on capturing about 20 people's eyes without failure.

- A novel method was presented for iris localization. By including features describing the texture difference between the iris and sclera and between the iris and pupil, in addition to image gradient features, the performance of iris localization was improved significantly. For example, our method extracted iris boundaries precisely for 97.6% of the eye images in the CASIA database, in contrast to 85.6% for Wildes' and 88% for Daugman's methods.

- A new method was proposed for iris encoding. A set of filters, called difference-of-sum filters, was designed for iris feature extraction. These filters can take advantage of a pre-computed integral image, which makes the filtering process take constant computation time no matter how big the filters are. Experimental evaluation shows that the new method has higher recognition accuracy and is faster than Daugman's iris code method. The false acceptance rate was reduced by 7% in comparison with the iris code method.

6.2 Limitations and Future Work

The face cyclograph representation is obtained when a person's head rotates in front of a stationary video camera. Our focus was to develop a concise representation of faces given such face image sequences. In order to extend the face cyclograph representation to face videos containing arbitrary head motions, a pre-processing step is required. That is, manipulate a face video with arbitrary head motion to synthesize a face video corresponding to single-axis head rotation starting and ending at designated poses. This pre-processing step can be viewed as an image-based rendering problem [108]. Then, a face cyclograph can be generated and used for recognition based on the techniques presented in this thesis. We will investigate this issue in the future.

The two-camera system for automatic iris acquisition has been evaluated successfully for a small number of people. The key idea is to use learning methods and computer vision techniques to design an automatic system replacing human adjustments of eye positions. In order to make a real product, more evaluation work has to be done for more people. Furthermore, we have not

considered use of infrared illumination in the current system. For black eyes, infrared light is necessary in order to capture rich iris texture.

The methods for iris localization and encoding were evaluated using the CASIA database [17] which was the only publicly available iris database available at the time. Recently, NIST has created a new iris database called ICE [89]. We may evaluate our methods using the ICE database in the future.

Learning for vision is a promising research direction. A wide variety of computer vision problems can benefit from learning techniques, not just object recognition problems. We have applied support vector regression (SVR) [121] for outlier detection and removal in affine motion tracking [48]. The problem is to detect and remove outliers in feature point trajectories given by a tracking method such as the KLT tracker [106]. Clean feature trajectories are of great importance for computer vision problems such as video sequence alignment, structure from motion, and motion segmentation. The key idea of our approach [48] is to develop a linear combination representation to characterize the relation of four image frames or four feature trajectories, and then the SVR method can be applied directly to estimate the linear combination coefficients and remove the outliers. Experimental results show that the SVR technique works slightly better than the RANdom SAmple Concensus (RANSAC) method [37] which is used widely in computer vision [39]. One experimental result is shown in Figure 6.1. Our future research will investigate new learning techniques for a wider range of computer vision problems.

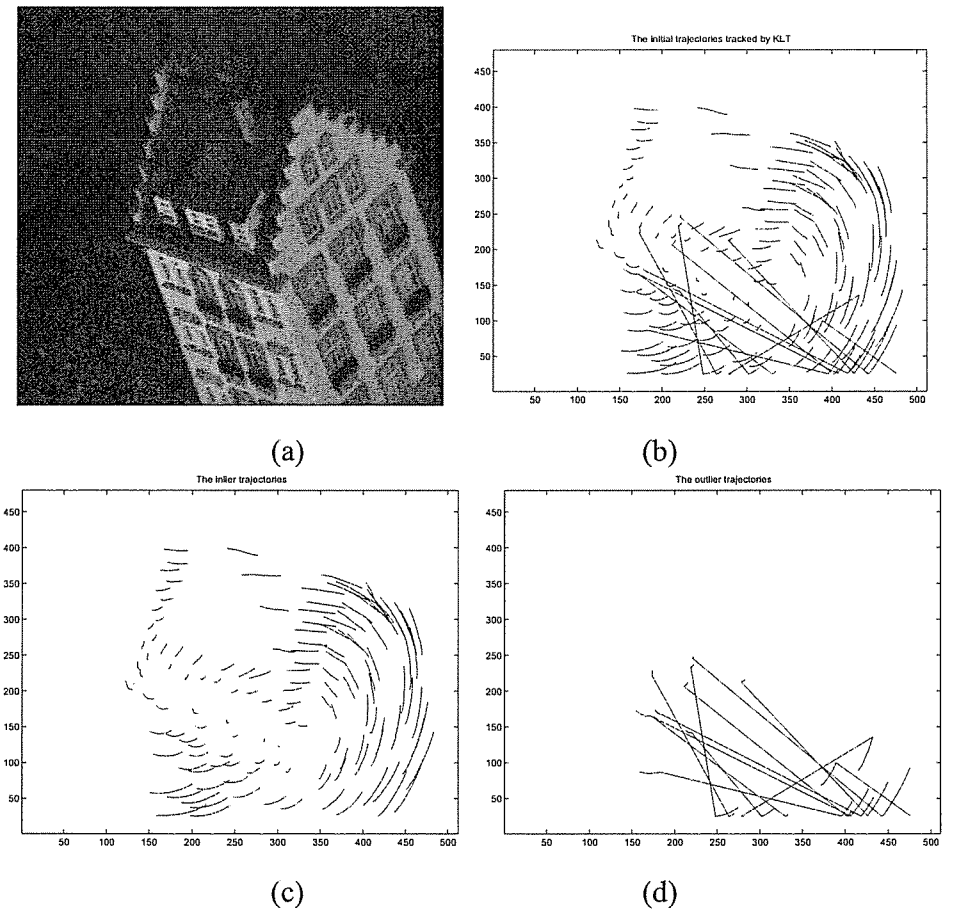

Figure 6.1 The first frame (a) and the KLT tracked trajectories (b) of the hotel sequence. Inliers (c) and outliers (d) computed by our trajectory-based linear combination and SVR method.

LIST OF REFERENCES

[1] G. Aggarwal, A. R. Chowdhury, and R. Chellappa. A system identification approach for video-based face recognition. In *Proc. 17th Int. Conf. Pattern Recognition*, volume 1, pages 175–178, 2004.

[2] S. Baker and T. Kanade. Limits on super-resolution and how to break them. In *IEEE Trans. Pattern Analysis and Machine Intell.*, volume 24, pages 1167–1183, 2002.

[3] M. Bartlett, P. Viola, T. Sejnowski, L. Larsen, J. Hager, and P. Ekman. Classifying facial action. In D. Touretzky, D. Touretzky, M. Mozer, and M.Hasselmo, editors, *Advances in Neural Information Processing Systems 8*, pages 823–829. MIT Press, Cambridge, Mass., 1996.

[4] P. Belhumeur, J. Hespanha, and D. Kriegman. Eigenfaces vs. fisherfaces: Recognition using class specific linear projection. *IEEE Trans. Pattern Analysis and Machine Intell.*, 19(7):711–720, 1997.

[5] K. P. Bennett and O. L. Mangasarian. Robust linear programming discrimination of two linearly inseparable sets. *Optimization Methods and Software*, 1:23–34, 1992.

[6] W. Boles and B. Boashash. A human identification technique using images of the iris and wavelet transform. *IEEE Trans. Signal Processing*, 46(4):1185–1188, 1998.

[7] R. C. Bolles, H. H. Baker, and D. H. Marimont. Epipolar-plane image analysis: An approach to determining structure from motion. *Int. J. Computer Vision*, 1(1):7–55, 1987.

[8] S. Borman and R. L. Stevenson. Super-Resolution from Image Sequences - A Review. In *Proc. the 1998 Midwest Symposium on Circuits and Systems*, 1998.

[9] P. S. Bradley and O. L. Mangasarian. Feature selection via concave minimization and support vector machines. In *Proc. 5th Int. Conf. Machine Learning*, pages 82–90, 1998.

[10] J. Brank, M. Grobelnik, N. M. Frayling, and D. Mladenic. Feature selection using linear support vector machines. Technical Report Technical Report MSR-TR-2002-63, Microsoft, 2002.

[11] M. Brown, D. Burschka, and G. Hager. Advances in computational stereo. *IEEE Trans. Pattern Analysis and Machine Intelligence*, 25(8):993–1008, 2003.

[12] H. H. Bülthoff, C. Wallraven, and A. Graf. View-based dynamic object recognition based on human perception. *Proc. 16th Int. Conf. Pattern Recognition*, 3:768–776, 2002.

[13] T. Camus and R. Wildes. Reliable and fast eye finding in close-up images. In *Proc.* 16^{th} *Int. Conf. on Pattern Recognition*, pages 389–394, 2002.

[14] J. Canny. A computational approach to edge detection. *IEEE Trans. Pattern Analysis and Machine Intelligence*, 8:679–698, 1986.

[15] D. Capel and A. Zisserman. Computer vision applied to super resolution. In *IEEE Signal Processing Magazine*, pages 75–86, 2003.

[16] M. Cascia, S. Sclaroff, and V. Athitsos. Fast, reliable head tracking under varying illumination: An approach based on registration of texture-mapped 3d models. *IEEE Trans. Pattern Analysis and Machine Intell.*, 22(4):322–336, 2000.

[17] CASIA. Iris image database, 2004. http://www.sinobiometrics.com.

[18] R. Chellappa, C. L. Wilson, and S. Sirohey. Human and machine recognition of faces: A survey. *Proc. IEEE*, 83:705–741, May 1995.

[19] G. Cottrell and J. Metcalfe. Face, gender and emotion recognition using holons. In *Advances in Neural Information Processing Systems*, volume 3, pages 564–571, 1991.

[20] T. M. Cover and J. A. Thomas. *Elements of Information Theory*. Wiley, 1991.

[21] F. Crow. Summed-area tables for texture mapping. In *Proc. SIGGRAPH 84*, volume 18, pages 207–212, 1984.

[22] J. Cui, Y. Wang, T. Tan, L. Ma, and Z. Sun. A fast and robust iris localization method based on texture segmentation. In *Proc. SPIE on Biometric Technology for Human Identification*, volume 5404, pages 401–408, 2004.

[23] D. P. Curtin. *The Textbook of Digital Photography*. http://www.shortcourses.com/, 2003.

[24] J. Daugman. Uncertainty relation for resolution in space, spatial frequency, and orientation optimized by 2d visual cortical filters. *J. Opt. Soc. Am. A*, 2(7):1160–1169, 1985.

[25] J. Daugman. How iris recognition works. *IEEE Trans. Circuits and Systems for Video Technology*, 14:21–30, 2004.

[26] J. G. Daugman. High confidence visual recognition of persons by a test of statistical indenpendence. *IEEE Trans. Pattern Analysis and Machine Intelligence*, 15:1148–1161, 1993.

[27] A. Davidhazy. Peripheral photography: Shooting full circle. *Industrial Photography*, 36(1):28–31, 1987.

[28] D. Decarlo, D. Metaxas, and M. Stone. An anthropometric face model using variational techniques. In *Proc. SIGGRAPH 98*, pages 67–74, 1998.

[29] P. A. Devijver and J. Kittler. *Pattern Recognition: A Statistical Approach*. Prentice Hall, Englewood Cliffs, N.J., 1982.

[30] G. Donato, M. S. Bartlett, J. C. Hager, P. Ekman, and T. J. Sejnowski. Classifying facial actions. *IEEE Trans. Pattern Analysis and Machine Intelligence*, 21(10):974–989, 1999.

[31] Y. Dufournaud, C. Schmid, and R. Horaud. Matching images with different resolutions. In *Proc. Computer Vision and Pattern Recognition*, pages 612–618, 2000.

[32] R. P. W. Duin. Classifiers in almost empty spaces. In *Proc. 15^{th} Int. Conf. Pattern Recognition*, volume 2, pages 1–7, 2000.

[33] M. Elad and A. Feuer. Super-resolution reconstruction of image sequences. In *IEEE Trans. Pattern Analysis and Machine Intelligence*, volume 21, pages 817–834, 1999.

[34] I. Essa and A. Pentland. Coding, analysis, interpretation, and recognition of facial expressions. *IEEE Trans. Pattern Analysis and Machine Intelligence*, 19(7):757–763, 1997.

[35] L. Farkas. *Anthropometry of the Head and Face*. Raven Press, New York, 1994.

[36] B. Fasel and J. Luettin. Automatic facial expression analysis: A survey. *Pattern Recognition*, 36(1):259–275, 2003.

[37] M. A. Fischler and R. C. Bolles. Random sample consensus: A paradigm for model fitting with applications to image analysis and automated cartography. *Comm. of the ACM*, 24(6):381–395, 1981.

[38] A. Fitzgibbon, M. Pilu, and R. Fisher. Direct least-square fitting of ellipses. *IEEE Trans. Pattern Analysis and Machine Intelligence*, 21:476–480, 1999.

[39] D. A. Forsyth and J. Ponce. *Computer Vision: A Modern Approach*. Prentice Hall, Upper Saddle River, N. J., 2003.

[40] W. T. Freeman, E. C. Pasztor, and O. T. Carmichael. Learning low-level vision. In *Int. J. Computer Vision*, volume 40, pages 25–47, 2000.

[41] Y. Freund and R. E. Schapire. A decision-theoretic generalization of online learning and an application to boosting. *J. Comp. & Sys. Sci.*, 55(1):119–139, 1997.

[42] Yoav Freund and Robert E. Schapire. A decision-theoretic generalization of on-line learning and an application to boosting. In *Computational Learning Theory: Eurocolt '95*, pages 23–37. Springer-Verlag, 1995.

[43] R. C. Gonzalez and P. Wintz. *Digital Image Processing*. Addison-Wesley, Reading, Mass., 1987.

[44] G-D. Guo and C. R. Dyer. Simultaneous feature selection and classifier training via linear programming: A case study for face expression recognition. In *Proc. Computer Vision and Pattern Recognition*, volume 1, pages 346–352, 2003.

[45] G-D. Guo and C. R. Dyer. Spatial resolution enhancement of video using still images. Technical Report TR-1502, University of Wisconsin - Madison, April 2004.

[46] G-D. Guo and C. R. Dyer. Learning from examples in the small sample case: Face expression recognition. *IEEE Trans. System, Man and Cybernetics - Part B*, 35(3):477–488, 2005.

[47] G-D. Guo and C. R. Dyer. Face cyclographs for recognition. Technical Report TR-1555, University of Wisconsin - Madison, March 2006.

[48] G-D. Guo, C. R. Dyer, and Z. Zhang. Linear combination representation for outlier detection in motion tracking. In *Proc. Computer Vision and Pattern Recognition*, volume 2, pages 274–281, 2005.

[49] G-D. Guo and M. Jones. Difference of sum filters for texture classification, January 2006. US Patent filed.

[50] G-D. Guo and M. Jones. Method for extracting features of irises in images using difference of sum filters, January 2006. US Patent filed.

[51] G-D. Guo and M. Jones. Method for localizing irises in images using gradients and textures, January 2006. US Patent filed.

[52] G-D. Guo, M. Jones, and P. Beardsley. A system for automatic iris capturing. Technical Report TR2005-044, Mitsubishi Electric Research Labs, June 2005.

[53] G-D. Guo, S. Z. Li, and K. L. Chan. Face recognition by support vector machines. *Proc. 4th Int. Conf. Automatic Face and Gesture Recognition*, pages 196–201, 2000.

[54] A. Hadid and M. Pietikinen. An experimental investigation about the integration of facial dynamics in video-based face recognition. *Electronic Letters on Computer Vision and Image Analysis*, 5(1):1–13, 2005.

[55] R. I. Hartley and A. Zisserman. *Multiple View Geometry in Computer Vision*. Cambridge University Press, 2000.

[56] B. Heisele, P. Ho, and T. Poggio. Face recognition with support vector machines: global versus component-based approach. In *Proc. Int. Conf. Computer Vision*, volume 2, pages 688–694, 2001.

[57] P. V. C. Hough. Method and means for recognizing complex patterns. *U.S. Patent 3 069 654*, 1962.

[58] M. Irani and S. Peleg. Improving resolution by image registration. In *Graphical Models and Image Processing*, volume 53, pages 231–139, 1991.

[59] A. Jain and D. Zongker. Feature selection: Evaluation, application, and small sample performance. *IEEE Trans. Pattern Analysis and Machine Intell.*, 19(2):153–158, 1997.

[60] A. K. Jain and F. Farrokhnia. Unsupervised texture segmentation using gabor filters. *Pattern Recognition*, 16(12):1167–1186, 1991.

[61] A. K. Jain, A. Ross, and S. Prabhakar. An introduction to biometric recognition. *IEEE Trans. Circuits and Systems for Video Technology*, 14:4–20, 2004.

[62] J. Kim, S. Cho, and J. Choi. Iris recognition using wavelet features. *J. VLSI Signal Processing*, 38:147–156, 2004.

[63] A. W. Kong and D. Zhang. Detecting eyelash and reflection for accurate iris segmentation. *Int. J. Pattern Recognition and Artifical Intelligence*, 17(6):1025–1034, 2003.

[64] M. Lades, J. C. Vorbruggen, J. Buhmann, J. Lange, C. von der Malsburg, R. P. Wurtz, and W. Konen. Distortion invariant object recognition in the dynamic link architecture. *IEEE Trans. Computers*, 42(3):300–311, 1993.

[65] A. Lanitis, C. Taylor, and T. Cootes. Automatic interpretation and coding of face images using flexible models. *IEEE Trans. Pattern Analysis and Machine Intell.*, 19(7):743–756, 1997.

[66] K. C. Lee, J. Ho, M. H. Yang, and D. Kriegman. Video-based face recognition using probabilistic appearance manifolds. In *Proc. Computer Vision and Pattern Recognition*, pages 313–320, 2003.

[67] B. Li and R. Chellappa. Face verification through tracking facial features. *J. Opt. Soc. Am.*, 18:2969–2981, 2001.

[68] S. Lim, K. Lee, O. Byeon, and T. kim. Efficient iris recognition through improvement of feature vector and classifier. *Elec. Tele. Res. Institute J.*, 23(2):61–70, 2001.

[69] C. Liu and H. Wechsler. Probabilistic reasoning models for face recognition. *Proc. Computer Vision and Pattern Recognition*, pages 827–832, 1998.

[70] X. Liu and T. Chen. Video-based face recognition using adaptive hidden markov models. In *Proc. Computer Vision and Pattern Recognition*, pages 340–345, 2003.

[71] X. Liu and T. Chen. Pose-robust face recognition using geometry assisted probabilistic modeling. In *Proc. Computer Vision and Pattern Recognition*, pages 502–509, 2005.

[72] D. G. Lowe. Object recognition from local scale-invariant features. In *Proc. Int. Conf. Computer Vision*, pages 1150–1157, 1999.

[73] D. G. Lowe. Distinctive image features from scale-invariant keypoints. *Int. J. Computer Vision*, 60(2):91–110, 2004.

[74] M. J. Lyons, S. Akamatsu, M. Kamachi, and J. Gyoba. Coding facial expressions with gabor wavelets. In *Proc. 3rd Int. Conf. Automatic Face and Gesture Recognition*, pages 200–205, 1998.

[75] M. J. Lyons, J. Budynek, and S. Akamatsu. Automatic classification of single facial images. *IEEE Trans. Pattern Analysis and Machine Intelligence*, 21(12):1357–1362, 1999.

[76] L. Ma, T. Tan, Y. Wang, and D. Zhang. Personal identification based on iris texture analysis. *IEEE Trans. Pattern Analysis and Machine Intelligence*, 25:1519–1533, 2003.

[77] L. Ma, T. Tan, Y. Wang, and D. Zhang. Efficient iris recognition by characterizing key local variations. *IEEE Trans. Image Processing*, 13(6):739–750, 2004.

[78] T. Maenpaa and M. Pietikainen. Texture analysis with local binary patterns. In C. Chen and P. Wang, editors, *Handbook of Pattern Recognition and Computer Vision*, 3rd ed., pages 197–216. World Scientific, 2005.

[79] O. L. Mangasarian. Linear and nonlinear separation of patterns by linear programming. *Operations Research*, 13:444–452, 1965.

[80] B. S. Manjunath and W. Y. Ma. Texture features for browsing and retrieval of image data. *IEEE Trans. Pattern Analysis and Machine Intelligence*, 18(8):837–842, 1996.

[81] T. Mansfield, G. Kelly, D. Chandler, and J. Kane. Biometric product testing final report. *UK Biometric Work Group Report*, 2001.

[82] D. Marr. *Vision*. Freeman Publishers, San Francisco, Ca., 1982.

[83] K. Mase. Recognition of facial expression from optical flow. *IEICE Trans. E*, 74(10):3473–3483, 1991.

[84] L. Masek and P. Kovesi. *MATLAB Source Code for a Biometric Identification System Based on Iris Patterns*. The School of Computer Science and Software Engineering, The University of Western Australia, 2003.

[85] Y. Miyashita. Neural correlate of visual associative long-term memory in the primate temporal cortex. *Nature*, 335:817–820, 1988.

[86] B. Moghaddam, T. Jebara, and A. Pentland. Bayesian face recognition. *Pattern Recognition*, 33(11):1771–1782, 2000.

[87] S. K. Nayar and S. G. Narasimhan. Assorted pixels: Multi-sampled imaging with structural models. In *Proc. Europe Conf. Computer Vision*, volume 3, pages 148–162, 2002.

[88] M. Negin, T. Chmielewski, M. Salganicoff, U. von Seelen, P. Venetainer, and G. Zhang. An iris biometric system for public and personal use. In *IEEE Computer*, volume 33, pages 70–75, 2000.

[89] NIST. Iris challenge evaluation (ice), 2006. http://iris.nist.gov/ICE/.

[90] T. Ojala, M. Pietikäinen, and D. Harwood. A comparative study of texture measures with classification based on feature distributions. *Pattern Recognition*, 29:51–59, 1996.

[91] C. Padgett and G. Cottrell. Identifying emotion in static images. In *Proc. 2nd Joint Symp. on Neural Computation*, volume 5, pages 130–136, 1997.

[92] M. Pantie and L. J. M. Rothkrantz. Automatic analysis of facial expressions: The state of the art. *IEEE Trans. Pattern Analysis and Machine Intelligence*, 22(12):1424–1445, 2000.

[93] S. Peleg and J. Herman. Panoramic mosaics by manifold projection. In *Proc. Computer Vision and Pattern Recognition Conf.*, pages 338–343, 1997.

[94] H. Proenca and L. Alexandre. Ubiris: A noisy iris image database. In *Int. Conf. Image Analysis and Processing*, 2005.

[95] P. Pudil, J. Novovicova, and J. Kittler. Floating search methods in feature selection. *Pattern Recognition Letters*, 15(11):1119–1125, 1994.

[96] L. Rabiner and B. H. Juang. *Fundamentals of Speech Recognition*. Prentice Hall, Englewood Cliffs, 1993.

[97] A. Rad, R. Safabakhsh, N. Qaragozlou, and M. Zaheri. Fast iris and pupil localization and eyhelid removal using gradient vector pairs and certainty factors. In *Proc. Irish Machine Vision and Image Processing Conf.*, pages 82–91, 2004.

[98] P. Rademacher and G. Bishop. Multiple-center-of-projection images. In *Proc. SIGGRAPH 98*, pages 199–206, 1998.

[99] A. Rahardja, A. Sowmya, and W. Wilson. A neural network aproach to component versus holistic recognition of facial expressions in images. In *Proc. SPIE Intelligent Robots and Computer Vision X: Algorithms and Techniques*, volume 1607, pages 62–70, 1991.

[100] R. T. Rockafellar. *Convex Analysis*. Princeton University Press, Princeton, N. J., 1970.

[101] A. Samal and P. A. Iyengar. Automatic recognition and analysis of human faces and facial expressions: A survey. *Pattern Recognition*, 25:65–77, 1992.

[102] B. Scholkopf, A. Smola, and K.-R. Muller. Nonlinear component analysis as a kernel eigenvalue problem. *Neural Computation*, 10:1299–1319, 1998.

[103] S. M. Seitz and J. Kim. The space of all stereo images. *Int. J. Computer Vision*, 48:21–38, 2002.

[104] S. M. Seitz and J. Kim. Multiperspective imaging. *IEEE Computer Graphics and Applications*, 23:16–19, November/December 2003.

[105] E. Shechtman, Y. Caspi, and M. Irani. Increasing space-time resolution in video. In *Proc. Europe Conf. Computer Vision*, pages 753–768, 2002.

[106] J. Shi and C. Tomasi. Good features to track. *Proc. Computer Vision and Pattern Recognition*, pages 593–600, 1994.

[107] H. Y. Shum and L. W. He. Rendering with concentric mosaics. In *Proc. SIGGRAPH 99*, pages 299–306, 1999.

[108] H-Y. Shum and S. B. Kang. A review of image-based rendering techniques. In *IEEE/SPIE Visual Comm. and Image Processing*, pages 2–13, 2000.

[109] C. E. Springer. *Geometry and Analysis of Projective Spaces*. W. H. Freeman and Company, San Francisco, Ca., 1964.

[110] J. Stone. Object recognition using spatio-temporal signatures. *Vision Research*, 38(7):947–951, 1998.

[111] J. Stone. Object recognition: View-specificity and motion-specificity. *Vision Research*, 39(24):4032–4044, 1999.

[112] M. Suma, N. Sugie, and K. Jujimora. A preliminary note on pattern recognition of human emotional expression. In *Proc. 4th Int. Joint Conf. Pattern Recognition*, pages 408–410, 1978.

[113] Z. Sun, T. Tan, and Y. Wang. Robust encoding of local ordinal measures: A general framework of iris recognition. In *ECCV Workshop on Biometric Authentication*, 2004.

[114] R. Szeliski. Video registration: Key challenges. In M. Shah and R. Kumar, editors, *Video Registration*, pages 247–252, Boston, 2003. Kluwer Academic Publishers.

[115] M. J. Tarr and H. H. Bülthoff. *Object recognition in man, monkey, and machine*. Cambridge, MIT Press, 1999.

[116] Y.-L. Tian, T. Kanade, and J. F. Cohn. Recognizing action units for facial expression analysis. *IEEE Trans. Pattern Analysis and Machine Intelligence*, 23(2):97–115, 2001.

[117] K. Tieu and P. Viola. Boosting image retrieval. In *Proc. Computer Vision and Pattern Recognition*, volume I, pages 228–235, 2000.

[118] M. Tipping and C. Bishop. Bayesian image super-resolution. In S. Becker, S. Thrun, and K. Obermayer, editors, *Advances in Neural Information Processing Systems 15*, pages 1303–1310, 2003.

[119] M. A. Turk and A. P. Pentland. Eigenfaces for recognition. *J. Cognitive Neurosci.*, 3(1):71–86, 1991.

[120] A. Vailaya. *Semantic classification in image database*. Ph.D. thesis, Michigan State University, 2000.

[121] V. N. Vapnik. *Statistical Learning Theory*. Wiley, New York, 1998.

[122] P. Viola and M. Jones. Rapid object detection using a boosted cascade of simple features. In *Proc. Computer Vision and Pattern Recognition*, volume 1, pages 511–518, 2001.

[123] G. M. Wallis and H. H. Bülthoff. Effect of temporal association on recognition memory. In *Proc. Natl. Acad. Sci. USA*, volume 98, pages 4800–4804, 2001.

[124] J. Weston, S. Mukherjee, O. Chapelle, M. Pontil, T. Poggio, and V. Vapnik. Feature selection for svms. In *Advances in Neural Information Processing Systems*, volume 13, pages 668–674, 2000.

[125] R. Wildes. Iris recognition: An emerging biometric technology. *Proc. IEEE*, 85:1348–1363, 1997.

[126] R. P. Wildes, J. C. Asmuth, G. L. Green, S. C. Hsu, R. J. Kolczynski, J. R. Matey, and S. E. Mcbride. A system for automated iris recognition. In *Proc. IEEE Workshop on Applications of Computer Vision*, pages 121–128, 1994.

[127] Reg G. Willson and Steven A. Shafer. A perspective projection camera model for zoom lenses. In *Proc. 2nd Conf. Optical 3-D Measurement Techniques*, October 1993.

[128] L. Wiskott, J.-M. Fellous, and C. von der Malsburg. Face recognition by elastic bunch graph matching. *IEEE Trans. Pattern Analysis and Machine Intell.*, 19(7):775–779, 1997.

[129] G. Wolberg. *Digital Image Warping*. IEEE Computer Society Press, Los Alamitos, Ca., 1990.

[130] D. N. Wood, A. Finkelstein, J. F. Hughes, C. E. Thayer, and D. H. Salesin. Multiperspective panoramas for cel animation. In *Proc. SIGGRAPH 97*, pages 243–250, 1997.

[131] S. Wright. Linear programming methods lecture notes. CS525, UW-Madison, Spring 2002.

[132] Y. Yacob and L. Davis. Recognizing facial expressions by spatio-temporal analysis. In *Proc. 12th Int. Conf. Pattern Recognition*, volume 1, pages 747–749, 1994.

[133] Z. Zhang. Feature-based facial expression recognition: Sensitivity analysis and experiments with a multi-layer perceptron. *Int. J. Pattern Recognition and Artificial Intelligence*, 13(6):893–911, 1999.

[134] Z. Zhang, M. Lyons, M. Schuster, and S. Akamatsu. Comparison between geometry-based and gabor-wavelets-based facial expression recognition using multi-layer perceptron. In *Proc. 3rd Int. Conf. Automatic Face and Gesture Recognition*, pages 454–459, 1998.

[135] W. Zhao, R. Chellappa, A. Rosenfeld, and P.J. Phillips. Face recognition: A literature survey. *ACM Computing Surveys*, 35(4):399–458, 2003.

[136] S. Zhou and R. Chellappa. Probabilistic human recognition from video. *Proc. 7th European Conf. Computer Vision, Vol. III*, pages 681–697, 2002.

[137] A. Zomet and S. Peleg. Super-resolution from multiple images having arbitrary mutual motion. In S. Chaudhuri, editor, *Super-Resolution Imaging*, pages 195–209, Boston, Mass., 2001. Kluwer Academic.